

Vol. 15 • No. 2 • October 2021

ISSN: 0976 - 1330

Journal of GEOMATICS

Special Section
Flood Assessment and Modelling



INDIAN SOCIETY OF GEOMATICS

Journal of Geomatics

(A publication of the Indian Society of Geomatics)

Editorial Board

Chief Editor: Dr. R.P. Singh

(Address for Correspondence: Group Director, Geo-Sciences, Hydrology, Cryosphere Sciences and Applications Group, Space Applications Centre, ISRO, Ahmedabad - 380 015, India)

Phone: +91-79-26914018 (O), Email: rpsingh@sac.isro.gov.in, editorjogisg@gmail.com

Guest Editor:

Praveen K Gupta Ahmedabad, Email: pkgupta@sac.isro.gov.in

Associate Editors:

Harish Chandra Karnatak Dehradun, Email: harish.karnatak@gmail.com

Bijoy K. Handique Shillong, Email: bkhandique@gmail.com

D. Giri Babu Jodhpur, Email: giribabu.d@nrsc.gov.in

R. Ratheesh Ahmedabad, Email: ratheeshr@sac.isro.gov.in

S.V.V. Arun Kumar Ahmedabad, Email: arunkumar@sac.isro.gov.in

R. Agrawal Ahmedabad, Email: ritesh_agrawal@sac.isro.gov.in

Members:

A.R. Dasgupta Ahmedabad, Email: arup@ieee.org

P.K. Garg Dehradun, Email: gargpfce@iitr.ernet.in

P.K. Verma Bhopal, Email: drpkverma@rediffmail.com

Ashok Kaushal Pune, Email: akaushal1960@yahoo.co.in

T.T. Medhavy Australia, Email: medhavy.thankappan@ga.gov.au

I.V. Murali Krishna Hyderabad, Email: ivm@ieee.org

S.M. Ramasamy Tiruchirapalli, Email: grucc@ruraluniv.ac.in

P.S. Roy Hyderabad, Email: psroy1952@yahoo.in

Milap Chand Sharma New Delhi, Email: milap@mail.jnu.ac.in

Tara Sharma Canada, Email: sharmatara@yahoo.com

P. Venkatachalam Mumbai, Email: pvenk@csre.iitb.ac.in

Claudio Zucca Morocco Email: c.zucca@cgiar.org

Advisory Board

Paul J. Curran Vice-Chancellor, Bournemouth University, Poole, **UK**

V. Jayaraman Bengaluru, **India**

R. Krishnan Thiruvananthapuram, **India**

P. Nag Varanasi, **India**

M.P. Narayanan President, CSDMS, NOIDA, U.P., **India**

R.R. Navalgund Bengaluru, **India**

Y.S. Rajan Bengaluru, **India**

Josef Strobl Interfaculty Dept. of Geoinformatics, University of Salzburg, **Austria**

Journal of Geomatics
(A Publication of the Indian Society of Geomatics)

Vol. 15. No. 2 **Special Section: Flood Assessment and Modeling** October 2021

	Preface P K Gupta	208
1	Spatial Prediction of Flash Floods using Susceptibility Modeling and Geospatial Technology: A Review Gagandeep Singh and Ashish Pandey	209
2	Flood Inundation Mapping and Depth Modelling using Machine Learning algorithms and Microwave data Gyan Prakash, Praveen Kumar Gupta, G Venkata Rao and Deva Pratap	221
3	An integrated approach of flood risk assessment over a severely flood-prone coastal region using geomorphic classifiers, and socio-economic indicators Mohit Prakash Mohanty, K.V.H Durga Rao and Subhankar Karmakar	230
4	Atmospheric Rivers and Flood Events in Ganga and Brahmaputra River Basins Nimisha Singh, Rohit Pradhan and R. P. Singh	241
5	An Approach of Satellite and UAS based Mosaicked DEM for Hydrodynamic Modelling – A Case of Flood Assessment of Dhanera City, Gujarat, India. Kishanlal Darji, Dhruvesh P. Patel, Amit Kumar Dubey, Praveen K. Gupta and R P Singh	247
6	Assessment of surface flooding over India from passive microwave radiometer Rohit Pradhan, Nimisha Singh and R P Singh	258
7	Flood assessment in the Brahmaputra River using microwave remote sensing and hydrological modelling Amit Kumar Dubey and R. P. Singh	263
8	Rainfall-Runoff relationship for the Lower Tapi Basin Aditi Rathod, Amit Kumar Dubey, Sanskriti Mujumdar and Nirav Agrawal	268
9	Coupled Model for Flood Prone Lower Tapi River Basin Integrating Satellite Inputs Swati S. Patel and Praveen.K. Gupta	276

Special Section: Flood Assessment and Modeling

Preface

Flood is perhaps most devastating, wide spread and frequent disaster across the world. The researchers are constantly attempting to reduce the damages through the use of various flood management techniques. In the realms of monsoon, river flooding is a recurrent natural phenomenon. Recent occurrences of extreme precipitation show shift in the flooding pattern and frequencies due to changing climate. Hence, there is need to update the flood prone areas. The conventional means to record hydrological and meteorological parameters of a flood event is often limited to few in situ observations. An accurate monitoring of flood events is increasingly necessary to gain insight about both causes and remedies.

For the last two decades advancement in the field of remote sensing and data science have greatly facilitated the multi-dimensional quantitative approach of flood mapping, modeling and flood risk assessment. The growing availability of multi-temporal satellite data has increased opportunities for monitoring large rivers from space. A variety of passive (AMSR-E/2), and active (SAR, Altimeters, scatterometers etc.), sensors in the visible and microwave range are currently operating, which can delineate food boundaries and estimate inundation area. Radar altimeters show great promise for directly measuring stage variation in large rivers. It is possible to obtain estimates of river discharge from space, using ground measurements and satellite data to construct empirical curves that relate water surface area to discharge. Recently, high temporal resolution scatterometer and passive microwave radiometers are also being

used for the mapping of major floods. ISRO/DOS is playing a vital role in supporting the flood management activities, by providing space as well as aerial remote sensing based services and products through VEDAS, MOSDAC, BHUVAN web portals.

The aim of this special section on “Flood Assessment and Modeling” is to enrich our knowledge of application of different satellite technologies independently and also in integrated fashion with mathematical models on a regional and local scales. A wide variety of topics covered including tracking the extreme weather events by studying the atmospheric rivers, high temporal resolution of passive microwave for inundation mapping, Altimetry for river water level estimation, flash flood review, 1D and 2-D coupled models integrated with RS derived hydro-meteorological parameters, WRF-HYDRO etc. for flood inundation and water surface elevation modeling. I am thankful to all the authors who have contributed research article to this special section. Special thank for all the reviewers for timely review and valuable comments. I am grateful to editorial team for editing, formatting and bringing out this special section. This Special section, covering research experiences of flood risk analysis and applications, will undoubtedly provide new tools to flood risk managers to improve risk mitigation, both preventive and remedial.

P. K. Gupta
Guest Editor

Spatial Prediction of Flash Floods using Susceptibility Modeling and Geospatial Technology: A Review

Gagandeep Singh* and Ashish Pandey
 Indian Institute of Technology Roorkee, Roorkee, India
 *Email: gsingh@wr.iitr.ac.in

(Received: Aug 8, 2021; in final form: Oct 6, 2021)

Abstract: Spatial prediction of flash floods is essential for identifying the probable areas, which may be impacted due to the occurrence of an extreme event, and making better decisions and management plans to minimize the damages. Given the dynamic nature of the climate, complexity in the topography, and sparse data monitoring network, it is very challenging to predict flash floods in advance. However, spatial maps presenting the most susceptible flash flood-prone areas can be a valuable resource for planners, decision-makers, and people residing in such areas. Such maps can be obtained through flash flood susceptibility modeling using various remote sensing-based inputs and geospatial technology. Literature suggests that flash flood susceptibility studies are being employed by researchers worldwide for just about a decade now. In this paper, the status, current approaches, and challenges in this domain have been reviewed. The review focuses on using remote sensing and GIS for conducting flash flood susceptibility modeling to generate spatial maps. The study provides a detailed description of the input datasets and conditioning factors required for susceptibility assessment. Various approaches used for flash flood susceptibility assessment and their evolution have also been discussed.

Keywords: Flash flood susceptibility, Remote sensing, GIS, Spatial prediction, Extreme events

1. Introduction

1.1. Flooding and its impact on natural resources/ life
 Flooding is a catastrophic global phenomenon that results in voluminous destruction in terms of fatalities and property loss. It is probably the most destructive and recurring natural disaster affecting the ecosystem and its components. In an assessment report titled, "Natural disasters 2018: An opportunity to prepare." published in 2018 by CRED, it has been pointed out very clearly that "Floods have affected more people than any other type of disaster in the 21st century, including in 2018". The data regarding the number of flood events reported worldwide

from 1900 to 2018 has been presented in the form of a chart in Figure 1. A disaster event is taken into consideration by the CRED International Disaster Database if at least one criterion is fulfilled: (i) 10 or more people are reported to have been killed, (ii) 100 people are reported to have been affected, (iii) a call for international assistance, (iv) declaration of a state of emergency (Jha et al. 2013). In the last two decades, the number of flood disasters has repeatedly crossed the mark of 100 every year. Floods end up causing mammoth economic loss worldwide. Millions of people get displaced or killed in such events.

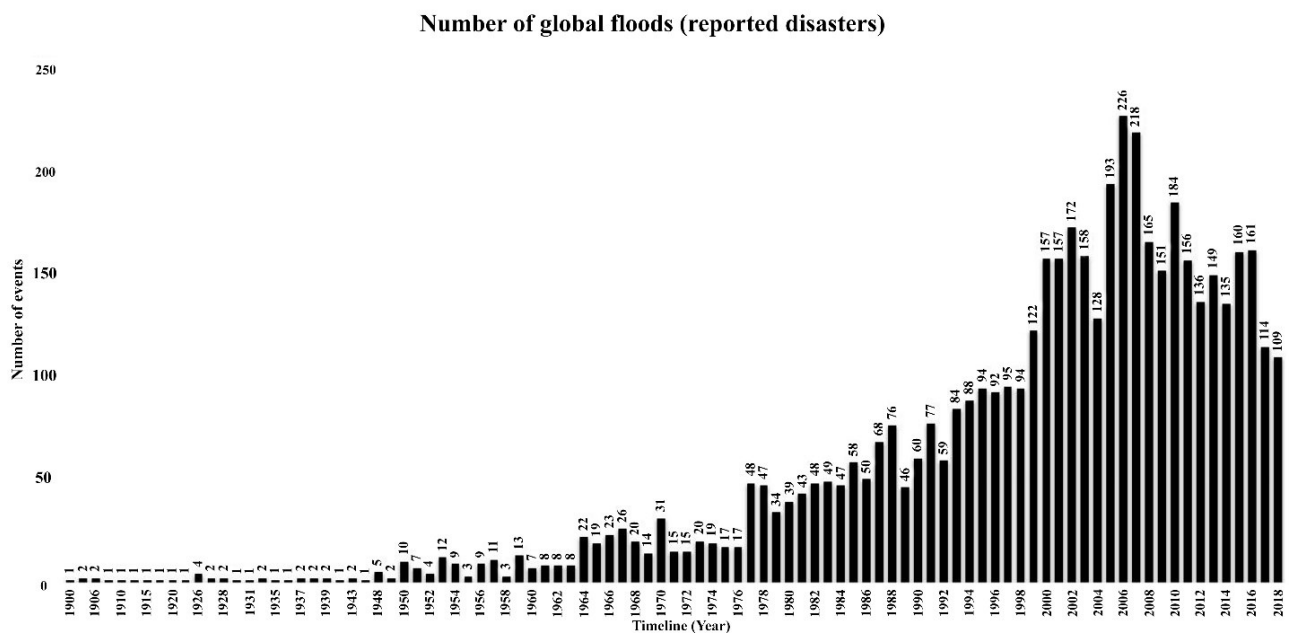


Figure 1. Number of reported flood disasters from 1901 to 2018

Data source: EMDAT (2019): OFDA/CRED International Disaster Database, Université catholique de Louvain – Brussels – Belgium

The receding floodwater consequently causes excessive deposition of mud and silt in the affected areas. In addition, the entire impacted terrain has very high chances of getting contaminated with dangerous materials, viz. chemicals, fuel, untreated sewage, and a massive amount of sharp debris. After the flood event, the standing water in the affected areas is highly vulnerable to outbreaks of life-threatening waterborne diseases like cholera, typhoid, and hepatitis A. There is a total failure of the infrastructure, causing long-term impacts on services like potable drinking water, wastewater treatment, transportation system, electricity, communication, education, and healthcare. Also, flood causes community-based social problems like large-scale crop destruction and loss of cattle. All these consequences bring life to a standstill leaving the communities economically vulnerable.

Floods have consequential impacts on the environment and natural resources in the affected areas. At times floods play a vital role in the sustenance of ecosystem and biodiversity by recharging groundwater systems, filling wetlands, increasing connection between aquatic habitats, and transportation of sediment and nutrients throughout the affected region. On the other hand, the involvement of human intervention in disturbing the river's natural course by either encroaching river banks for residential purposes or exploiting the river bed for mining activities has made the areas highly susceptible to destruction by flooding. Activities like deforestation along the river catchment degrade the hill-slopes and the river flood plains, thereby making the area erosion-prone resulting in excessive sediment and nutrient flow during floods. Consequently, downstream water quality is compromised. Other adverse effects of floods on natural resources include habitat loss, weed species dispersion, water pollution, diminished fish production, loss of wetlands and recreational areas.

Flash floods are highly complex events that depend on specific climate conditions, leading to high-intensity rainfall concentrated over an area for a short period, resulting in excessive surface runoff. These characteristics render the prediction of such events extremely difficult and equally challenging. The prediction models are of great utility in flood hazard assessment and management (Xie et al. 2017).

In this context, susceptibility modeling is critical to identify the most vulnerable areas prone to flash floods and are highly likely to experience damage and destruction. In addition, it also enables engineers, planners, policymakers, and authorities to prepare flash flood management plans to minimize the damage. In view of the available scientific literature, researchers have analyzed flash flood susceptibility. These studies have utilized the potential of geospatial technology to identify areas likely to be affected by flash floods. Furthermore, rapid advancements in remote sensing and GIS have translated into various approaches to model and assess flash flood susceptibility.

The main objective of this study is to present a detailed review of flash flood susceptibility modeling and assessment techniques.

1.2. Relevance of geospatial technology for flash flood susceptibility

Flash floods are highly complex and dangerous phenomena wherein the enormous volume of water precipitates within minutes or a few hours due to extreme rainfall events (Doswell 2015). Such events are usually a consequence of cloudbursts or thunderstorms. Several hydrological factors influence the occurrence of flash floods: antecedent rainfall, land use, land cover, population habitation, soil type, topography, terrain slope, and, most importantly, meteorological conditions (Doswell 2015). Another significant characteristic of a flash flood is the localization of heavy precipitation events. Interestingly flash floods can occur both on or near a river or away. The hydrological and dynamic nature of climatic factors makes predicting flash floods a very challenging affair. Moreover, it becomes more complex in data-scarce areas. Therefore, remote sensing and GIS for susceptibility modeling become a promising approach in identifying the most susceptible areas and can help reduce damages.

Earth observation capabilities have been improving rapidly, with various remote sensing datasets capable of capturing valuable information. Different satellite data products are being employed very effectively to derive input data required to perform susceptibility assessment. Digital elevation model (DEM), being the most innovative satellite product, is used to generate input parameters like slope, curvature, flow direction, aspect, and a few more (Himanshu et al. 2015; Dhami et al. 2018). Additionally, DEMs are also used to derive various indices which play a vital role in analyzing the susceptibility, viz. topographic wetness index, stream power index, topographic position index, etc. Also, input layers like rainfall, land use land cover (LULC), river density, distance from the river, normalized difference vegetation index (NDVI), etc., are derived using satellite data in a GIS environment. These input layers are processed in a GIS environment and then analyzed using various susceptibility modeling techniques and methods.

2. Review approach

A bibliographic search in the "Web of Science Core Collection" database was carried out with "flash flood susceptibility" keywords. The investigation resulted in 156 publications comprising complete research articles in peer-reviewed journals, book chapters, or conference proceedings. Furthermore, to get a sense of flash flood susceptibility (FFS) studies across the globe, the results were analyzed by filtering according to countries/ regions. Figure 2 shows the country-wise distribution of the publications. The analysis revealed that studies based on FFS had been carried out in 57 countries across the globe. Vietnam, China, Romania, Iran, and India are the top 5 countries on the list. The map in Figure 2 has been color-coded based on the number of studies in different countries.

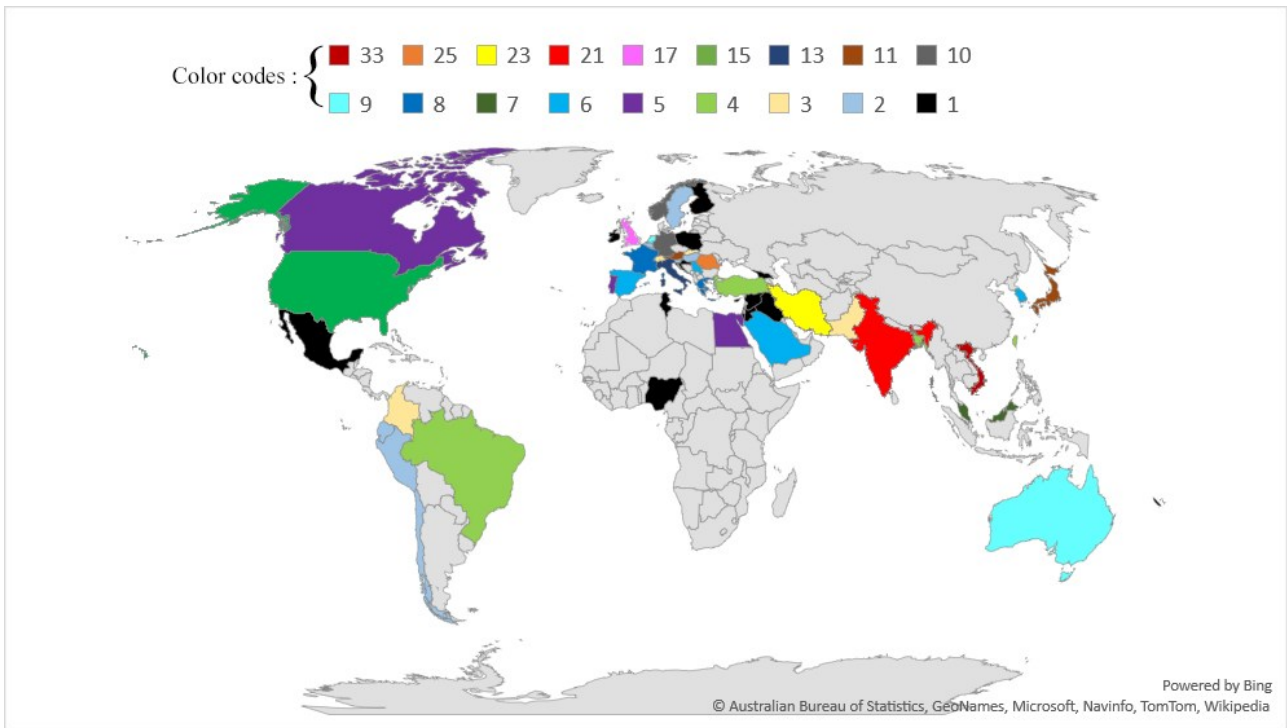


Figure 2. Distribution of the number of articles across the globe

Figure 3 presents the trend in the number of flash flood susceptibility (FFS) studies conducted from 2007 onwards.

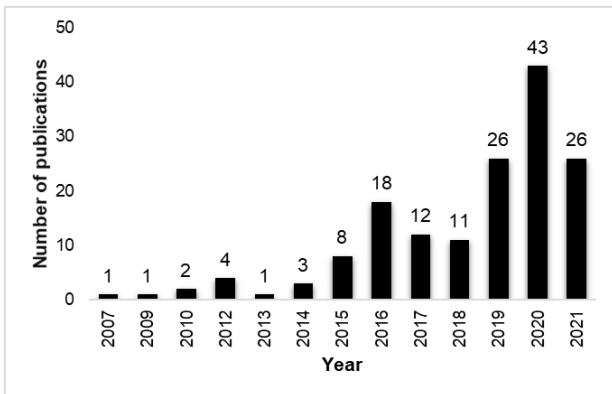


Figure 3. Number of publications on flash flood susceptibility on the Web of Science Database

3. Theoretical background and role of geospatial technology for flash flood susceptibility studies

3.1 Background of FFS

Flash flood susceptibility can be described as assessing the spatial probability of occurrence of flash floods in an area considering the meteorological, morphometric, and hydrological conditions (Santangelo et al. 2011). It is an approach to categorize or prioritize regions based on the degree to which they can be affected by extreme events in the future. In other words, susceptibility is the locational assessment of future events without considering its temporal probability (Tehrany et al. 2014). This approach is efficient in data-scarce areas where there is a deficit of adequate instrumentation to derive information about the recurrence interval of flash floods (Khosravi et al. 2016).

3.2 FF conditioning factors

The magnitude of a flash flood event is influenced by two significant factors: rainfall intensity and duration. Additionally, the catchment characteristics govern flash flood susceptibility through geomorphometric and meteorological factors often referred to as the conditioning factors. For analyzing the flash flood susceptibility, relationship of all the conditioning factors with the distribution of previously occurred flash flood events is assessed (Liu and De Smedt 2005; Tehrany et al. 2015a). Various conditioning factors are selected to comprehend their influence and relationship with flash flooding. Therefore, this section presents the significance of all major flash flood conditioning factors.

The slope for an area is derived from the DEM and is considered one of the most important input parameters that influence the severity of flash floods. The slopes in an area are directly proportional to the magnitude of velocity that could be obtained by the surface runoff (Tehrany et al. 2015b). This plays a crucial role, especially in the mountainous area prone to flash floods primarily due to cloud burst events. Also, areas with low slopes have a higher chance of water accumulation (Popa et al. 2019).

The aspect gives a clear representation of directions in the study area viz. flat, north, northeast, east, southeast, south, southwest, and northwest, which can be related to the direction of water flow. It is a crucial morphometric factor that plays an active role when the soil gets saturated, especially on the shaded slopes responsible for generating more surface runoff than the areas with dry soils on the sunny side (Costache and Bui 2020). It also helps identify flat regions that may be most prone to flood damages (Popa et al. 2019). DEM is employed to derive aspects.

Convergence Index (CI) is a highly significant flash flood conditioning factor (Costache et al. 2020b). CI values may be positive and negative, with negative values indicating high convergence of rivers (Zaharia et al. 2017), leading to a low time of concentration of the runoff and hence higher chances of flash flood occurrence vice-versa. DEM is used to generate a convergence index for an area.

Distance from the rivers and river density are naturally prominent factors in identifying flood-prone areas. Areas near the rivers have more chances to get flooded and vice-versa (Glenn et al. 2012). Buffer analysis in a GIS environment is instrumental in segregating areas close to the river proximity.

The geology of the area defines its hydrological behavior. Soil permeability is one of the critical geologic attributes which governs surface runoff and infiltration. Impermeable geology supports higher depth surface runoff in comparison to permeable soil. Therefore, different rock formations contribute to the runoff as per their nature. Lithology is very closely associated or analogous to geology as it represents the rock and soil types in an area. Hydrological Soil Group (HSG) is another factor that governs water infiltration and contributes to runoff generation. This parameter is used to compute the curve numbers (CN), further employed to calculate surface runoff for catchments (Sharma et al. 2021).

Land use/cover influences the runoff velocity in a catchment. The areas with dense forest cover and high vegetation presence will not allow rainwater to contribute as runoff. Therefore, the higher the vegetation density lower are the chances of flooding (Tehrany et al. 2014). Urban areas are very much prone to increased runoff. Thus, land use/cover plays a prominent role in flash flood susceptibility modeling (Mindje et al. 2019). There are readily available global land use/cover datasets freely available to use. Also, optical satellite imagery from Landsat and Sentinel missions are highly recommended datasets to prepare LULC maps for any area (Chaves et al. 2020; Singh and Pandey 2021).

L-S factor is a morphometric factor that is extensively used to realize the combined effect of length and steepness of the slopes on the behavior of runoff (Zaharia et al. 2017; Costache et al. 2020b). It is calculated using the formula proposed by Moore and Wilson in 1992.

$$LS = \left(\frac{A_s}{22.13}\right)^m \left(\frac{\sin \theta}{0.0896}\right)^n \quad (1)$$

Where A_s is the unit contributing area (m^2), θ is the slope in radians, m and n are exponents ranging between 0.4 to 0.56 and 1.2 to 1.3, respectively. This parameter is derived using a DEM, and QGIS software has a built-in tool in the Terrain Analysis module of SAGA GIS.

Rainfall is the most critical factor responsible for the occurrence of flash floods. Therefore, spatial variability of rain intensity becomes of utmost relevance for susceptibility assessment. A common approach followed is to compute the mean annual rainfall raster from the long-

term data collected from a network of well-distributed meteorological and hydrometric stations. Modified Fournier Index (MFI) is widely used to capture the spatial variation of rainfall intensity thus employed (Zaharia et al. 2015; Costache et al. 2020a) by various researchers for susceptibility assessment using the following formula:

$$MFI = \sum_{i=1}^{12} \frac{P_i^2}{P} \quad (2)$$

Where P_i is the monthly average rainfall for a month i in mm and P is the average annual rainfall.

Normalized Difference Vegetation Index (NDVI) has been explored for flood susceptibility studies in the past (Khosravi et al. 2018; Ali et al. 2020). The importance of vegetation cover in controlling runoff justifies its use for susceptibility analysis. The NDVI values range between -1 and +1. NDVI is conventionally used for monitoring crop health status and agricultural production using remote sensing observations. It is derived using satellite data acquired in near-infrared (NIR) and red band using the following formula:

$$NDVI = \frac{NIR - R}{NIR + R} \quad (3)$$

Where NIR and R represent the reflectance values in the near infrared and red bands respectively.

Curvature gives an idea about the shape of the ground surface, which governs the accumulation of water or runoff on the slopes. In line with this concept, profile curvature represents the curvature of a vertical plane with respect to the direction of slope (Duman et al. 2006). It represents the direction of the maximum slope. The values may be positive signifying areas less susceptible to surface runoff and negative signifying vice-versa (Zaharia et al. 2017). If the ground surface is convex upwards, the profile curvature is negative (Figure 4a), suggesting accelerated runoff, values nearing zero (Figure 4c) indicate flat surface. In contrast, areas with positive values (Figure 4b) concave upwards and offer decelerated runoff.

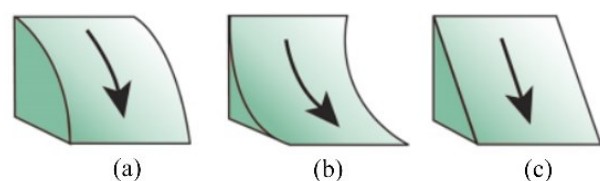


Figure 4. Pictorial representation of profile curvature (a) negative (b) positive and (c) zero value

(Image source:

<https://desktop.arcgis.com/en/arcmap/10.3/manage-data/raster-and-images/curvature-function.htm>)

Another exciting concept is the plan curvature represented by the contour created at the horizontal plane and ground surface intersection (Costache, 2019a). Plan curvature plays a vital role in analyzing areas susceptible to flash flooding by differentiating areas with convergent and

divergent runoff characteristics. It is perpendicular to the direction of the maximum slope. A laterally convex surface is expressed by positive values (Figure 5a). A laterally concave surface is expressed by negative values (Figure 5b). The linear surface has zero value of plan curvature (Figure 5c). Profile and plan curvature rasters are derived from DEM in GIS software.

Stream Power Index (SPI) indicates the river basin's erosive power and runoff capacity (Moore and Grayson 1991). In other words, it is an indicator of transport and abrasive potential of the flood water (Sharma, 2010).

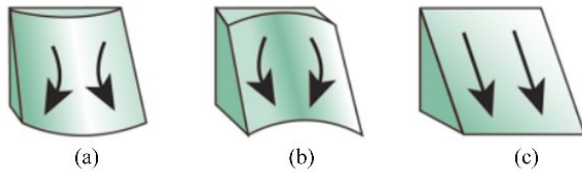


Figure 5. Pictorial representation of plan curvature (a) positive (b) negative and (c) zero value

(Image source:

<https://desktop.arcgis.com/en/arcmap/10.3/manage-data/raster-and-images/curvature-function.htm>)

Higher values of SPI signify the faster movement of water, while low values suggest slow motion (Chowdhuri et al. 2020). It is calculated using the following formula:

$$SPI = A_s \tan \beta \quad (4)$$

Where A_s is the specific catchment area (m^2m^{-1}) and β is the slope expressed in degrees.

Topographic Position Index (TPI) measures the elevation difference between a cell and its neighboring cells (Costache and Bui 2020).

$$TPI = E_c - \left(\frac{1}{n^M} \sum_{i \in m} E_i \right) \quad (5)$$

E_c is the elevation at the central point, E_i is the elevation, and M is the predetermined radius (predetermined matrix length).

Topographic Wetness Index (TWI) underlines the effect of topography on the accumulated water in each pixel (Gokceoglu et al. 2005). It is expressed as the ratio of specific catchment area and the slope angle values. This parameter indicates spatial variation in the wetness (Beven and Kirkby 1979) and is expressed by the following formula:

$$TWI = \ln \left(\frac{A_s}{\tan \beta} \right) \quad (6)$$

Where A_s is the cumulative upslope area contributing at a point (per unit contour length) and $\tan \beta$ is the slope at the point in degrees.

It is worth noting here that not all the above-discussed conditioning factors may influence every study area. Also, there might be the existence of multicollinearity, which may impact the accuracy of the results. Therefore, it is recommended to employ multicollinearity diagnostic tests

for determining the most influential factors and ignore the redundant ones in the flash flood susceptibility analysis. The two most popular statistical methods to test multicollinearity are VIF (Variance Inflation Factor) and Tolerance (TOL). VIF greater than 10 or tolerance less than 0.1 confirms the presence of multicollinearity in the conditioning factors (Hair et al. 2009).

3.3 Concept of Flash Flood Potential Index

Flash Flood Potential Index (FFPI) directly addresses the objectives of susceptibility assessment. The concept of FFPI was introduced by Greg Smith in 2003 to determine the hydrological response of the Flash Flood Monitoring and Prediction System to heavy rain by analyzing the physiographic characteristics of the Colorado river basin of the USA. The objective behind introducing this concept was to enhance flash flood forecasts. Only four factors were taken into consideration, namely, slope, vegetation cover, soil type, and land use. Raster layers for each factor were prepared, and relative indexing was assigned to them, ranging from 1 to 10. Each layer was further classified using an equal interval approach, and each layer was given equal weight. Finally, the layers were averaged together to obtain layers representing the flash flood potential.

Gradually, the methodology was evolved, and studies on FFPI were conducted in different parts of the USA and elsewhere considering more variables/ factors (Davis 2002; Krzdlo 2010; Ceru 2012; Zaharia et al. 2015; Prăvălie and Costache 2013; Minea 2013; Zogg and Deitsch 2013; Tincu et al. 2018). In light of the above-cited literature, it is to be noted that none of these studies considered the locations where flash flood events occurred previously, and the weights to the flash flood conditioning factors were assigned subjectively. Moreover, a GIS was employed to estimate FFPI using a simple overlay technique on the conditioning factors taken into consideration.

Therefore, to address the drawbacks mentioned above, significant modifications were introduced in the approach. All the flash flood susceptibility studies are conducted considering the past flash flood event locations. Furthermore, advanced statistical methods and machine learning techniques are being widely used by researchers worldwide to perform flash flood susceptibility modeling (Tehrany et al. 2015a; Lee et al. 2012; Chapi et al. 2017; Janizadeh et al. 2019; Bui et al. 2019). Therefore, it can be stated that FFPI is a highly effective indexing approach to understand the risk of flash flooding in any area (Zog and Deitsch 2013).

4. FFS modeling approaches

Literature suggests that flash flood susceptibility modeling approaches can be classified under four broad categories: bivariate statistical methods, multi-criteria decision-making approach, machine learning-based approach, and hybrid modeling approach. The following sections provide a detailed overview of each of these approaches.

4.1 Statistical modeling

Frequency Ratio (FR), Weights of Evidence (WoE), and Statistical Index (SI) are among the most popular bivariate statistical models employed for modeling flash flood susceptibility (Tehrany et al. 2014; Khosravi et al. 2016; Rahmati et al. 2016). A few other models like Information Value (IV) and Index of Entropy (IoE) have also been adopted in a few studies to model FFS. These methods are based on the correlation between flash flood locations and the parameters controlling the flash flood occurrences in the area.

However, there is a significant drawback in the bivariate statistical modeling approaches. These methods capture only the spatial relationship between the flash flood event locations and the conditioning factors without considering the relationship between the predictors (Tehrany et al. 2014).

4.2 Multicriteria decision making

This approach is described as a complex decision-making tool that considers quantitative and qualitative factors (Mardani et al. 2015). Analytic hierarchy process (AHP) and technique for order of preference by similarity to ideal solution (TOPSIS) are the two popular MCDM approaches that have been employed for modeling flash flood susceptibility (Khosravi et al. 2019).

MCDM approaches provide a unique capability to determine and assign weights to the conditioning factors and the decision alternatives for analyzing flash flood susceptibility. Methods like AHP are employed to obtain a pair-wise comparison matrix for each conditioning factor and the sub-criteria, and finally, the correct weights are determined.

4.3 Machine learning models

Machine learning (ML) has become one of the most revolutionary multidisciplinary technologies. This is one of the fastest-growing modern-day technologies offering several models to simulate and solve a real-life problem. Some of the most popular machine learning methods being used for flash flood susceptibility modeling include artificial neural networks (Chakraborty et al. 2021), logistic regression (Nandi et al. 2016), support vector machines (Tehrany et al. 2015b), and decision trees (Khosravi et al. 2018). Researchers have employed several different machine learning algorithms to perform flash flood susceptibility modeling. These algorithms have a typical working framework because the algorithms are trained using a subset of flash flood event locations.

Post-training, the algorithm is tested or validated on the remaining set of flash flood locations. Finally, a comparison is performed to observe the effectiveness of the approach adopted.

4.4 Hybrid models

Hybrid models refer to ensembles of statistical models, multi-criteria decision-making models, and machine learning models. To improve the accuracy of spatial prediction of flash floods, susceptibility assessment is improvised by using combinations or ensembles of two

different types of models (Bui et al. 2018; Costache et al. 2019a; Costache 2019b; Costache et al. 2020b; Pham et al. 2020b)

5. Review and synthesis

Table 1 presents studies that demonstrate different approaches adopted by researchers for flash flood modeling studies along with flash flood conditioning factors considered in each research and significant findings. It is to be noted that all the studies presented have employed remote sensing datasets and GIS to prepare the flash flood conditioning factors. Additionally, the overlay tools and ability of a GIS to perform various raster and vector operations make it an integral part of any FFS study. Furthermore, the most crucial part of any FFS modeling study is the validation of the model used. For validation, the use of Receiver Operating Characteristic (ROC) curves is the most sought-after method used in every FFS study. These curves are employed to evaluate the model capability of being able to predict an event correctly. ROC curve represents sensitivity on the Y-axis and (1-Specificity) on the X-axis (Chen et al. 2017). Once the curve is prepared, Area Under Curve (AUC) is determined, indicating the model's effectiveness. AUC values range between 0 and 1. AUC of 1 indicates a perfect model, and 0 refers to a weak model (Costache and Zaharai 2017). AUC values are calculated using the following formula:

$$AUC = \frac{(\sum TP + \sum TN)}{(P + N)} \quad (8)$$

Where TP represents true positive and TN represents true negative, and their sum indicates the sum of correctly classified pixels. P is the number of pixels representing flash flood event locations, and N represents non-flood locations.

Table 1 presents a compilation of flash flood susceptibility assessment studies in four sections. Section (a) discusses four studies conducted using different statistical methods, section (b) presents a study conducted using MCDM and ML models, section (c) presents three studies conducted using advanced machine learning models, and section (d) presents five studies wherein researchers have employed hybrid models.

The statistical models used for FFS have mathematical representations, which are easily translated into data modeling software like Microsoft EXCEL. All the conditioning factors are analyzed class-wise to obtain the model coefficients for each factor. Finally, these coefficients are used to calculate the FFPI. As far as the machine learning models are concerned, WEKA is the most popular open-source machine learning and data mining software widely employed for FFS studies (Khosravi et al. 2018; Janizadeh et al. 2019; Popa et al. 2019; Costache et al. 2020b). It features a huge number of in-built models and tweaking capabilities that researchers are extensively using worldwide.

Table 1: Existing flash flood susceptibility studies. The list in the table is sorted based on the type of approach adopted (statistical, multi-criteria decision making, machine learning, and hybrid)

#	Reference	Modeling approach	Location/ study area	Data/ conditioning factors	Findings
(a)		<u>Statistical models</u>			
1	Costache and Zaharia 2017	Frequency ratio and Weights of Evidence	Bâsca Chiojdului river catchment, Romania	Slope, L-S factor, profile curvature, drainage network density, convergence index, aspect, lithology, LULC, and HSG	FFPI and susceptibility maps were derived on the basis of the torrential inventory, which was split for training and validation purposes. ROC curve was employed to validate the results for both models. However, no comparative assessment was done for the methods. Area percentage distribution under each susceptibility class was presented for both models.
2	Cao et al. 2016	Frequency ratio and Statistical Index	Beijing, China	Elevation, slope, curvature, land use, geology, soil texture, subsidence risk area, SPI, TWI, short-term heavy rain	The authors prepared an inventory of 85 flash flood hazard locations. These were split into 70:30 for training and validation. Validation was done using the area under the curve (AUC) assessment. Results revealed that FR produced higher prediction accuracy in comparison to SI
3	Khosravi et al. 2016	Shannon's entropy, Statistical index, Weighting factor	Haraz, Iran	Slope angle, plan curvature, altitude, TWI, SPI, distance from the river, rainfall, geology, land use, and NDVI	Three different statistical models were applied for flash flood susceptibility mapping. 211 flood locations inventory was split in 70:30 for training and validation purposes. Performance evaluation was done with respect to the FR model. Analysis revealed that the SI model performed the best.
4	Chakraborty et al. 2021	ANN, DLNN and PSO	Kangsabati River Basin, India	Aspect, elevation, slope, plan curvature, profile curvature, TWI, TRI, SPI, distance from the river, drainage density, distance from the road, rainfall, LULC, and Geology	Three advanced models were employed for performing flash flood susceptibility assessment. The results indicated that the PSO model showed the best results for both training and validation data of the events inventory among the three.
(b)		<u>Multicriteria Decision Making models</u>			
5	Khosravi et al. 2019	VIKOR, TOPSIS, SAW, NBT and NB	Jiangxi, China	NDVI, lithology, land use, distance from the river, curvature, altitude, STI, TWI, SPI, soil	Three MCDM models and 2 ML models were employed for flash flood susceptibility mapping. Their validation and comparison were made using the ROC curve method, Kappa, and AUC.

#	Reference	Modeling approach	Location/ study area	Data/ conditioning factors	Findings
				type, slope, and rainfall	
(c) <u>Machine learning-based models</u>					
6	Janizadeh et al. 2019	ADT, MLP, FT, KLR and QDA	Tafresh, Iran	Elevation, slope, slope aspect, distance from rivers, average annual rainfall, land use, soil type, and lithology	Four machine learning-based models were employed. ADT model performed the best among these for both training and validation, followed by MLP, QDA, KLR, and FT. AUC was used for the performance evaluation of the models.
7	Band et al. 2020	BRT, PRF, RRF and ERT	Kalvan, Iran	Altitude, slope, aspect, plan curvature, profile curvature, distance from the river, distance from the road, land use, lithology, soil depth, rainfall, SPI, and TWI	Machine learning approaches sometimes pose a problem of overfitting. To address this shortcoming, four hybrid models with regularized and parallel and boosting techniques were introduced to reduce the errors. ERT model with an AUC of 0.82 outperformed for its predictive capability, followed by RRF, PRF, and BRT.
8	Pham et al. 2020a	KLR, RBFC, NBM, and LMT	Nghe An, Vietnam	Soil, slope, curvature, river density, flow direction, distance from rivers, elevation, aspect, land use, and geology	Four machine learning-based models were applied for flash flood susceptibility assessment and comparison. KLR was the best model using training data, while LMT demonstrated higher predictive ability in the validation. LMT was robust and capable of reducing overfitting.
(d) <u>Hybrid models</u>					
9	Pham et al. 2020b	ABM-CDT, Bag- CDT, Dag-CDT, MBAB-CDT, and single CDT	Tafresh, Iran	Distance from the river, aspect, elevation, slope, rainfall, distance from faults, soil types, land use, and lithology	Five novel machine learning- based hybrid models were employed for susceptibility modeling. An inventory of 320 previous events was prepared for the training and validation of models. ABM-CDT displayed the best predictive capability with an AUC of 0.957, followed by Dag-CDT, MBAB-CDT, Bag-CDT, and CDT.
10	Costache et al. 2019a	LR-FR, LR-WoE, SVM-FR, SVM-WoE	Prahova river catchment (Romania)	Slope angle, land use, lithology, HSG, convergence index, TWI, TPI, aspect, plan	Four hybrid models were proposed for evaluating the flash flood potential. Assessment of model performance revealed that LR- FR and LR-WoE were most effective for success rate and prediction rate. At the same

#	Reference	Modeling approach	Location/ study area	Data/ conditioning factors	Findings
				curvature, and profile curvature	time, SVM-FR and SVM-WoE were the most accurate models for training and validating areas, respectively.
11	Costache et al. 2020a	Integration of AHP with kNN and lazy KS	Prahova river basin in Romania	slope angle, aspect, plan curvature, profile curvature, convergence index, TPI and TWI	FFPI assessment was done using the kNN and lazy KS models stand-alone and their ensembles with AHP. Models were trained and validated using torrential areas inventory. ROC curves and AUC values revealed that all models showed good performance.
12	Costache et al. 2020b	Integration of SI with LR, CART, MLP, RF and SVM	Bâsca Chiojdului Catchment, central south- eastern region of Romania	Slope, L-S Factor, Convergence index, SPI, TWI, profile curvature, TPI, land use, HSG, and lithology	Hybrid integration of bivariate statistical method with five machine learning approaches was employed for obtaining flash flood susceptibility maps. Models were trained and validated based on a torrential area inventory dataset with a split of 70:30. MLP-SI model performed the best with AUC of 0.94 and 0.927 for training and validation, respectively.
13	Costache and Bui 2020	ADT with IoE ADT with AHP	Romania	Slope angle, land use, profile curvature, plan curvature, convergence index, aspect, HSG, and TPI	AHP, IoE, and two hybrid models formed by integration with the ADT algorithm were employed. The models were evaluated using ROC and Kappa. ADT-AHP performed the best with a sensitivity of 100%, specificity of 80.49%, and Kappa statistics of 0.758

ADT: Alternating Decision Tree; IoE: Index of Entropy; AHP: Analytic Hierarchy Process; SI: Statistical index; LR: Logistic Regression; CART: Classification and Regression Trees; kNN: k-Nearest Neighbour; KS: K-Star; MLP: Multilayer Perceptron; RF: Random Forest; SVM: Support Vector Machine; KLR: Kernel Logistic Regression; RBFC: Radial Basis Function Classifier; MNB: Multinomial Naïve Bayes; LMT: Logistic Model Tree; BRT: Boosted Regression Tree; PRF: Parallel Random Forest; RRF: Regularized Random Forest; ERT: Extremely Randomized Trees; ABM-CDT: AdaBoostM1 based Credal Decision Tree; Bag-CDT: Bagging based Credal Decision Tree; Dag-CDT: Dagging based Credal Decision Tree; MBAB-CDT: MultiBoostAB based Credal Decision Tree; CDT: Single Credal Decision Tree; FT: Functional Tree; KLR: Kernel Logistic Regression; QDA: Quadratic Discriminant Analysis; VIKOR: Vlse Kriterijuska Optimizacija I Komoromisno Resenje; TOPSIS: Technique for Order Preference by Similarity to Ideal Solution; SAW: Simple Additive Weighting; Naïve Bayes Trees: NBT; Naïve Bayes: NB; ROC: Receiver Operating Characteristic; AUC: Area Under the Curve

6. Summary and conclusions

The accurate and timely spatial prediction of flash floods is a challenging prospect. In this paper, an attempt has been made to review the progress towards this goal. Various approaches adopted by researchers worldwide have been discussed in detail. A database of 156 articles on flash flood susceptibility was considered for the review.

The main findings of the review are:

- (i) A comprehensive review of the studies enabled the identification of sixteen flash flood

conditioning factors used in combinations in FFS modeling.

- (ii) It is recommended that the following factors viz. slope, aspect, convergence index, distance from the river, geology, lithology, hydrological soil group, land use land cover, L-S factor, rainfall, normalized difference vegetation index, plan curvature, profile curvature, stream power index, topographic position index and topographic wetness index must be considered in all FFS studies.

- (iii) Multicollinearity among the above-listed factors can lead to redundancy, which would reduce the accuracy of susceptibility assessment. Therefore, it is recommended to employ tools like VIF and TOL to identify and eliminate redundant factors for the final analysis.
- (iv) Table 1 presents the development in FFS modeling approaches. A detailed assessment of case studies has been presented addressing each modeling approach type: statistical methods, multi-criteria decision-making models, machine learning-based models, and hybrid approaches.
- (v) A discussion on the gradual evolution of the susceptibility modeling approaches revealed that flash flood locations inventory is an important input to accurately model and predict the spatial occurrence of future events.
- (vi) The future scope in flash flood susceptibility lies in improving weights assignment to individual conditioning factors to develop the final FFPI.
- (vii) There is a tremendous scope in the development of hybrid models. Numerous model combinations can be developed using machine learning algorithms through open-source data mining software like WEKA.
- (viii) Most importantly, this paper highlights the importance and use of geospatial technology in preparing input layers and preparing flash flood susceptibility maps.
- (ix) The FFS maps can be very effectively used by the decision-makers and disaster management agencies to plan and reduce the damage caused by flash flood events.

Acknowledgments

We wish to express a deep sense of gratitude and sincere thanks to the Department of Water Resources Development and Management (WRD&M), IIT Roorkee, for providing a conducive environment to conduct this research work. We are grateful to IIT Roorkee for providing the Mahatma Gandhi Central Library (MGCL) remote access portal to access and download the research papers from the Web of Science and other subscription-based journals.

References

Ali S. A., F. Parvin, Q. B. Pham, M. Vojtek, J. Vojteková, R. Costache, N. T. T. Linh, H. Q. Nguyen, A. Ahmad and M. A. Ghorbani (2020). GIS-based comparative assessment of flood susceptibility mapping using hybrid multi-criteria decision-making approach, naïve Bayes tree, bivariate statistics and logistic regression: A case of Topľa basin, Slovakia. *Ecological Indicators*, 117, 106620.

Band S. S., S. Janizadeh, S. Chandra Pal, A. Saha, R. Chakraborty, A. M. Melesse, and A. Mosavi (2020). Flash flood susceptibility modeling using new approaches of hybrid and ensemble tree-based machine learning algorithms. *Remote Sensing*, 12(21), 3568.

Bui D. T., P. T. T. Ngo, T. D. Pham, A. Jaafari, N. Q. Minh, P. V. Hoa, and P. Samui (2019). A novel hybrid approach based on a swarm intelligence optimized extreme

learning machine for flash flood susceptibility mapping. *Catena*, 179, 184-196.

Bui D. T., M. Panahi, H. Shahabi, V. P. Singh, A. Shirzadi, K. Chapi, K. Khosravi, W. Chen, S. Panahi, S. Li and B. B. Ahmad (2018). Novel hybrid evolutionary algorithms for spatial prediction of floods. *Scientific reports*, 8(1), 1-14.

Cao C., P. Xu, Y. Wang, J. Chen, L. Zheng, and C. Niu (2016). Flash flood hazard susceptibility mapping using frequency ratio and statistical index methods in coalmine subsidence areas. *Sustainability*, 8(9), 948.

Ceru J. (2012). The flash flood potential index for Pennsylvania. In 2012 ESRI federal GIS conference. <http://proceedings.esri.com/library/userconf/feduc12/papers/user/JoeCeru.pdf>.

Chakraborty R., S. Chandra Pal, F. Rezaie, A. Arabameri, S. Lee, P. Roy, A. Saha, I. Chowdhuri and H. Moayedi (2021). Flash-Flood Hazard Susceptibility Mapping in Kangsabati River Basin, India. *Geocarto International*, 1-21.

Chapi K., V. P. Singh, A. Shirzadi, H. Shahabi, D. T. Bui, B. T. Pham and K. Khosravi (2017). A novel hybrid artificial intelligence approach for flood susceptibility assessment. *Environmental modelling and software*, 95, 229-245.

Chaves M. E. D., M. C. A. Picoli, and I. D. Sanches (2020). Recent applications of Landsat 8/OLI and Sentinel-2/MSI for land use and land cover mapping: A systematic review. *Remote Sensing*, 12(18), 3062.

Chen W., H. R. Pourghasemi, and Z. Zhao (2017). A GIS-based comparative study of Dempster-Shafer, logistic regression and artificial neural network models for landslide susceptibility mapping. *Geocarto international*, 32(4), 367-385.

Chowdhuri I., S. C. Pal, and R. Chakraborty (2020). Flood susceptibility mapping by ensemble evidential belief function and binomial logistic regression model on river basin of eastern India. *Advances in Space Research*, 65(5), 1466-1489.

Costache R. (2019a). Flash-Flood Potential assessment in the upper and middle sector of Prahova river catchment (Romania). A comparative approach between four hybrid models. *Science of the Total Environment*, 659, 1115-1134.

Costache R. (2019b). Flash-flood Potential Index mapping using weights of evidence, decision Trees models and their novel hybrid integration. *Stochastic Environmental Research and Risk Assessment*, 33(7), 1375-1402.

Costache R., and D. T. Bui (2020). Identification of areas prone to flash-flood phenomena using multiple-criteria decision-making, bivariate statistics, machine learning and their ensembles. *Science of The Total Environment*, 712, 136492.

Costache R., Q. B. Pham, E. Sharifi, N. T. T. Linh, S. I. Abba, M. Vojtek, J. Vojteková, Pham T. T. N. and D. N. Khoi (2020a). Flash-flood susceptibility assessment using multi-criteria decision making and machine learning

- supported by remote sensing and GIS techniques. *Remote Sensing*, 12(1), 106.
- Costache R., H. Hong, and Q. B. Pham (2020b). Comparative assessment of the flash-flood potential within small mountain catchments using bivariate statistics and their novel hybrid integration with machine learning models. *Science of The Total Environment*, 711, 134514.
- Costache R., and L. Zaharia (2017). Flash-flood potential assessment and mapping by integrating the weights-of-evidence and frequency ratio statistical methods in GIS environment—case study: Bâsca Chiojdului River catchment (Romania). *Journal of Earth System Science*, 126(4), 1-19.
- CRED/UNISDR (Centre for Research on the Epidemiology of Disaster/United Nations Office for Disaster Risk Reduction). 2015. *The Human Cost of Weather-Related Disasters 1995-2015*. Geneva/Brussels, CRED/UNISDR. www.unisdr.org/we/inform/publications/46796
- Davis R. S. (2002). The flash flood (FF) index: estimating flash flood severity. In *Proceedings of the Symposium on Managing the Extremes, Floods and Droughts*. Environmental and Water Resources Institute of American Society of Civil Engineers Roanoke, VA.
- Dhami B., S. K. Himanshu, A. Pandey, and A. K. Gautam (2018). Evaluation of the SWAT model for water balance study of a mountainous snowfed river basin of Nepal. *Environmental Earth Sciences*, 77(1), 1-20.
- Doswell C. A. (2015). Hydrology, Floods and Droughts | Flooding. *Encyclopedia of Atmospheric Sciences*, 201–208. doi:10.1016/b978-0-12-382225-3.00151-1
- Duman T. Y., T. Can, C. Gokceoglu, H. A. Nefeslioglu, and H. Sonmez (2006). Application of logistic regression for landslide susceptibility zoning of Cekmece Area, Istanbul, Turkey. *Environmental Geology*, 51(2), 241-256.
- Glenn E. P., K. Morino, P. L. Nagler, R. S. Murray, S. Pearlstein, and K. R. Hultine (2012). Roles of saltcedar (*Tamarix* spp.) and capillary rise in salinizing a non-flooding terrace on a flow-regulated desert river. *Journal of Arid Environments*, 79, 56-65.
- Gokceoglu C., H. Sonmez, H. A. Nefeslioglu, T. Y. Duman, and T. Can (2005). The 17 March 2005 Kuzulu landslide (Sivas, Turkey) and landslide-susceptibility map of its near vicinity. *Engineering geology*, 81(1), 65-83.
- Hair J., W. Black, B. Babin, and R. Anderson, (2009). *Multivariate Data Analysis*. 7111 Ed. Prentice Hall Publishing, New York
- Himanshu S. K., A. Pandey, and S. S. Palmate (2015). Derivation of Nash Model Parameters from Geomorphological Instantaneous Unit Hydrograph for a Himalayan River using ASTER DEM. In *Proceedings of International Conference on Structural Architectural and Civil Engineering*, Dubai.
- Janizadeh S., M. Avand, A. Jaafari, T. V. Phong, M. Bayat, E. Ahmadisharaf, I. Prakash, B. T. Pham and Lee, S. (2019). Prediction success of machine learning methods for flash flood susceptibility mapping in the Tafresh watershed, Iran. *Sustainability*, 11(19), 5426.
- Jha A. K., T. W. Miner, and Z. Stanton-Geddes (2013). Appendix A. Disaster Definitions and Classifications. *Emergency Events Database (EM-DAT)*.
- Khosravi K., B. T. Pham, K. Chapi, A. Shirzadi, H. Shahabi, I. Revhaug, I. Prakash and D. T. Bui (2018). A comparative assessment of decision trees algorithms for flash flood susceptibility modeling at Haraz watershed, northern Iran. *Science of the Total Environment*, 627, 744-755.
- Khosravi K., E. Nohani, E. Maroufinia, and H. R. Pourghasemi (2016). A GIS-based flood susceptibility assessment and its mapping in Iran: a comparison between frequency ratio and weights-of-evidence bivariate statistical models with multi-criteria decision-making technique. *Natural hazards*, 83(2), 947-987.
- Khosravi K., H. Shahabi, B. T. Pham, J. Adamowski, A. Shirzadi, B. Pradhan and I. Prakash (2019). A comparative assessment of flood susceptibility modeling using multi-criteria decision-making analysis and machine learning methods. *Journal of Hydrology*, 573, 311-323.
- Krudzlo R. (2010). Flash Flood Potential Index for the Mount Holly Hydrologic Service Area. A Microsoft PowerPoint presentation available at: http://www.state.nj.us/drbc/library/documents/Flood_Website/flood-warning/user-forums/Krudzlo_NWS.pdf.
- Lee M. J., J. E. Kang, and S. Jeon (2012). Application of frequency ratio model and validation for predictive flooded area susceptibility mapping using GIS. In *2012 IEEE international geoscience and remote sensing symposium* (pp. 895-898). IEEE.
- Lee S., J. C. Kim, H. S. Jung, M. J. Lee, and S. Lee, (2017). Spatial prediction of flood susceptibility using random-forest and boosted-tree models in Seoul metropolitan city, Korea. *Geomatics, Natural Hazards and Risk*, 8(2), 1185-1203.
- Liu Y. B., and F. De Smedt (2005). Flood modeling for complex terrain using GIS and remote sensed information. *Water resources management*, 19(5), 605-624.
- Mardani A., A. Jusoh, K. Nor, Z. Khalifah, N. Zakwan, and A. Valipour (2015). Multiple criteria decision-making techniques and their applications—a review of the literature from 2000 to 2014. *Economic research-Ekonomska istraživanja*, 28(1), 516-571.
- Mindje R., L. Li, A. C. Amanambu, L. Nahayo, J. B. Nsengiyumva, A. Gasirabo, and M. Mindje (2019). Flood susceptibility modeling and hazard perception in Rwanda. *International journal of disaster risk reduction*, 38, 101211.
- Minea G. (2013). Assessment of the flash flood potential of Basca river catchment (Romania) based on physiographic factors. *Open Geosciences*, 5(3), 344-353.
- Moore I. D., and R. B. Grayson (1991). Terrain-based catchment partitioning and runoff prediction using vector elevation data. *Water Resources Research*, 27(6), 1177-1191.

- Moore I. D., and J. P. Wilson (1992). Length-slope factors for the revised universal soil loss equation: simplified method of estimation. *Journal of Soil and Water Conservation* 47(5):423-428
- Nandi A., A. Mandal, M. Wilson, and D. Smith (2016). Flood hazard mapping in Jamaica using principal component analysis and logistic regression. *Environmental Earth Sciences*, 75(6), 465.
- Pham B. T., T. V. Phong, H. D., C. Qi, N. Al-Ansari, A. Amini, and D. Tien Bui (2020a). A comparative study of kernel logistic regression, radial basis function classifier, multinomial naïve bayes, and logistic model tree for flash flood susceptibility mapping. *Water*, 12(1), 239.
- Pham B. T., M. Avand, S. Janizadeh, T. V. Phong, N. Al-Ansari, L. S. Ho, and I. Prakash (2020b). GIS based hybrid computational approaches for flash flood susceptibility assessment. *Water*, 12(3), 683.
- Popa M. C., D. Peptenatu, C. C. Drăghici, and D. C. Diaconu (2019). Flood hazard mapping using the flood and flash-flood potential index in the Buzău River catchment, Romania. *Water*, 11(10), 2116.
- Prăvălie R., and R. Costache (2013). The vulnerability of the territorial-administrative units to the hydrological phenomena of risk (flash-floods). Case study: the subcarpathian sector of Buzău catchment. *Analele Universității din Oradea–Seria Geografie*, 23(1), 91-98.
- Rahmati O., H. R. Pourghasemi, and H. Zeinivand (2016). Flood susceptibility mapping using frequency ratio and weights-of-evidence models in the Golastan Province, Iran. *Geocarto International*, 31(1), 42-70.
- Santangelo N., A. Santo, G. D. Crescenzo, G. Foscari, V. Liuzza, S. Sciarrotta, and V. Scorpio (2011). Flood susceptibility assessment in a highly urbanized alluvial fan: the case study of Sala Consilina (southern Italy). *Natural Hazards and Earth System Sciences*, 11(10), 2765-2780.
- Sharma A. (2010). Integrating terrain and vegetation indices for identifying potential soil erosion risk area. *Geo-Spatial Information Science*, 13(3), 201-209.
- Sharma I., S. K. Mishra, and A. Pandey (2021). A simple procedure for design flood estimation incorporating duration and return period of design rainfall. *Arabian Journal of Geosciences*, 14(13), 1-15.
- Singh G., and A. Pandey (2021). Evaluation of classification algorithms for land use land cover mapping in the snow-fed Alaknanda River Basin of the Northwest Himalayan Region. *Applied Geomatics*, 1-13.
- Smith G. (2003). Flash flood potential: Determining the hydro-logic response of FFMP basins to heavy rain by analyzing their physiographic characteristics; <http://www.cbrfc.noaa.gov/papers/ffwpap.pdf>, 11p.
- Tehrany M. S., B. Pradhan, and M. N. Jebur (2014). Flood susceptibility mapping using a novel ensemble weights-of-evidence and support vector machine models in GIS. *Journal of hydrology*, 512, 332-343.
- Tehrany M. S., B. Pradhan, and M. N. Jebur (2015a). Flood susceptibility analysis and its verification using a novel ensemble support vector machine and frequency ratio method. *Stochastic environmental research and risk assessment*, 29(4), 1149-1165.
- Tehrany M. S., B. Pradhan, S. Mansor, and N. Ahmad (2015b). Flood susceptibility assessment using GIS-based support vector machine model with different kernel types. *Catena*, 125, 91-101.
- Tincu R., G. Lazar, and I. Lazar (2018). Modified flash flood potential index in order to estimate areas with predisposition to water accumulation. *Open Geosciences*, 10(1), 593-606.
- Xie K., K. Ozbay, Y. Zhu, and H. Yang (2017). Evacuation zone modeling under climate change: A data-driven method. *Journal of Infrastructure Systems*, 23(4), 04017013.
- Zaharia L., R. Costache, R. Prăvălie, and G. Ioana-Toroimac (2017). Mapping flood and flooding potential indices: a methodological approach to identifying areas susceptible to flood and flooding risk. Case study: the Prahova catchment (Romania). *Frontiers of Earth Science*, 11(2), 229-247.
- Zaharia L., R. Costache, R. Prăvălie, and G. Minea (2015). Assessment and mapping of flood potential in the Slănic catchment in Romania. *Journal of Earth System Science*, 124(6), 1311-1324.
- Zogg J., and K. Deitsch (2013). The flash flood potential index at WFO Des Moines. National Oceanic and Atmospheric Administration: Silver Spring, MD, USA.

Flood Inundation Mapping and Depth Modelling using Machine Learning algorithms and Microwave data

Gyan Prakash^{1*}, Praveen Kumar Gupta², G Venkata Rao¹ and Deva Pratap¹,

¹Department of Civil Engineering, National Institute of Technology Warangal, Telangana, 506004, India

²Space Applications Centre, ISRO, Ahmedabad, Gujarat, 380015, India

*Email: prakas_191854@student.nitw.ac.in

(Received: Aug 10, 2021; in final form: Oct 6, 2021)

Abstract: Flooding is one of the most devastating natural hazards that significantly impact human life and property. During floods, monitoring and mapping flood extent is crucial in identifying the flood-affected areas and the damage assessment. Space-based monitoring of floods can provide a systematic, spatial, timely, and impartial way to monitor disastrous floods. The study area is a part of the Kosi River in the Bihar state. In this study, using microwave remote sensing data (Sentinel - 1), an independent and open-source tool was developed to monitor the flooding extent and water depth. The tool consists of a hybrid model and a floodwater depth analysis model: The hybrid model is fully automated in which Binarization techniques and Random Forest Classifier (RFC) and K Nearest Neighbor (KNN), supervised Machine Learning(ML) algorithms were used. Using flood inundation maps and Digital Elevation Model (DEM), the floodwater depth analysis model (PyQGIS standalone tool) was developed to calculate the flood water depth. Supervised classification algorithms in the hybrid model were further compared and found that the performance of both the KNN and RFC classifiers was close enough, but the time taken by RFC was less than KNN Classifier. The model results were compared and validated with the August 2017 flood event results over the Darbhanga district. The results of the fully automated model have shown a deviation of 0.9% to 19% compared with the published results over the Darbhanga district. The present study suggests that the RFC ML algorithm can classify the SAR data into flooded and non-flooded areas. The developed tool can be used to monitor floods in near/real-time to issue warnings to the people and rescue operations.

Keywords: Flood Inundation, Floodwater Depth, Microwave Remote Sensing, Machine Learning Algorithms, Supervised Classification

1. Introduction

Flood is one of the most devastating natural hazards which is caused due to excessive increase in surface runoff, heavy rainfall, rise in the riverbed, cyclones, and cloud bursts, etc. (Singh, 2015). Among the nations in the world, India is one of the most flood-affected countries due to its unique geo-climatic conditions, precipitation patterns, topographic features, population growth, urbanization, industrialization, etc. (Mohanty et al., 2020). According to National Flood Commission, out of a total geographical area of approximately 329 million hectares, about 40 million hectares are prone to floods (Sharma et al., 2016; Gangwar et al., 2013). Among all the river basins in India, Ganga and Brahmaputra river basins experience the highest number of floods (Mohanty et al. 2020).

It is essential to have information about their intensities and extents to cope with the damage caused by floods. Therefore, the preparation of flood inundation maps is the primary step for damage control and assessing a flood event (Matgen et al., 2007). Compared to in-situ measurement, remote sensing offers practical ways to observe and monitor the surface water dynamics at multiple spatial and temporal scales. There are generally two types of remote sensing datasets are available for the purpose of monitoring the surface water – the optical and microwave remote sensing data. Optical data has been widely used to monitor and map surface water bodies due to the high availability and suitable Spatio-temporal resolutions (Chang Huang et al., 2019). Although the optical data is numerously used for surface water body extraction, the data has several limitations. The most

serious one is that the optical data doesn't have the ability to penetrate through the clouds (Shen et al., 2019), which are mainly prevalent during the monsoon season. Microwave sensors are the alternative sources to overcome the drawbacks of optical sensors. Due to the usage of longwave radiation, microwave sensors can penetrate through the clouds and detailed vegetation coverage. Microwave sensors are independent of solar radiation, and they can provide the data in all weather conditions (Chang Huang et al., 2018; Shen et al., 2019).

Several studies have been carried out for flood inundation mapping and damage assessment using microwave data (Anusha and Bharathi 2020; de Groeve 2010; Gouweleeuw et al. 2011; D. C. Mason et al. 2012; Matgen et al. 2007; Schumann and Moller 2015; Shen et al. 2019; Temimi et al. 2005; Tripathi et al. 2020, 2020). (Matgen et al. 2007) extracted the flood extent and depth of floodwater using DEM and SAR data with the help of the HEC-RAS river flow model and reported an RMSE of 41cm for flood water depth. Using image segmentation, (David C. Mason et al. 2012) extracted the flood inundation maps in urban and rural areas with an accuracy of 89% and a false-positive rate of 6%. For urban flood pixels using TerraSAR-X, 75% of pixels were accurately identified as water, with a false positive rate of 24%. Tripathi et al. 2020 used the Binarization method for the classification of MODIS and SAR data by selecting threshold values. They reported that MODIS data had shown an overestimation of 21% in the flood area compared with SAR data. Anusha and Bharathi 2020 used SAR and optical data for flood mapping of the August

2017 flood in Uttar Pradesh with the help of thresholding and Unsupervised classification methods.

ML algorithms such as Support vector machine, random forest, K Nearest Neighbor (KNN), Decision Tree (DT), K-means, and iso-data (ISO) cluster have been used in several studies to minimize the human interference and time taken for flood mapping (Benoudjit and Guida 2019; Campolo et al. 1999; D Amitrano 2018; Elsafi 2014; Feng et al. 2015; Schumann and Moller 2015; Shahabi et al. 2020; R. Sinha et al. 2008; Tehrany et al. 2014, 2015). Benoudjit and Guida 2019 developed an algorithm for flood mapping using Sentinel 1 and Sentinel 2 data with the help of NDWI and a supervised Classifier. They reported an overall accuracy of 77 % for the rural and 74.7% for the urban floods. Shahabi et al. 2020 developed an ensemble model using KNN as meta classifier and Weighted base classifier for flood inundation mapping. Thus, from the above studies, it can be interpreted that the hybrid/ensemble model results in higher accuracy than individual models. For automation of flood mapping tools with high accuracy results, hybrid models were developed in several studies (Anusha and Bharathi 2020; Matgen et al. 2007; Tehrany et al. 2014; Twele et al. 2016).

The above studies were mostly done for inundation mapping. Thus, there is a need for a coupled model that can also estimate the floodwater depth along with inundation extent. Floodwater Depth Estimation Tool (FwDET) was used to estimate an approximate water depth of the flood plain (Cohen et al., 2018). In this study, a fully automated coupled model approach for flood mapping and depth modeling was made.

2. Study Area

North Bihar faces heavy damages due to floods in the Kosi river (Bhatt et al., 2010). During the last few years, the Kosi River has changed its flow course by 150 Km and caused damage to human lives and properties every year. For more than five decades, flood control management has been working for this basin but continues to bring harm through its devastating floods every year (R. Sinha et al. 2008). The geomorphological properties of the Kosi River have a significant role in these extensive floods. Kosi flows through the slopes of the Himalayas in Tibet and the Southern slopes in Nepal. After that, it enters into Indian region (Kosi River).

In Himalayan region, only it has three tributaries, Arjun, Tamur and Sun-Kosi. Three gauge/discharge stations along the Kosi River, namely, Barakhshetra, Birpur, and Baltara, were used by Central Water Commission (CWC), India. In which Barakhshetra and Birpur show higher peak discharges than Baltara for the same return period. The annual average discharge at Kosi was found 2236 m³/s, the average monsoon discharge 5156 m³/s being almost five times higher than the non-monsoon discharge 1175 m³/s huge difference the river vulnerable to extensive flooding (R. Sinha et al. 2008). The average elevation in the study

area is 49.81m and 100m max elevation was found in SRTM DEM. Gole and Chitale 1966 reports that the Kosi river is built by large sediment flux, which also plays a vital role in causing westward shifting of Kosi and extensive flooding. Thus, the Kosi river changes its course of flow frequently with a 24 year frequency period and causes a lot of damage in the Northern Bihar region (Bhatt et al. 2010). In August 2008, the Kosi River routed to its old course of flow, followed by the Kosi river 100 years ago, and this flood affected over 2.3 million people in the northern area of Bihar state (Singh et al. 2011). In the present study, taking these damages into account caused by Kosi river flood, a part of Kosi river basin which lies in Bihar of 14,861.535 Km² areas and 112 Km long river was selected study area as shown in Figure 1.

3. Data and Methodology

3.1 Data and Pre-Processing

Active microwave remote sensing data in C band, dual polarization with VV and VH polarization from Sentinel-1 satellite was used. The SAR data over the Kosi river basin was acquired for flood events days - from Alaska Satellite Facility (ASF) as Ground Range Detected (GRD) product with a spatial resolution of 10 m and temporal resolution of 10 to 12 days (Table 1).

It is found in various studies that the VH polarization band is more useful in separating Water and Other Land features (Benoudjit and Guida 2019; Matgen et al. 2007; Tavus et al. 2019; Tripathi et al. 2020; Twele et al. 2016) based on their Backscatter value, which can be derived from SNAP tool and all the classification was done on Sigma0_VH_db band of SAR datasets.

SNAP tool was used for pre-processing of SAR data such as radiometric calibration, speckle filtering, orbit file, geometric correction etc. as shown in Figure 2.

Flooded pixels were identified using binarization techniques as used in (Tripathi et al. 2020) by applying threshold values as a trial and error process. These threshold values can be estimated from the histogram shown in Figure 3 (b). There are two peaks can be seen in the histogram in Figure 3(b). Thus, it can be interpreted that the high peak shows other land features, and the low peak shows water. Water mask band was created using the following math in the "band math" in snap tools.

$$\text{If } \sigma_{o_VH} < t_h \text{ then } 255 * (\sigma_{o_VH} < t_h) \text{ else } 0 * (\sigma_{o_VH} > t_h \ \&\& \ \sigma_{o_VH} \neq 0) \quad (1)$$

Similar equation was used for the VV band. Further, the water mask generated using the above equation was checked and found 78% similarity with a published global water mask data of the Kosi River basin. While this published Global water mask (Pekel, J F., et al. 2016) shows a 50 % probability of flood extent, as shown in Figure 4. Pre-processing of DEM data is performed using QGIS software.

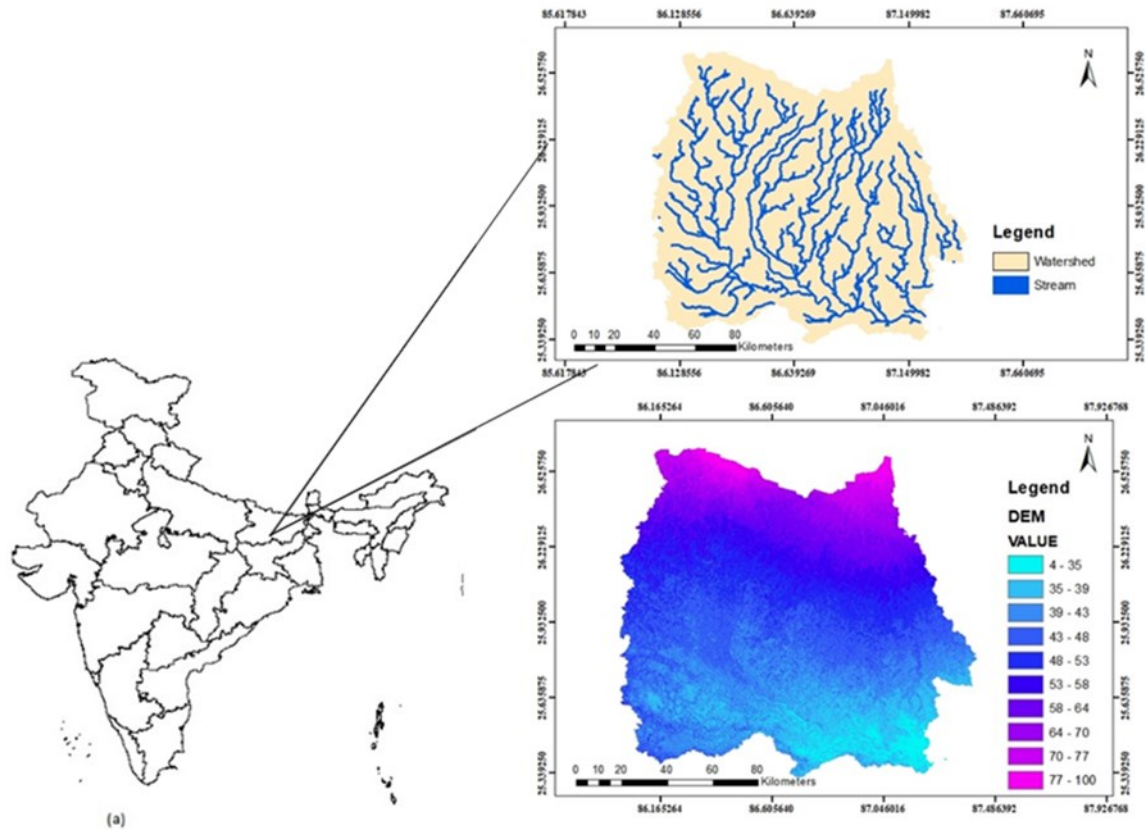


Figure 1. Study area

Table 1. Data used

Data	Type/Format	Source	Acquisition Date	Spatial Resolution	Temporal Resolution	Use	Satellite
SAR	GRD-HD with VH VV Polarization in IW mode	ESA Open Access hub and Alaska Satellite Facility	24/07/2020	10m	12 days	Flood Mapping	Sentinel 1
			11/08/2017, 23/08/2017, 04/09/2017, 16/09/2017	10m	12 days		Sentinel 1
DEM	Raster	USGS		30m		Flood water depth estimation	SRTM

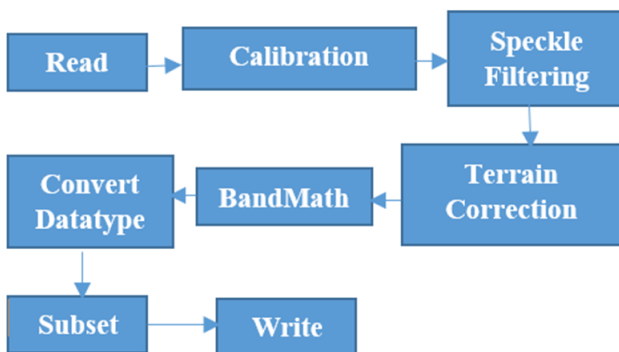


Figure 1. Flowchart of pre-processing

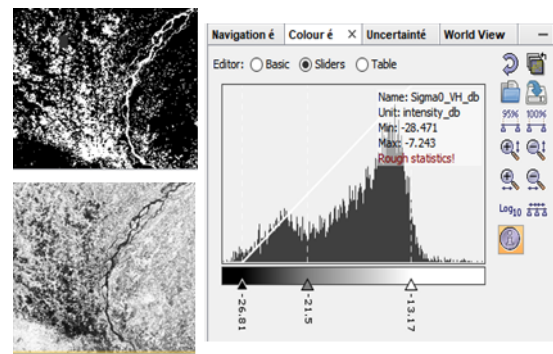


Figure 3. (a) SNAP tool interface for SAR pre-processing (b) Backscatter value histogram

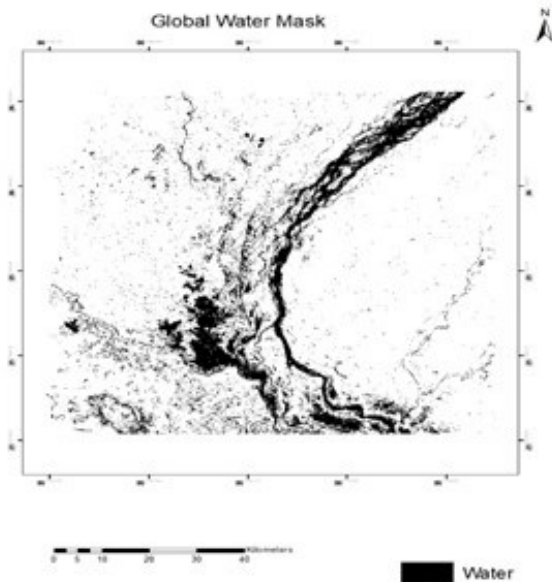


Figure 4. Surface water mask (source: global surface water product)

3.2 Methodology

The main objective of this study is to develop an automated model which will have the potential to provide flood inundation extent and water depth in near real-time. Automated flood mapping and water depth estimation was done in two stages. In the first stage, flood inundation extent was estimated using a hybrid model, which was developed using Machine learning-based supervised classifiers (mainly RFC and KNN). In the second stage, flood extents maps were used along with DEM to estimate floodwater depth maps using the PyQGIS tool based on FwDET (Cohen et al. 2018). The methods used in this study are shown in Figure 5 as a flowchart; further description of the method is discussed below.

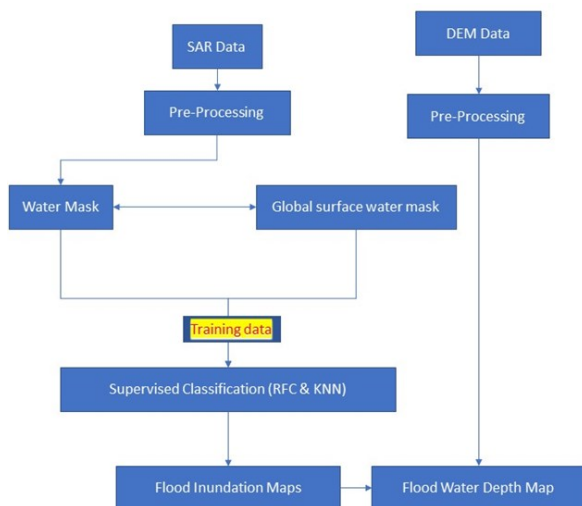


Figure 5. Schematic representation of approach adopted for flood water depth estimation

3.2.1 Hybrid Flood Inundation Model (Classification Using Water Mask and Supervised Machine Learning Algorithm)

This model was developed to get a fully automated approach for flood inundation mapping. The model is

based on the concept of the binarization method and supervised ML algorithms. Binarization includes the selection of threshold backscatter values for water bodies and flooded areas using histogram-based thresholds and published global surface water mask data as ground truth. Further, the flooded and the non-flooded area gets separated as shown in Figure 3(a), top panel window is water mask, the lower one is pre-processed data and histogram of the pixel value is seen in Figure 3(b). There are two peaks can be seen in the histogram in Figure 3(b). Thus, it can be interpreted that the taller peak shows other land features, and the smaller peak shows water.

It was found that the pixel value of the water surface was very close to the value same as under the second smaller peak of the histogram. The threshold value for water in this study area varies from -19db to -22db, and using a "band math" tool in SNAP software water mask was created by applying equation (1) in Sigma0_VH_db band image shown in Figure 6(b). This water mask was updated using a published global surface water mask (Pekel, J F., et al. 2016). Further, the water mask band was used as ground truth data for RFC and KNN supervised classification.

Water mask had labeled data of flooded area as 255 and non-flooded area as 0 shown in Figure 6 (b). The labeled information is used as training datasets for the machine learning models. N_estimator (RFC parameter) was set to a value of 100 whereas six neighbors were selected in the KNN algorithm. Models estimated inundations are shown in Figure 8.

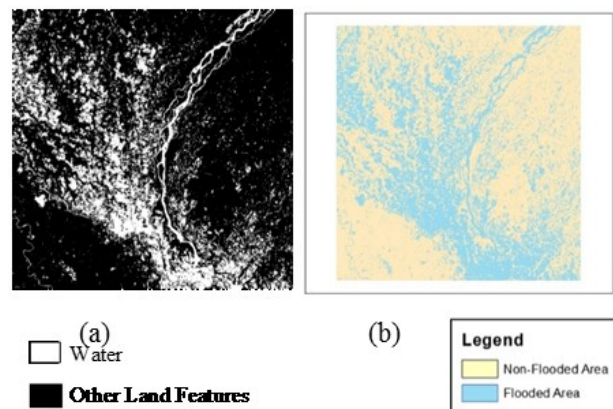


Figure 6. (a) Water Mask (b) Sigma0_VH_db band image

3.2.2 Floodwater Depth Analysis Model

Floodwater depth was estimated with the help of an inundation map and DEM using PyQGIS script and FwDET tool developed by (Cohen et al. 2018). This tool was applied by taking input from the hybrid flood inundation model output. Further, to get the elevation value of pixels in inundation maps was converted into vector form of polygons. These polygons consist of flooded areas and non-flooded areas. Flooded area polygon with grid id of 255 was extracted and merged into a single polygon. So that, these inundated area polygons were further converted into polylines, which can serve as the flood area extent boundary line. The elevation value for these boundary lines was extracted from DEM and a

surface interpolated within this boundary line using grow distance tool as in QGIS. The interpolated surface zones. Flood water depth was found after subtracting the surface created within flood extent with DEM in raster format, and each pixel shows the flood water depth at that location in meters. The structure of this depth estimation tool is shown in Figure 7.

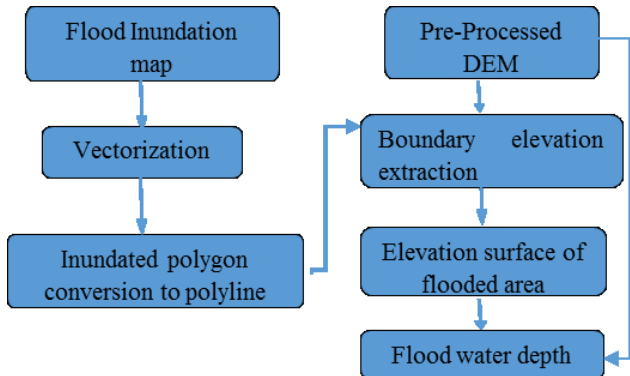


Figure 7. Flow chart of Flood Water Depth Analysis Model

The concept of floodwater depth estimation is constructed from the property of water, i.e., as compared with boundary elevation value, water surface also shows the same elevation value with its boundary of extent. This concept helps in determining the flood water depth of the inundated areas in a river basin. The classified maps show flood extent in the study area, and a floodwater depth map was generated using this tool, as shown in Figure 10.

4. Result and validation

4.1 Hybrid model based inundation

The random forest model results flood inundation map, which shows 5432 Km² under non-flooded area and 2517 Km² as flooded area. The KNN model estimated 5892 Km² as non-flooded area and 2057 Km² under flooded area. The algorithms, KNN and RFC, show nearly the same flood extent and demonstrated an accuracy of 0.9719 and 0.9726, respectively with ground truth data used in this study. This classification report shows that both Classifiers perform well with a very little difference in performance, but the time taken by KNN classifiers was 28hr, whereas the RFC algorithm takes only 6hr. The confusion matrix, as shown in Figure 10, was generated to assess the classification results.

The confusion matrix shows the performance of KNN and RFC in identifying the flooded and non-flooded area, e.g., in Figure 9 model based on the RFC classifier method identifies 28114541 flooded pixels and 11968 number of pixels confused as a flooded pixel. On the other hand, 57936144 pixels were considered non-flooded pixels and confused in 1990969 pixels as flooded areas. A similar result was found in RFC classifiers.

A floodwater depth map was generated using the algorithm for water depth estimation discussed above, and it is shown in Figure 7. Flood extent from the machine learning approach was used to prepare the Flood depth map shown in Figure 10. A total area of 2515 Km² was found inundated in the flood water depth map using an RFC-based flood inundation map. While 145 Km² area of the inundated part was found overestimated as it shows 0 m flood water depth and further spatial variation of flooded water is shown in table 2.

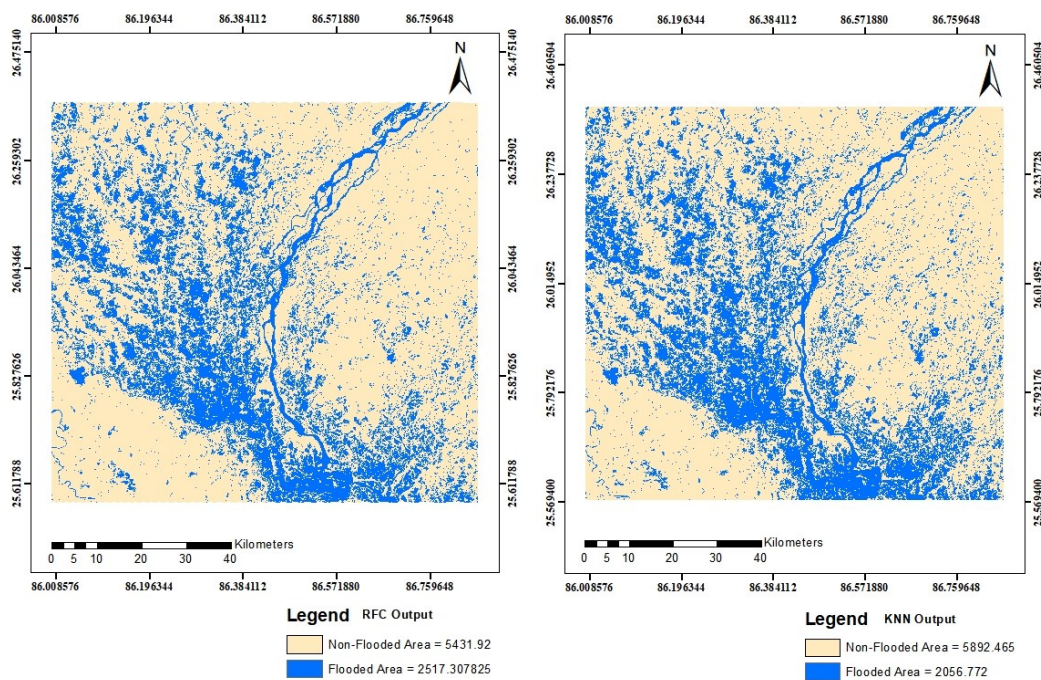


Figure 8. Flood inundation map using RFC (left) and KNN (right) based hybrid model

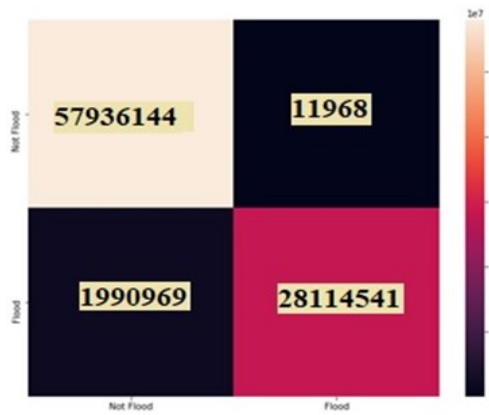


Figure 9. Confusion Matrix of Model

Table 2. Flood water depth Information (26/07/2020)

Depth (m)	Area (Km ²)
0-0.25 m	814.1034
0.25-0.5m	468.1819
0.5-1m	504.8314
1 - 2m	386.8695
2-3m	126.88
3-5m	60.27397
5-10m	9.004411
>10 m	0.098399

Flood Water Depth Map(26/07/2020)

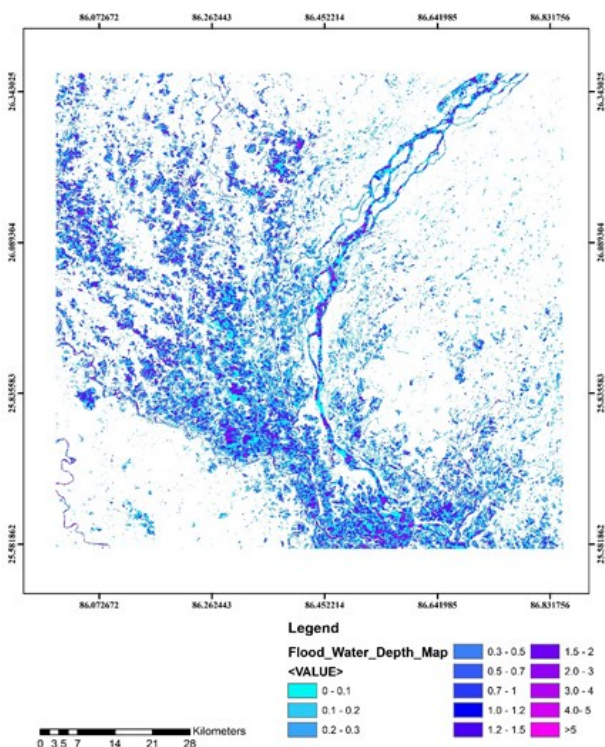


Figure 10. Flood Depth Map using Flood water depth analysis model

4.2 Validation

Further validation of these models results was done with the flood mapping of Darbhanga district 2017 Tripathi et al. 2020. SAR data of 11/08/2017, 23/08/2017, 04/09/2017, and 16/09/2017 dates were used to map inundation using the Binarization technique. The flood inundation map generated by Tripathi et al. 2020 and hybrid model based inundation in the present study were compared for validation. On August 23, 2017, heavy runoff was calculated using TRMM and IMD rainfall products found in (Tripathi et al. 2020).

According to a published study, most inundation area was observed on August 23, 2017. Similarly, model results also show the most flood inundated area on August 23, as shown in Figure 11. Flooded and the non-flooded area were also calculated. Published data shows underestimated whereas model-derived area shows slightly over estimated results. Flood maps estimated using the model can be rectified using a water depth map derived using floodwater depth tool. Floodwater depth maps for different dates are shown in Figure 11.

The automated model shows the flooded area as 104.6, 820, 536 Km², and 371.4 Km² on 11/08/2017, 23/08/2017, 04/09/2017, and 16/09/2017, respectively. When compared with previous studies, these flooded areas found that the flooded area estimated using this model is slightly overestimated, varying from 14.9% to 70% before rectification was done.

To calculate the depth of flooded water, DEM was used to extract the elevation values. Flood water depth information of the study area is shown in the table. Water depth was estimated and found that in the study area during August and September month there was a max water level of 13 meters, as also shown in table 3. There were also some pixels showing a 0-meter depth of water, and these pixels were considered a non-flooded area which was confused by the model as a flooded area. After removing 0 m pixels from the flooded area, it was found that the final Flood Inundation map, along with flood water depth information, was deviating from 0.9% to 19.33 % respective to the published flood map as provided in the table 3.

Thus, depth map accuracy depends on the resolution of DEM. In this study, DEM of 30m spatial resolution was used, and in any case, when a single pixel of 30 meters covers an area where some portion is inundated, and the rest is dry land, then it might happen that the site will be classified as flooded or non-flooded zone thus it could affect the accuracy of the model.

From this study, it can be suggested that coupled model addressing water extent and depth is highly useful to analyze flood events. Figure 11 shows varying flood water depth over Darbhanga district in August and September 2017.

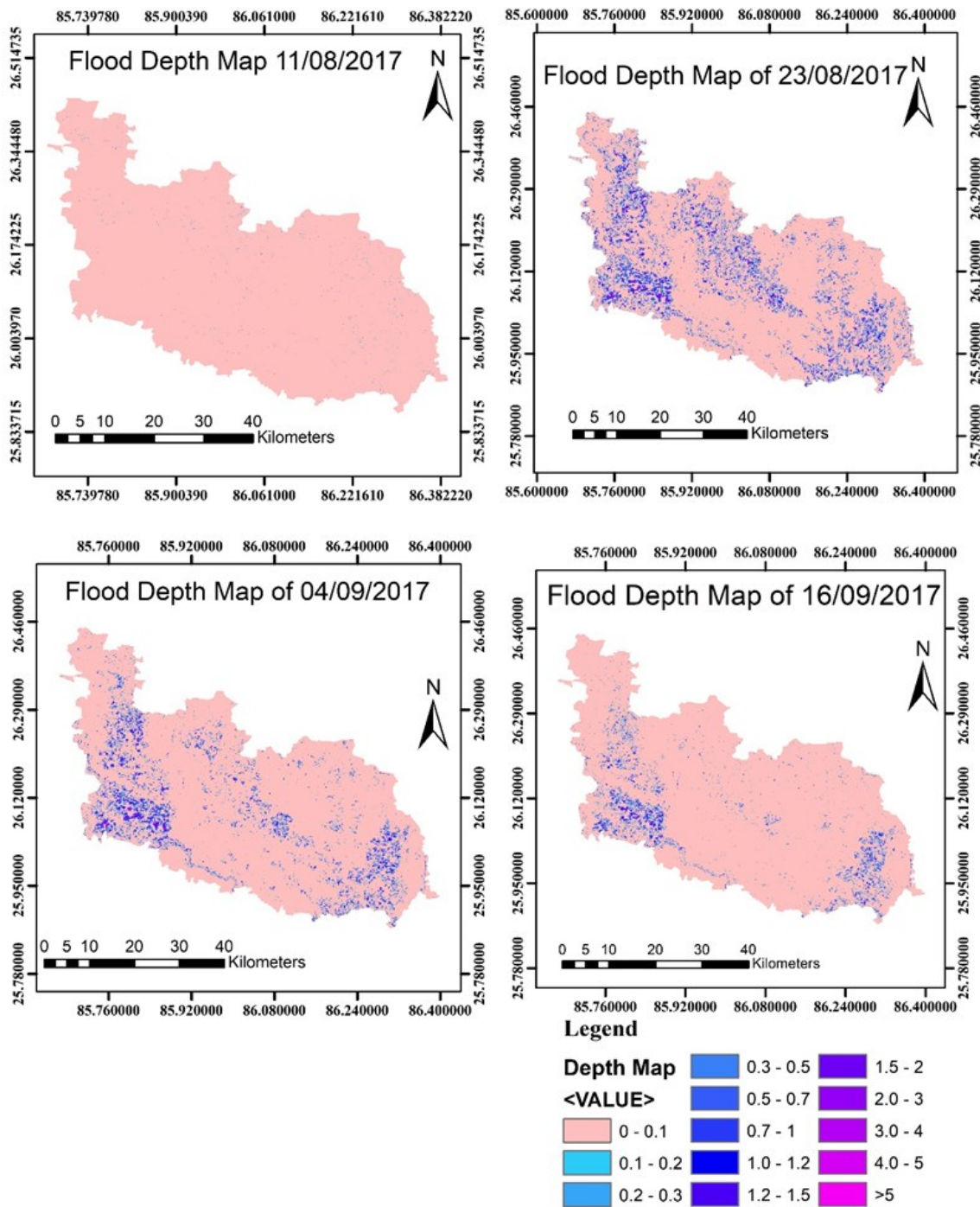


Figure 11. Flood water depth map of Darbhanga 2017 flood

Table 3 Floodwater depth of Darbhanga district 2017 flood

Date	0-1m depth(Km ²)	1-5m depth(Km ²)	5-10m depth(Km ²)	10-13m depth (Km ²)	Total Area (Km ²) (Hybrid Model)	Total Inundated Area in (Tripathi et al. 2020)	Percentage Deviation from previous study(Tripathi et al. 2020)
11/08/2017	20.62	0.051	0	0	21	36	13.88 %
23/08/2017	488.50	70.609	0.626	0.0364	560	554	0.90%
04/09/2017	316.66	41.48	0.388	0.0453	358	330	8.64%
16/09/2017	205.93	18.39	0.023	0	224	188	19.33%

5. Conclusions

In this study, different methods of flood inundation mapping were used using active Microwave C band SAR data. Because the SAR C band having a higher wavelength can penetrate dense clouds and even thin vegetative canopy, thus even in dense cloudy conditions, the SAR image provides precise information. Machine learning classification algorithms, e.g., K- nearest neighbor and Random Forest classifiers, were used, and it was found that the Random Forest classifier gives better results. Inundated surface estimates were also compared with published data over the Darbhanga District and found in good agreement. Subsequently, estimated inundation along with DEM was used to estimate water depth using PyQGIS standalone tool. As mentioned above, all the methods used in the study were packaged to develop an independent and open-source tool to monitor the flooding extent and water depth. This tool consists of a hybrid model for inundation extents and a Flood water depth analysis model. The present study suggests that the RFC ML algorithm can be used to classify the SAR data into flooded and non-flooded areas. The developed tool can be used for monitoring floods in near real-time for rescue operations. The greatest advantage of this tool is that it works independently. ML algorithm for classification and its automation for flood mapping makes this tool usable on any platform. The tool could be most helpful for monitoring flood damages and their effect.

References

- Anusha N., and B. Bharathi (2020). Flood detection and flood mapping using multi-temporal synthetic aperture radar and optical data. *Egyptian Journal of Remote Sensing and Space Science*, 23(2), 207–219.
- Benoudjit A., and R. Guida. (2019). A novel fully automated mapping of the flood extent on sar images using a supervised classifier. *Remote Sensing*, 11(7).
- Bhatt C. M., G. Srinivasa Rao, P. Manjushree and V. Bhanumurthy (2010). Space based disaster management of 2008 Kosi floods, North Bihar, India. *Journal of the Indian Society of Remote Sensing*, 38(1), 99–108.
- Campolo M., P. Andreussi and A. Soldati (1999). River flood forecasting with a neural network model, 35(4), 1191–1197.
- Cohen S., G. R. Brakenridge, A. Kettner, B. Bates, J. Nelson, R. McDonald, Y. F. Haung, D. Munasinghe and J. Zhang (2018). Estimating Floodwater Depths from Flood Inundation Maps and Topography. *Journal of the American Water Resources Association*, 54(4), 847–858.
- Amitrano D, G. D. Martino, A. Iodice, D. Riccio and G. Ruello (2018). Unsupervised rapid flood mapping using Sentinel-1 GRD SAR images. *IEEE Trans Geosci Remote Sens*, 56(6), 3290–3299.
- de Groeve, T. (2010). Flood monitoring and mapping using passive microwave remote sensing in Namibia. *Geomatics, Natural Hazards and Risk*, 1(1), 19–35.
- Elsafi S. H. (2014). Artificial Neural Networks (ANNs) for flood forecasting at Dongola Station in the River Nile , Alexandria Engineering Journal, 53(3), 655–662. <https://doi.org/10.1016/j.aej.2014.06.010>
- Feng Q., J. Gong, J. Liu and Y. Li (2015). Flood mapping based on multiple endmember spectral mixture analysis and random forest classifier-the case of yuyao, China. *Remote Sensing*, 7(9), 12539–12562.
- Gole C. V., and S. V. Chitale (1966). Inland Delta Building Activity of Kosi River. *Journal of the Hydraulics Division*, 92(2), 111–126.
- Gouweleeuw B., C. Ticehurst, P. Dyce, J. P. Guerschman, A. I. J. M. Van Dijk and P. Thew (2011). An experimental satellite-based flood monitoring system for southern Queensland, Australia. 34th International Symposium on Remote Sensing of Environment - The GEOSS Era: Towards Operational Environmental Monitoring.
- Peke, J.F., A. Cottam, N. Gorelick and A. S. Belward (2016) High-resolution mapping of global surface water and its long-term changes. *Nature* 540, 418–422.
- Mason D. C., G. J. P. Schumann, J. C. Neal, J. Garcia-Pintado and P. D. Bates (2012). Automatic near real-time selection of flood water levels from high resolution Synthetic Aperture Radar images for assimilation into hydraulic models: A case study. *Remote Sensing of Environment*, 124, 705–716.
- Mason David C., I. J. Davenport, J. C. Neal, G. J. P. Schumann and P. D. Bates (2012). Near real-time flood detection in urban and rural areas using high-resolution synthetic aperture radar images. *IEEE Transactions on Geoscience and Remote Sensing*, 50(8), 3041–3052.
- Matgen P., G. Schumann, J. B. Henry, L. Hoffmann and L. Pfister (2007). Integration of SAR-derived river inundation areas, high-precision topographic data and a river flow model toward near real-time flood management. *International Journal of Applied Earth Observation and Geoinformation*, 9(3), 247–263.
- Mohanty, M. P., S. Mudgil and S. Karmakar (2020). Flood management in India: A focussed review on the current status and future challenges. *International Journal of Disaster Risk Reduction*, 49(July 2019), 101660.
- Schumann G. J. P., and D. K Moller (2015). Microwave remote sensing of flood inundation. *Physics and Chemistry of the Earth*, 83–84, 84–95.
- Shahabi H., A. Shirzadi, K. Ghaderi, E. Omidvar, N. Al-Ansari, J. J. Clague, M. Geertsema, K. Khosravi, Ata Amini, S. Bahrami, O. Rahmati, K. Habibi, A. Mohammadi, H. Nguyen, A. M. Melesse, B. B. Ahmad and A. Ahmad. (2020). Flood detection and susceptibility mapping using Sentinel-1 remote sensing data and a machine learning approach: Hybrid intelligence of bagging ensemble based on K-Nearest Neighbor classifier. *Remote Sensing*, 12(2).
- Shen X., D. Wang, K. Mao, E. Anagnostou and Y. Hong (2019). Inundation extent mapping by synthetic aperture radar: A review. *Remote Sensing*, 11(7), 1–17.
- Singh S. K., A.C. Pandey and M.S. Nathawat (2011). Rainfall variability and spatio temporal dynamics of flood inundation during the 2008 Kosi flood in Bihar State,

India. *Asian Journal of Earth Sciences*, 4(1), 9–19.

Singh D.A. (2015). *Floods in India: Cause and Control*

Sinh R., G.V. Bapalu, L. K. Singh and B. Rath, B. (2008). Flood risk analysis in the Kosi river basin, north Bihar using multi-parametric approach of Analytical Hierarchy Process (AHP). *Journal of the Indian Society of Remote Sensing*, 36(4), 335–349

Sivanpillai R., K. M. Jacobs, C. M. Mattilio and E.V. Piskorski (2020). Rapid flood inundation mapping by differencing water indices from pre- and post-flood Landsat images. *Frontiers of Earth Science* 2020 15:1, 15(1), 1–11.

Tavus B., S. Kocaman, H. Nefeslioglu and C. GÖKÇEOĞLU (2019). Flood Mapping Using Sentinel-1 SAR Data: A Case Study of Ordu August 8 2018 Flood. *International Journal of Environment and Geoinformatics*, 6(3), 333–337.

Tehrany M. S., B. Pradhan and M. N. Jebur (2014). Flood susceptibility mapping using a novel ensemble weights-of-evidence and support vector machine models in GIS.

Journal of Hydrology, 512, 332–343.

Tehrany M. S., B. Pradhan, S. Mansor, and N. Ahmad (2015). Flood susceptibility assessment using GIS-based support vector machine model with different kernel types. *Catena*, 125, 91–101.

Temimi M., R. Leconte, F. Brissette and N. Chaouch (2005). Flood monitoring over the Mackenzie River Basin using passive microwave data. *Remote Sensing of Environment*, 98(2–3), 344–355.

Tripathi G., A. C. Pandey, B. R. Parida, and A. Kumar (2020). Flood Inundation Mapping and Impact Assessment Using Multi-Temporal Optical and SAR Satellite Data: a Case Study of 2017 Flood in Darbhanga District, Bihar, India. *Water Resources Management*, 34(6), 1871–1892.

Twele A., W. Cao, S. Plank, and S. Martinis (2016). Sentinel-1-based flood mapping: a fully automated processing chain. *International Journal of Remote Sensing*, 37(13), 2990–3004.

An integrated approach of flood risk assessment over a severely flood-prone coastal region using geomorphic classifiers, and socio-economic indicators

Mohit Prakash Mohanty^{1,2}, K.V.H Durga Rao³ and Subhankar Karmakar^{2,4,5*},

¹Department of Water Resources Development and Management, Indian Institute of Technology Roorkee, Roorkee 247 667, India

²Environmental Science and Engineering Department, Indian Institute of Technology Bombay, Mumbai 400 076, India

³Disaster Management Support Division, National Remote Sensing Centre, Balanagar, Hyderabad-500625, Telangana, India

⁴Interdisciplinary Program in Climate Studies, Indian Institute of Technology Bombay, Mumbai, 400076, India

⁵Centre for Urban Science and Engineering, Indian Institute of Technology Bombay, Mumbai, 400076, India

*Email: skarmakar@iitb.ac.in

(Received: Aug 10, 2021; in final form: Oct 06, 2021)

Abstract: The present study explores the efficacy of readily available geomorphic classifiers and socio-economic indicators to characterize flood risk over Jagatsinghpur district, a severely flood-prone coastal region in the Mahanadi River Basin. A set of twelve relevant geomorphic classifiers are derived from the high-resolution CartoDEM topographic data through linear binary classification to identify flood hazard zones. On the other side, twenty-one socio-economic indicators are considered through multivariate Data Envelopment Analysis (DEA) to derive socio-economic vulnerability at the village level. Flood risk at the village level is calculated as the combination of geomorphic flood hazard and socio-economic vulnerability. The flood risk zones derived by utilizing geomorphic classifiers are compared to those derived through a comprehensive 1D 2D coupled hydrodynamic modeling. Inundation along the floodplains near the rivers and coastal regions is well captured through both geomorphic analysis and hydrodynamic modeling. A vast majority of villages experience low and very low vulnerability, while only a few face high and very high vulnerability, mainly secluded to Ersama, Jagatsinghpur, Tirtol Nuagaon, and Baligaon talukas. A high degree of similarity in flood risk proves the reliability of the proposed approach for the estimation of flood risk. Given the acute problem of floods, the proposed methodology, characterized by low computational cost, lesser data requirement, and limited flood modeling complexity, may facilitate local authorities and planners deriving effective flood management strategies.

Keywords: flood risk, geomorphic classifiers, hazard, riverine flooding, vulnerability

1. Introduction

It is well known that floods account for the most pervasive mortality and economic damages among all known weather-related natural disasters (Ward et al., 2017; Dottori et al., 2018). Recently, AoN- the leading global professional services firm, reported that global flood events that occurred during March 2019 alone accounted for a mammoth USD 8 billion of economic losses (<https://www.preventionweb.net/news/view/64911>). The worrying fact is that flood events have been increasing manifold, majorly driven by climate change impacts and changes in socio-economic dynamics, as indicated by several research articles (Blöschl et al., 2017; Thober et al., 2018; Mohanty and Simonovic, 2021b). A recent report by Rentschler and Salhab (2020) prepared for the World Bank highlights that a staggering 1.47 billion people globally live within high flood risk zones. It further apprises that although countries at all levels of development face various degrees of flood risk, the vast majority of the exposed population, i.e., ~ 89% reside in the low- and middle-income countries, most widespread impacts of floods noticed over South-Asia.

One way of comprehending this emerging concern is by quantifying flood risk, which provides a transparent knowledge of the regions and how they are affected by flooding (Trigg et al., 2016; Wing et al., 2019). As per the standard definition, flood risk is the product of flood hazard and vulnerability (Hagenlocher et al., 2018; Mohanty et al., 2020b; Sajjad et al., 2020). Flood hazard is considered the tangible component of flood risk and is quantified based on the degree of depth and velocity of

inundated water over the region (Kourgialas and Karatzas, 2011; Costabile et al., 2020). On the other hand, vulnerability is the intangible component and determines the susceptibility of various domains, including humans, physical features, and the environment, to flood damages (Wing et al., 2020; Paprotny et al., 2021). Several approaches quantifying flood hazards and can be categorized into empirical, simple conceptual, and hydrodynamic models (Teng et al., 2017). Empirical models adopt straightforward approaches to retrieve flood information from past observations. In the last two decades, the usability of remotely sensed data and GIS has been widely explored in quantifying flood hazards. The recently launched satellites, such as SWOT, RADARSAT-2, TerraSAR-X, COSMO-SkyMed, and Sentinel-1, contain sophisticated sensors that facilitate in capturing high-resolution images at a faster time (Teng et al., 2017). In particular, satellite images derived from Synthetic aperture radar (SAR) that can overcome cloud cover have been found to help identify flooded regions (Zhan et al., 2021; Clement et al., 2018). The algorithms considered in the process also make it possible to distinguish between permanent water bodies and inundated areas, allowing flooded boundaries to be identified with a high degree of accuracy (Gebremichael et al., 2020). Hydrodynamic models are mathematical models designed to replicate fluid motion by solving St. Venant's equations and are considered the most sophisticated approach (Afshari et al., 2018; Wing et al., 2019). Usually, they consider a wide range of inputs such as topographic (e.g., digital elevation model; DEM, underwater topography, built-up area, and artificial drainage network), hydrologic (e.g., streamflow, lake discharge, point source), and meteorological (e.g.,

rainfall, snowfall) to derive flood hazard. In most cases, the availability of the datasets is a daunting task, and even more while dealing with data-scarce flood-prone regions existing in several developing and under-developed nations. Based on the representation of flood inundation dynamics, hydrodynamic models can be further grouped into one-dimensional (1D), two-dimensional (2D), and three-dimensional (3D) models.

Although hydrodynamic models are competent in deriving precise flood hazard information, their usage may be limited in some instances due to (i) scarcity of extensive data inputs, (ii) in comprehensive performance over large and complex terrains, (iii) high computational cost and time, and (iv) lack of expertise in handling model simulations by a non-technical user. An alternative computationally less extensive solution is to utilize the river basin's topography to identify flooding patterns (Adnan et al., 2019; Mishra and Sinha, 2020). In particular, hydrological extremes and floods accelerate erosion, transport, and deposition processes, and over extended periods can shape and form geomorphic features. Few studies have recently developed DEM-based floodplain delineation methods to compare the topographic surface and a reference water level. The identification of flood-prone areas is demonstrated through linear binary classification techniques that have proven to be an appealing tool characterized by simple requirements regarding input data, costs, and computational times (Manfreda et al., 2014, 2015). The classifiers include single features (e.g., slope, contributing area, distance to the nearest channel, topographic convergence, etc.) and composite features formulated with the specific aim to represent a metric of flood hazard. **Table 1** enlists recent efforts made to map flood hazards through geomorphic classifiers.

Despite the encouraging usage of geomorphic classifiers in identifying flood-prone regions, their efficacy in flood risk mapping, which requires information on flood hazard and socio-economic vulnerability, has not been explored. Most of the studies have limited their analysis to identifying flood susceptible zones without looking further into the flood hazard component. Moreover, past studies have focussed on geomorphic studies over inland areas affected by riverine flooding; their performance over coastal regions has not been reported so far. It is widely known that coastal environments identified by multiple flood drivers are the most susceptible to flooding (Kron, 2013; Vousdoukas et al., 2018; Tiggeloven et al., 2020). In such regions, the inland areas are inundated from riverine overflow due to extreme rainfall during the monsoon. At the same time, the coastal stretches are affected by storm tide (combination of astronomical tide and storm surge) impacts. The present study explores the efficacy of geomorphic classifiers in flood risk mapping over a severely flood-prone coastal region in India. A set of relevant single and composite classifiers are considered to derive flood hazard zones. The socio-economic vulnerability is quantified at the finest administrative scale of the village level over the study area. The hazard identified by the best performing geomorphic classifier is considered along with the socio-economic vulnerability to

derive different levels of flood risk. The flood risk derived by utilizing the geomorphic approach is compared with the other flood risk map developed by using hazard derived from a comprehensive 1D 2D coupled inundation modeling. At last, both the flood risk maps are compared to establish the geomorphic classifier's efficacy in quantifying flood risk.

2. Description of the study area

Jagatsinghpur district is situated between 19° 58' N to 20° 23' N latitude and 86° 3' E to 86° 45' E longitude in the flood-prone delta region of the lower Mahanadi river basin in the state of Odisha, India (Figure 1). It is well-known as a severe flood-prone area in India (Mohapatra, 2015; Sahoo and Bhaskaran, 2018; Mohanty et al., 2021a). The region falls within the deltaic zones of two major rivers, namely, River Mahanadi and Devi. The district receives an annual average rainfall of 1451.60 mm, majorly from the South-west monsoon. It has a coastline spanning up to ~50 km that faces constant tidal disturbances. The tide is semi-diurnal with the maximum Highest High Water Level (HHWL) of +3.5 m and a minimum Lowest Low Water Level (LLWL) of +0.7 m relative to the chart datum (Gopikrishna and Deo, 2018). Morphologically, more than half of the region is relatively flat (< 4.5 m) (Muralikrishnan et al., 2013), which prolongs the stance of floodwater. Moreover, being predominantly agrarian (~66%), the district is subjected to substantial socio-economic setbacks very frequently in terms of losses in crop production, loss of livestock, and fisheries due to floods almost every year (Mohanty et al., 2020b).

3. Proposed framework and methodology

The proposed framework is illustrated in Figure 2. The flood hazard analysis is carried out using geomorphic classifiers, which are implemented on the DEM. In this study, we considered the CartoDEM of horizontal resolution 10m. CartoDEM is an Indian product synthesized from the Cartosat-1 stereo payload launched in May 2005 by ISRO's Polar Satellite Launch Vehicle (PSLV-C5). Previous studies have reported the high accuracy of CartoDEM while accounting for flood inundation modeling (Mohanty et al., 2020a). Both single and composite classifiers are considered to depict the flood hazard zones. Later, the best performing geomorphic classifier is selected to create the representative geomorphic flood hazard map. Another flood hazard map is derived through a comprehensive 1D 2D coupled hydrodynamic modeling. Village-level socio-economic vulnerability is quantified by considering 21 socio-economic indicators through Data Envelopment Analysis (DEA). The hazard (both geomorphic and hydrodynamic) and socio-economic vulnerability information are aggregated to create two flood risk maps at the village level. A step-by-step disposition of the proposed methodology is described in the following sections.

3.1 Identification of flood hazard zones through geomorphic classifiers

Numerous physical features describe the morphology of a river basin.

Table 1. Recent efforts made to map flood hazard through geomorphic classifiers

Indicators	Case study	DEM	Remarks	References
Modified topographic index (TIm) $TI_m = \log \frac{a_d^n}{\tan(\beta)}$ ad is drained area per unit contour length; and $\tan(\beta)$ is local gradient.	Arno river basin, Italy (8,830 km ²)	DEM obtained from Arno River Basin Authority (20m) SRTM DEM (90 m) ASTER DEM (30 m) National elevation data (30 m)	The index is highly sensitive to DEM resolution; however, a cell size of ~100 m is sufficient for good performance. SRTM DEM showed good performance when compared with the other DEMs.	Manfreda et al. (2011)
Surface curvature (H) Laplacian of the elevation (ΔH) Contributing area (A) Local slope (S)	Tanaro river basin, Italy (8,000 km ²)	SRTM: DEM-VOID (Void filled) and DEM-CON (Hydrologically conditioned) from HydroSHEDS	The classifiers could identify 93% of flood-prone areas while validated with the flood inundation map.	Degiorgis et al. (2012)
Single features Upslope contributing area, As (m ²) Surface curvature ($\nabla^2 H$) Local slope, S Distance from the nearest stream, D (m) Elevation to the nearest stream, H (m).	Tiber River Basin, Italy (17,375 km ²)	-do-	Elevation to the nearest stream (H), downslope index (DWi), and GFi showed better performance. Among the single features, Distance from the nearest stream (D) and Elevation to the nearest stream (H) performed better, while among composite indices $\ln[h_l/H]$ and $\ln[hr/H]$ performed better. Composite indices were found to be less sensitive to the variations in DEM resolution.	Manfreda et al. (2014)
Composite indices Modified topographic index (TIm) Downslope index, (DWi) Ratio between the flow distance (D) and elevation (H) $\ln[h_l/H]$; where h_l is the variable water depth GFI (Geomorphic Flood Index): $\ln[hr/H]$; hr is computed as a the function of the contributing area Ar $[hr-H]/\tan(\alpha d)$ and $[hr - H]/D$.	Bradano River Basin, Italy (2765 km ²)	-do-		Manfreda et al. (2015)
	Bulbula river sub-catchment, Ethiopia	-do-	Elevation difference (H) and the composite index $\ln[hr/H]$ showed the best performance.	Samela et al. (2016)
	Ohio River Basin, US, (29,000 km ²)	-do-	GFI was the most suitable morphologic classifier, as it exhibited a higher accuracy than the other indices.	Samela et al. (2017)

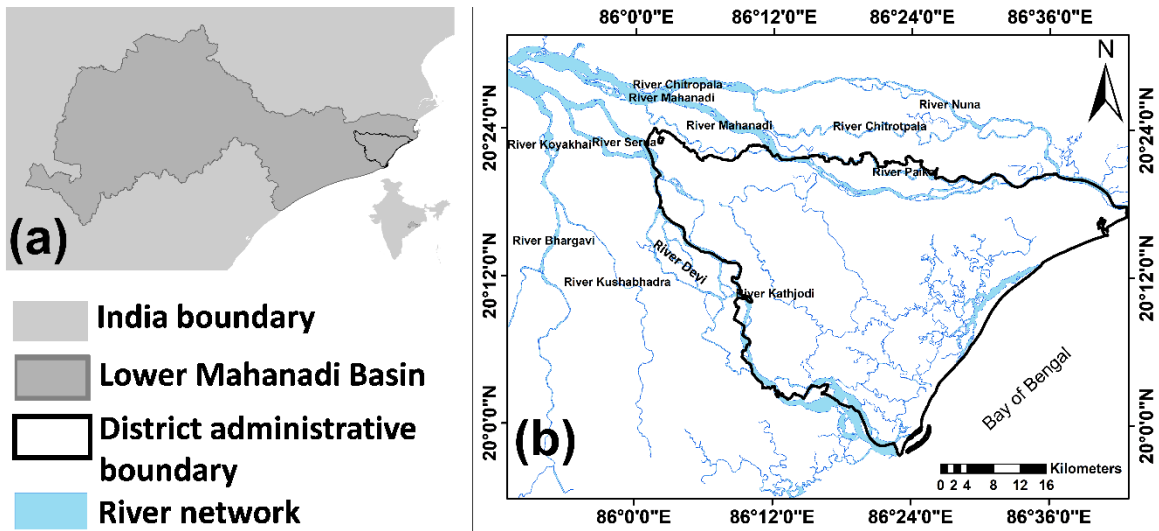


Figure 1. Description of the study area: (a) Location of Jagatsinghpur in the lower Mahanadi river basin; (b) River network in Jagatsinghpur district.

In this study, we considered the relevant indicators that are explicitly capable of capturing flood wave propagation and flood hazards. For example, a few indicators characterize the tendency of the flood water to be accumulated over specific locations over the study area or the tendency of gravitational force to allow the floodwater to move downstream (Samela et al., 2017). Based on this criterion, twelve geomorphic features were finalized. Among them, five were single geomorphic classifiers, while the rest were composite geomorphic classifiers. The composition of single classifiers proposes the latter set of classifiers to estimate the water depth that is calculated as a function of the contributing area. The selected geomorphic classifiers are described below.

Single geomorphic classifiers

1. Upslope contributing area, **A** (m²): the upslope area of the region that contributes to runoff to the point of focus;
2. Surface curvature, $\nabla^2 H$: Laplacian of the elevation;
3. Local slope, **S**: maximum value of slope among the eight possible flow directions;
4. Flow distance to the nearest stream, **D** (m): hydrologic distance from the point under focus to the closest point of the river drainage network;
5. Elevation difference to the nearest stream, **H** (m): the difference between the point's elevation under focus and the final point of the above-identified path.

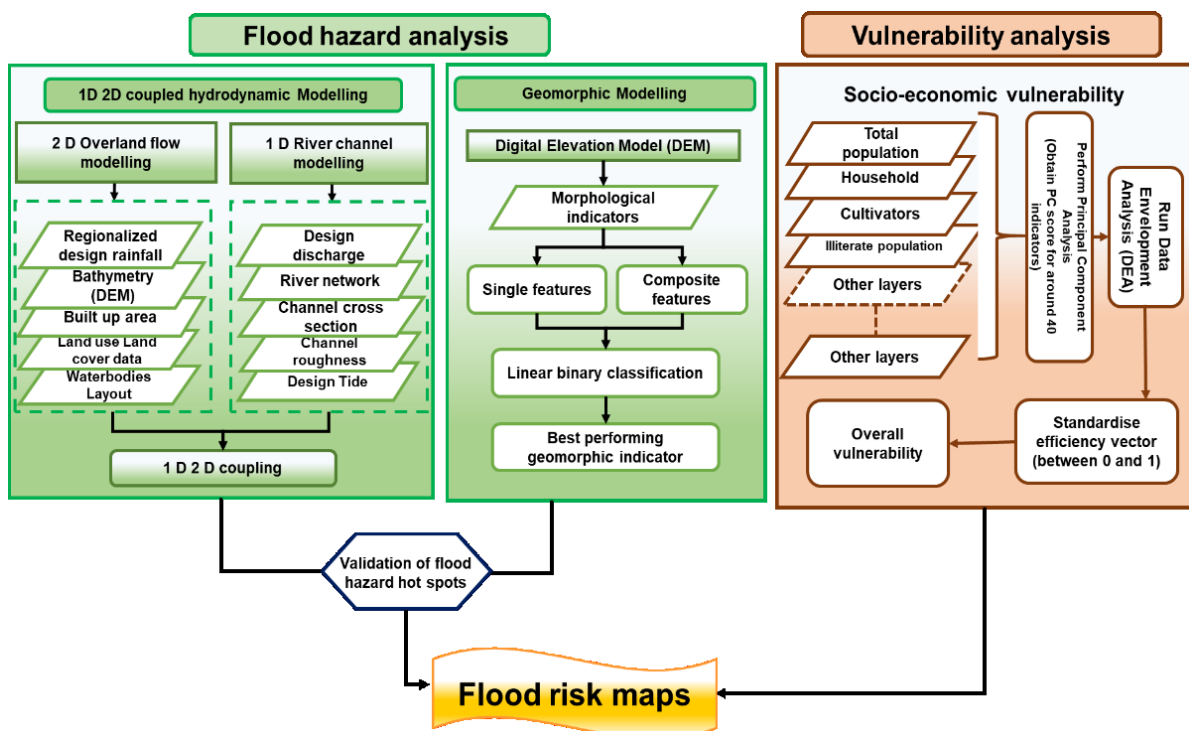


Figure 2. The proposed framework of flood risk mapping considering flood hazards derived through geomorphic analysis and 1D-2D hydrodynamic modeling, and Socio-economic vulnerability analysis.

Composite geomorphic classifiers

1. Modified topographic index(TI_m): it is mathematically represented as,

$TI_m = \ln \left[\frac{a_d^n}{\tan(\beta)} \right]$ where a_d (m) is the drained area per unit contour length; $\tan(\beta)$ is the local gradient, and n is an exponent whose value is taken as less than 1.

2. Downslope index: it is mathematically represented as

$$\tan(a_d) = \frac{d}{L_d}$$

where, L_d (m) is the distance that an amount of water has to travel along its flow path to lose potential energy equal to d (m).

3. H/D: where H is the elevation difference, and D is the flow distance to the nearest stream

4. $\ln(h_r/H)$: where, h_r is the water depth, and H is the elevation difference.

5. $\ln(h_r/H)$: h_r is determined as a function of the upslope contributing area A in the nearest point of the river drainage network hydrologically connected to the point under focus.

6. $(h_r-H)/\tan(\alpha_d)$: representing the change between water depth h_r and the elevation difference H divided by a surrogate of the hydraulic gradient represented by the downslope index, and

7. $(h_r-H)/D$: change between water depth h_r and the elevation difference H divided by the distance D.

3.2 1D 2D coupled hydrodynamic modeling

The flood inundation modeling was carried out using the MIKE FLOOD model (DHI, 2019). MIKE FLOOD encompasses the 1D version in MIKE 11 for river channel modeling and the 2D version in MIKE 21 HD for overland or flood plain inundation modeling. The MIKE 11 employs an implicit finite difference scheme developed by Abbott and Ionescu (1967) for solving the Saint-Venant equations, regardless of them being kinematic, diffusive, or dynamic. This robust scheme can support courant numbers as high as 10-20 for subcritical flow (with a Froude number less than 1). The governing equations in the MIKE 11 are continuity and momentum equations, as expressed in equations 1 and 2.

$$\frac{\partial Q}{\partial x} + \frac{\partial A}{\partial t} = q \tag{1}$$

$$\frac{\partial Q}{\partial t} + \frac{\partial(\alpha \frac{Q^2}{A})}{\partial x} + gA \frac{\partial h}{\partial x} + \frac{gQ|Q|}{C^2AR} = 0 \tag{2}$$

where Q is the discharge (m³/s), A is the cross-sectional area (m²), q is the lateral inflow (m³/s/m), h is the stage above datum (m), C is the Chezy's roughness coefficient (m^{1/2}/s), R is the hydraulic radius (m), α is the momentum distribution coefficient (s²/m³), g is the gravitational acceleration (m/s²), and x and t are the distance (m) and time (s), respectively.

MIKE 21 HD model employs a non-orthogonal unstructured triangular mesh and is based on the numerical solution of the two-dimensional incompressible Reynolds-averaged Navier-Stokes equations using the assumptions of Boussinesq and hydrostatic pressure. The model functions on a finite element method (FEM) scheme and solves the fully dynamic shallow water equations as expressed in equations (3), (4), and (5)

$$\frac{\partial \zeta}{\partial t} + \frac{\partial p}{\partial x} + \frac{\partial q}{\partial y} = \frac{\partial d}{\partial t} \tag{3}$$

$$\frac{\partial p}{\partial t} + \frac{\partial}{\partial x} \left(\frac{p^2}{h} \right) + \frac{\partial}{\partial y} \left(\frac{pq}{h} \right) + gh \frac{\partial \zeta}{\partial x} - \frac{gp\sqrt{p^2+q^2}}{C^2h^2} - \frac{1}{\varphi_w} \left[\frac{\partial}{\partial x} (h\tau_{xx}) + \frac{\partial}{\partial y} (h\tau_{xy}) \right] - \Omega_q - fVV_x + \frac{h}{\varphi_w} \frac{\partial}{\partial x} (p_a) = 0 \tag{4}$$

$$\frac{\partial q}{\partial t} + \frac{\partial}{\partial y} \left(\frac{q^2}{h} \right) + \frac{\partial}{\partial x} \left(\frac{pq}{h} \right) + gh \frac{\partial \zeta}{\partial y} + \frac{gp\sqrt{p^2+q^2}}{C^2h^2} - \frac{1}{\varphi_w} \left[\frac{\partial}{\partial y} (h\tau_{yy}) + \frac{\partial}{\partial x} (h\tau_{xy}) \right] + \Omega_p - fVV_y + \frac{h}{\varphi_w} \frac{\partial}{\partial x} (p_a) = 0 \tag{5}$$

The following symbols notations are used in the equations:

$h(x, y, t)$	Water depth ($=\zeta - d, m$)
$d(x, y, t)$	Time-varying water depth (m)
$\zeta(x, y, t)$	Surface elevation (m)
$p, q(x, y, t)$	Flux densities in x-and y-directions (m ³ /s/m)= (uh, vh) ; (u,v) = depth averaged velocities in x- and y-directions
$C(x, y)$	Chezy resistance (m ^{1/2} /s)
G	Acceleration due to gravity (m/s ²)
$f(V)$	Wind
$V, V_x, V_y(x, y, t)$	Wind speed and components in x- and y-direction (m/s)
$\Omega_{x,y}$	Coriolis parameter, latitude dependant (s ⁻¹)
$p_a(x, y, t)$	Atmospheric pressure (kg/m ² s ²)
φ_w	Density of water (kg/m ³)
x, y	Space coordinates (m)
T	Time (s)
$\tau_{xx}, \tau_{xy}, \tau_{yy}$	Components of effective shear stress

The 1 in 100-yr design storm-tide and design discharge are provided as boundary conditions in MIKE 11, while 1 in 100-yr regionalized design rainfall is provided in MIKE 21 HD. The simulated outputs from MIKE 11 and MIKE 21 HD are coupled in the MIKE FLOOD interface by providing lateral links between river cross-sections and the adjoining floodplains to generate the overland flood inundation. The degree of flood hazard is derived from the flood inundation values and determined as the tuple of depth and velocity (Mohanty et al., 2020b). Extensive details on the validation of flood hazard zones at both 1D and 2D levels is provided in Mohanty et al. (2020a).

3.3 Socio-economic vulnerability

An array of 21 relevant socio-economic for 2011 is selected to determine the village-wise vulnerability values. The details of the indicators are tabulated in Table 2. These indicators are classified into positive (higher the quantity, higher the vulnerability or cost-type) and non-positive (higher the quantity lower the vulnerability or benefit type) categories based on their impacts during flood disasters. The quantitative values of indicators are standardized to reduce the multi-dimensionality, after which Principal Component Analysis (PCA) is performed to decorrelate the indicators further. Data envelopment analysis (DEA) is a widely used nonparametric technique for estimating the relative efficiency of units, referred to as DMUs, when it is difficult to identify absolute measures of efficiency (Mardani et al., 2017; Mohanty et al., 2020).

Table 2. List of positive (*cost-type*), and non-positive (*benefit-type*) indicators

Indicators	Indicators	Justification
Positive (cost-type)	Female Population	A majority of the female population devote their lives to household activities and hence have less scope to participate in educational and social activities.
	Total Population	A larger population leads to increased exposure to floods. They are usually poor and will have a direct adverse effect during a disaster event. The coping ability will also be less, as they need to find some other jobs to fulfill their financial needs
	Main agricultural and cultivators population	They require special attention during evacuation due to their high care needs and susceptibility to health problems and thereby slowing down the processes during the disaster
	Population of Children (population < 6 years)	A higher number of households increases the vulnerability as the number of economic dependents tends to increase
	Number of households	Illiterates tend to have a minor set of employable skills and have reduced access to information with a low level of risk acknowledgment, which increases their vulnerability.
	Illiterate population	Illiterate females may find it more difficult to follow any evacuation warning and take care of the family during a disaster.
	Illiterate female population	The weaker economic sections are categorized as the backward community by the Govt. of India.
	SC and ST population	The weaker economic sections are categorized as the backward community by the Govt. of India.
	SC and ST population	GoI identifies them as part of the backward community. The women in this community have a greater responsibility in taking care of the family during a disaster.
Non- Positive (benefit-type)	SC and ST female population	This community has temporary jobs and mostly landless laborers.
	Marginal workers (including cultivators, agricultural laborers, household Industry, and others)	This community are dependent on adult members in their respective family, and they will be more vulnerable during a disaster event, as their coping ability will be meager
	Non-workers	Unemployed people are vulnerable because of inadequate income and resources to support themselves and recover from disasters. The more unemployed people in a society, the more unstable the society is as more problems may emerge under these adverse circumstances.
	Working population	The coping capacity will be higher in a family during hazards if the female working population is higher in a community.
	Female working population	Literacy rate commonly enhances the knowledge about how to cope during the natural hazards and thus reduces the impact
	Literate Population	The higher the ratio of literate people in a community, the higher the capacity to cope with hazards.
	Female literate population	

Indicators	Indicators	Justification
Non-positive (benefit type)	Amenities (primary education, secondary education, colleges, and medical facilities)	Education can help in creating awareness among the general public in coping with floods. Medical facilities can aid in providing treatment to people during the time of disasters.
	Status of power supplies	The presence of this indicator represents the overall development in the village which positively influences the ability to adapt
	Status of well	It provides a viable source of drinking water during disaster situations
	Status of hand pump	
	Status of river	
Status of tank		

The model optimizes each observation associated with a DMU to calculate a discrete piecewise frontier determined by the set of Pareto efficient DMUs. The efficiency of each DMU is measured by the distance of its input-output vectors to a piecewise linear frontier. In this study, the slack-based input-oriented BCC method (named after Banker, Charnes, and Cooper) (Banker et al., 1984), which considers variable returns to scale (VRS), is considered. The mathematical expressions for deriving the vulnerability is provided in equations 6 to 9.

$$\min [\theta_j - \xi (\sum_{x=1}^X S_x^- + \sum_{x=1}^X S_x^+)] \tag{6}$$

$$\text{such that } \sum_{j=1}^J \lambda_j * PC_{xj} + \sum_{x=1}^X S_x^- = \theta_j * PC_{xj}; \tag{7}$$

$$\forall x = 1, \dots, X \tag{7}$$

$$\sum_{j=1}^J \lambda_j * QC_{xj} - \sum_{x=1}^X S_x^+ = QC_{xj}, \tag{8}$$

$$\forall x = 1, \dots, X \tag{8}$$

$$\sum_{j=1}^J \lambda_j = 1; \lambda_j, \xi, S_x^-, S_x^+ \geq 0 \quad \forall x, j \tag{9}$$

The vulnerability for *jth* village is given by $\mathcal{V}_j = 1 - \theta_j$ where, θ ($0 < \theta < 1$) is the technical efficiency of each village, λ_j is the weight assigned to *jth* village, S_x^- and S_x^+ are the slack and remnant variables. In the last step, the vulnerability indices are discretized into five different classes from very low to very high, based on the values of function f ($i1, \dots, in$). This discretization is done by defining the mapping in \mathcal{V} as given in equations 10 and 11:

$$f_d: \mathcal{V} \rightarrow \mathcal{V}_d; \mathcal{V}_d = \{v_d \in \mathbb{N}: v_d \leq 5\} \tag{10}$$

$$\mathcal{V}_d = \begin{cases} 1, & 0.1 \leq v \leq 0.2 \\ 2, & 0.2 < v \leq 0.3 \\ 3, & 0.3 < v \leq 0.4 \\ 4, & 0.4 < v \leq 0.5 \\ 5, & v > 0.5 \end{cases} \tag{11}$$

where v and v_d represent the value and index of vulnerability for *jth* village

3.4 Flood risk

The flood risk value for each village is calculated as the product of the corresponding flood hazard and socio-economic vulnerability value. Two sets of flood risk maps are derived by considering the hazards derived from geomorphic analysis and hydrodynamic modeling, with the fixed socio-economic vulnerability values. The

gridded hazard values derived through each methodology are converted to village-scale by assigning the median value among the grids falling over the village. In the next step, the hazard is multiplied with the socio-vulnerability value to derive flood risk for the village. Similar to vulnerability, the overall risk values for each village are converted to qualitative scale, namely very-low risk, low-risk, moderate risk, high risk, and very-high risk.

4. Results and discussion

4.1 Geomorphic maps for Jagatsinghpur district

The Single and composite geomorphic maps of the Jagatsinghpur district are illustrated in Figures 3 and 4. In all the figures, we notice a clear and continuous illustration of the geomorphic classifiers, which supports the accurate representation of surface features in the CartoDEM without significant errors. For instance, Figure 3 (d), representing the flow path distance to the nearest stream, captures the river network accurately, appropriately accounting for the geomorphic properties of the study area. The upslope contributing area (Figure 3, a) varied up to 16 km², with maximum values falling between 8 to 10 km², while surface curvature values did not exceed 25 over most parts over the region (Figure 3, b). The local slope values were well captured, clearly identifying the high and low values over the entire area (Figure 3, c). We notice that most of the spots far from the river drainage networks contain a slope between 0 to 0.5, while those near the river drainage networks had a higher slope value.

While analyzing the composite set of classifiers, we again discover a continuous distribution of the geomorphic properties over the entire region. The modified topographic index was well represented, with most of the values falling within 15 (Figure 4, a). As expected, the downslope index was found to be maximum over the floodplains of the Mahanadi and Devi rivers (Figure 4, b). H/D values were found to lie between 0 and 1, with maximum values over the main river channels (Figure 4, c). In (hl/H), and ln (hr/H) classifiers showed similar behavior, with most grid values not exceeding a value of 5 (Figure 4d, and e). More or less similar behavior was also noticed with (hr-H)/ tan (αd) as well (Figure 4, f).

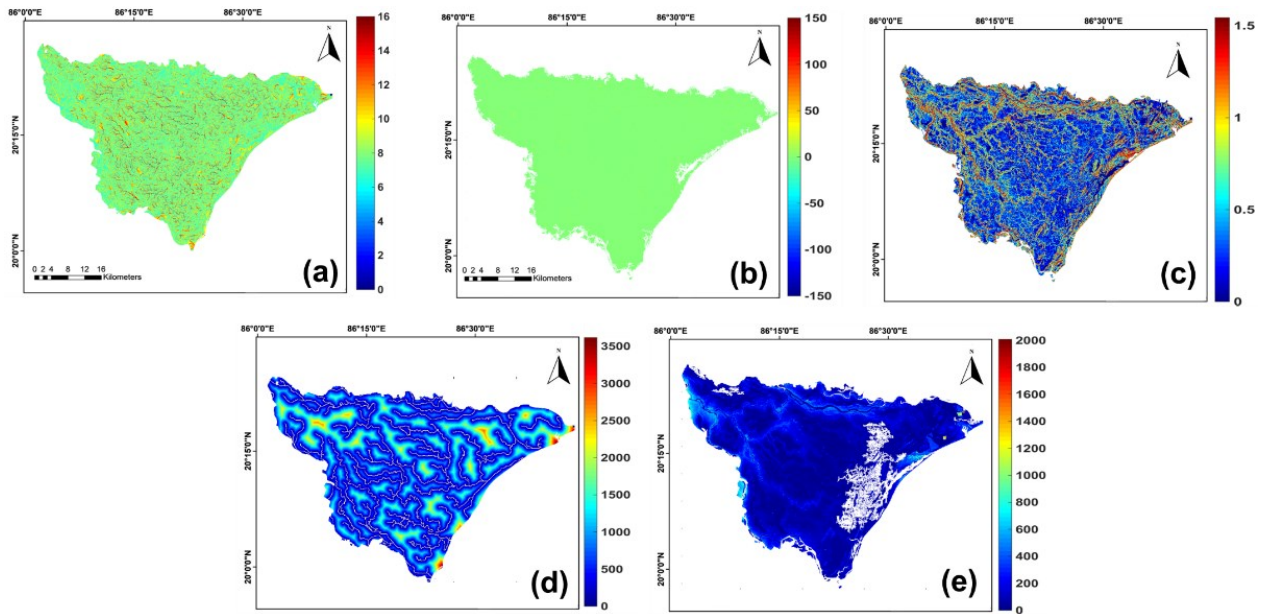


Figure 3. Single geomorphic classifiers-(a) Upslope contributing area, (b) Surface curvature, (c) Local slope , (d) Flow path distance to the nearest stream, and (e) Elevation to the nearest stream- for Jagatsinghpur district derived by using CartoDEM.

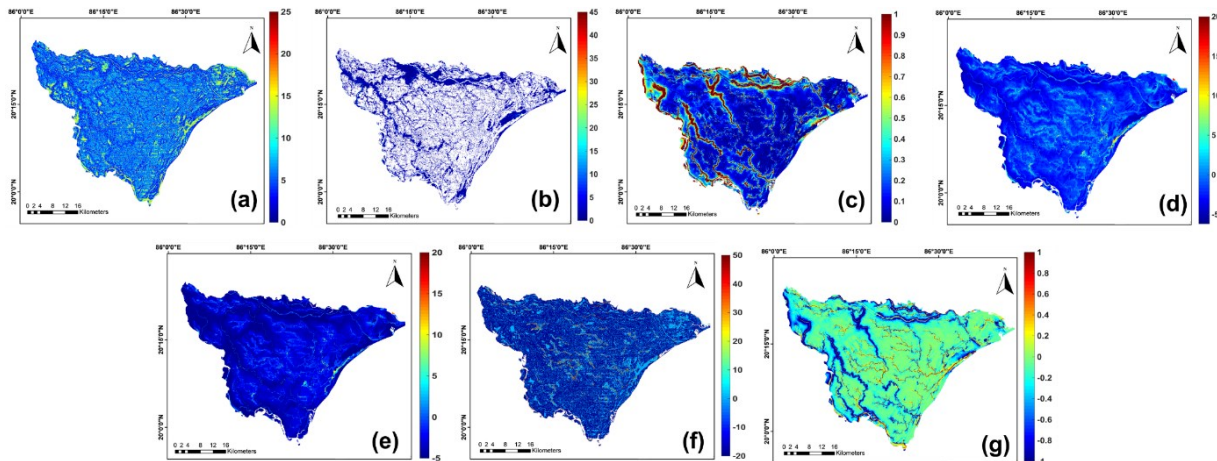


Figure 4. Composite geomorphic classifiers- (a) Modified topographic index, (b) Downslope index, (c) H/D, (d) $\ln(h/H)$, (e) $\ln(hr/H)$, (f) $(hr-H)/\tan(\alpha)$, (g) $(hr-H)/D$ - for Jagatsinghpur district derived by using CartoDEM.

(hr-H)/D composite classifier had a mix of high and low values over the region. We noticed lesser values near the floodplains of the river while higher values in the coastal stretches. However, more than 80 percent of the areas were covered between -0.2 to 0.2 (Figure 4, g). The best geomorphic classifier was selected, after which a representative flood hazard map was created (Figure 5, a)

4.2 Flood hazard maps derived using 1D-2D coupled flood modelling

The 1D-2D coupled hydrodynamic flood inundation was carried out using the MIKE FLOOD model as described in section 3.2. The model was initially run over a flexible mesh domain but was later converted into a rectangular grid of $10m \times 10m$ to comply with the grid resolution of the CartoDEM. The 1 in 100-yr flood hazard map derived through hydrodynamic modeling is illustrated in Figure 5,b. This figure shows the riverine inundation in the lower stretches of the major river networks and coastal inundation in the coastal villages. Significantly, the floodplains of Mahanadi falling in Raghunathpur and

Tirtol tehsils which are well-known to be severely flood-prone spots, were accurately captured. So also, the coastal stretches experiencing coastal flooding impacts in the Ersama, and Kujang tehsils were also accurately captured. Elaborate details on the validation of flood hazard layer both at 1D river channel and 2D overland level are reported in Mohanty et al. (2020a).

4.3 Socio-economic vulnerability maps

The socio-economic vulnerability map is illustrated in Figure 5, c. We notice that a majority of villages face low and very low vulnerability, while only a few experience high and very high vulnerability in the Jagatsinghpur district. The low-, and very-low vulnerable villages are spread all over the district. In contrast, the high and very-high vulnerable ones are secluded mostly to Ersama, Jagatsinghpur, Tirtol, Nuagaon, and Baligaon talukas. The coastal villages in Ersama and Balikuda talukas contain a significant number of highly vulnerable villages. Unlike the previous flood hazard map, we do not notice a similar distribution of vulnerability.

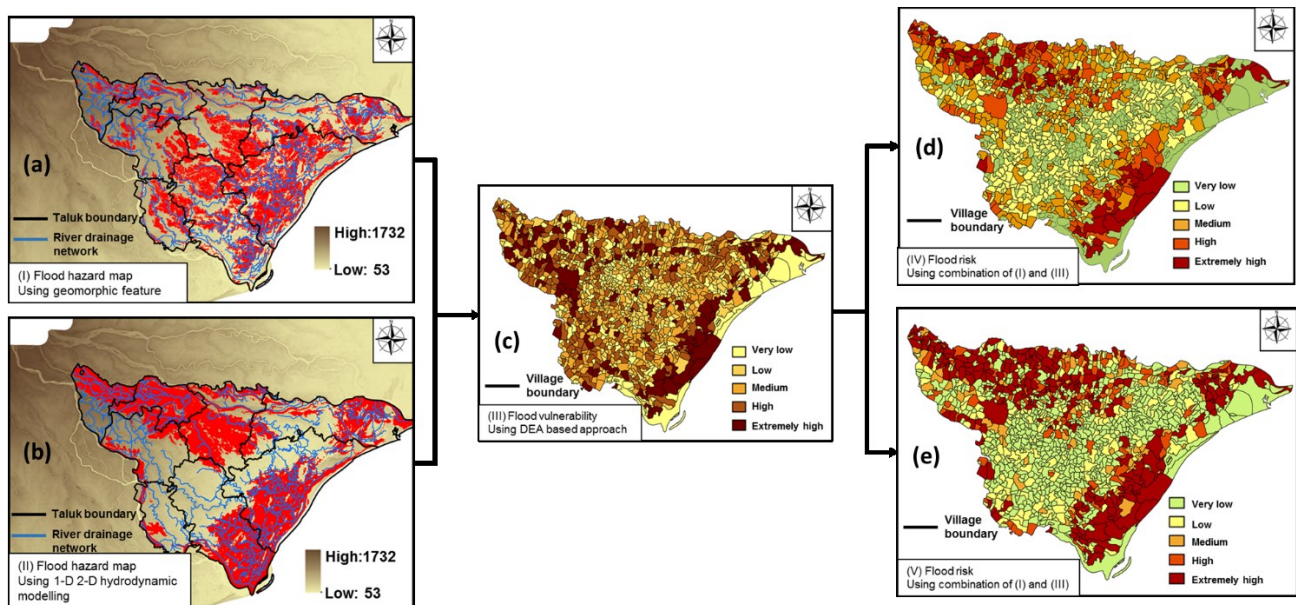


Figure 5. Set of flood-related maps- (a) Representative flood hazard map derived by geomorphic classification; (b) Flood hazard map derived through 1D 2D coupled hydrodynamic modeling, (c) Socio-economic vulnerability map derived through DEA; (d) Flood risk map for the combination of geomorphic flood hazard and socio-economic vulnerability; and (e) Flood risk map for the combination of hydrodynamic flood hazard and socio-economic vulnerability.

For instance, the south-eastern coastal region of Jagatsinghpur contains several villages facing very high vulnerability. At the same time, as we move upwards to the northeastern part, we notice a decline in vulnerability with less vulnerable villages. This is because the socio-economic vulnerability analysis is sensitive due to various influencing socio-economic indicators in the investigation. The North-eastern and western parts contained several high and very high vulnerable villages as well.

4.4 Comparison of flood risk maps

As discussed in Section 3.4, the flood hazard maps from geomorphic analysis and hydrodynamic analysis were considered along with the socio-economic vulnerability map to derive the flood risk map. Figures 5 d and e illustrate the two flood risk maps. We notice a more or less similar pattern in the risk values villages within the Jagatsinghpur district. The risk values over the coastal region through both approaches were well defined.

The impact of coastal inundation was more pronounced in hydrodynamic modeling, resulting in a few more high-risk villages than the other risk map. Similar behavior was also noticed in the floodplains lying near the Mahanadi river and Devi rivers. However, the central part of Jagatsinghpur was very well captured with equal distribution of risk values. In this region, most of the villages experienced very low risk. Overall, we observe that different degrees of risk values are adequately captured through the geomorphic analysis, which promises its application to identify flood risk quickly.

5. Conclusions

The quantification of flood risk is vital for building a comprehensive flood management strategy for any region. A flood risk map containing inherent information on flood

hazards and vulnerability serves as an essential tool for the general public, disaster experts, and civic bodies. Based on the flood risk knowledge, appropriate structural and non-structural measures can be planned to improve the resilience for longer terms.

Although the hydrodynamic-based approach is considered the most sophisticated technology for determining flood hazards, they are often limited due to the technicalities involved and lack of expertise by a non-technical user in handling the model. Under such circumstances, geomorphic classifiers that utilize the basin's topography to determine flood susceptible zones can be considered an alternate option. The determination of hazard zones through various classifiers does not yield much computational cost and time. In this study, we considered a set of 12 relevant geomorphic classifiers to characterize the flood hazard zones. The best performing geomorphic classifier was considered to create the most representative flood hazard map. On the other hand, a 1D 2D coupled flood inundation modeling was carried out at a finer scale. A 1 in 100-yr flood hazard map was generated that considered regionalized design rainfall, design discharge, and design storm-tide as input parameters. The socio-economic vulnerability was determined by considering a suite of 21 socio-economic indicators. The combination of flood hazards was considered along with the socio-economic vulnerability map to derive a flood risk map. The two sets of flood risk maps were found to capture various degrees of risk appropriately. Based on this study, we realize that geomorphic classifiers that are computationally less intensive may be considered in place of the hydrodynamic approach to demarcate flood risk zones, mainly when computational cost and time are a restraint. The regions identified as high-risk areas by geomorphic classifiers can be identified, which may be

further considered for a detailed flood risk mapping considering the hydrodynamic approach. The geomorphic classification will be suitable for large regions, which are flood-prone and have the limitation of hydrodynamic modeling due to high computational cost and time.

Acknowledgments

The research presented here is supported financially by ISRO-IIT (B)- Space Technology Cell(STC) through sponsored projects (Project No. RD/0114-ISROC00-013, and RD/0119-ISROC00-001), and Department of Science and Technology (SPLICE-Climate Change Programme), Government of India through Project reference number DST/CCP/CoE/140/ 2018, Grant Number: 0000000000010013072 (UC ID: 18192442). The authors are grateful to National Remote Sensing Centre, Hyderabad, for allowing access to the MIKE FLOOD model. IIT Bombay has provided support towards computational resources

References

- Abbott M. B., and Ionescu, F. (1967). On the numerical computation of nearly horizontal flows. *Journal of Hydraulic Research*, 5(2), 97-117.
- Adnan M. S. G., Dewan, A., Zannat, K. E., and Abdullah, A. Y. M. (2019). The use of watershed geomorphic data in flash flood susceptibility zoning: a case study of the Karnaphuli and Sangu river basins of Bangladesh. *Natural Hazards*, 99(1), 425-448.
- Afshari S., Tavakoly, A. A., Rajib, M. A., Zheng, X., Follum, M. L., Omranian, E., and Fekete, B. M. (2018). Comparison of new generation low-complexity flood inundation mapping tools with a hydrodynamic model. *Journal of Hydrology*, 556, 539-556.
- Banker R. D., Charnes, A., and Cooper, W. W. (1984). Some models for estimating technical and scale inefficiencies in data envelopment analysis. *Management Science*, 30(9), 1078-1092.
- Blöschl G., Hall, J., Parajka, J., Perdigão, R. A., Merz, B., Arheimer, B., ... and Živković, N. (2017). Changing climate shifts timing of European floods. *Science*, 357(6351), 588-590.
- Clement M. A., Kilsby, C. G., and Moore, P. (2018). Multi-temporal synthetic aperture radar flood mapping using change detection. *Journal of Flood Risk Management*, 11(2), 152-168.
- Costabile P., Costanzo, C., De Lorenzo, G., and Macchione, F. (2020). Is local flood hazard assessment in urban areas significantly influenced by the physical complexity of the hydrodynamic inundation model?. *Journal of Hydrology*, 580, 124231.
- Degiorgis M., Gnecco, G., Gorni, S., Roth, G., Sanguineti, M., and Taramasso, A. C. (2012). Classifiers for the detection of flood-prone areas using remote sensed elevation data. *Journal of Hydrology*, 470-471, 302-315.
- DHI (2019) MIKE FLOOD The integrated water modelling platform <https://www.mikepoweredbydhi.com/products/mikeplus> accessed on 10 July 2021.
- Dottori F., Szewczyk, W., Ciscar, J. C., Zhao, F., Alfieri, L., Hirabayashi, Y., ... and Feyen, L. (2018). Increased human and economic losses from river flooding with anthropogenic warming. *Nature Climate Change*, 8(9), 781-786.
- Gebremichael E., Molthan, A. L., Bell, J. R., Schultz, L. A., and Hain, C. (2020). Flood Hazard and Risk Assessment of Extreme Weather Events Using Synthetic Aperture Radar and Auxiliary Data: A Case Study. *Remote Sensing*, 12(21), 3588.
- Gopikrishna B., and Deo, M. C. (2018). Changes in the shoreline at Paradip Port, India in response to climate change. *Geomorphology*, 303, 243-255.
- Hagenlocher M., Renaud, F. G., Haas, S., and Sebesvari, Z. (2018). Vulnerability and risk of deltaic social-ecological systems exposed to multiple hazards. *Science of the total environment*, 631, 71-80.
- Kourgialas N. N., and Karatzas, G. P. (2011). Flood management and a GIS modelling method to assess flood-hazard areas-a case study. *Hydrological Sciences Journal- Journal des Sciences Hydrologiques*, 56(2), 212-225.
- Kron W. (2005). Flood risk= hazard• values• vulnerability. *Water international*, 30(1), 58-68.
- Kron W. (2013). Coasts: the high-risk areas of the world. *Natural hazards*, 66(3), 1363-1382.
- Manfreda S., Leo, M. Di, and Sole, A. (2011). Detection of Flood-Prone Areas Using Digital Elevation Models. *Journal of Hydrologic Engineering*, 16(10), 781-790.
- Manfreda S., Samela, C., Gioia, A., Gerardo, G., Iacobellis, V., Giuzio, L. (2015). Flood-prone areas assessment using linear binary classifiers based on flood maps obtained from 1D and 2D hydraulic models, *Natural Hazards*, 79, 735-754.
- Manfreda S., Samela, C., Sole, A., and Fiorentino, M. (2014). Flood-Prone Areas Assessment Using Linear Binary Classifiers based on Morphological Indices Salvatore. *Vulnerability, Uncertainty, and Risk*, 2002-2011.
- Mardani A., Zavadskas, E. K., Streimikiene, D., Jusoh, A., and Khoshnoudi, M. (2017). A comprehensive review of data envelopment analysis (DEA) approach in energy efficiency. *Renewable and Sustainable Energy Reviews*, 70, 1298-1322.
- Mishra K., and Sinha, R. (2020). Flood risk assessment in the Kosi megafan using multi-criteria decision analysis: A hydro-geomorphic approach. *Geomorphology*, 350, 106861.
- Mohanty M. P., and Karmakar, S. (2021a). WebFRIS: An efficient web-based decision support tool to disseminate end-to-end risk information for flood management. *Journal of environmental management*, 288, 112456.
- Mohanty M. P., and Simonovic, S. P. (2021b). Changes in floodplain regimes over Canada due to climate change impacts: Observations from CMIP6 models. *Science of The Total Environment*, 148323.

- Mohanty M. P., Nithya, S., Nair, A. S., Indu, J., Ghosh, S., Bhatt, C. M., ... and Karmakar, S. (2020a). Sensitivity of various topographic data in flood management: Implications on inundation mapping over large data-scarce regions. *Journal of Hydrology*, 590, 125523.
- Mohanty M. P., Vittal, H., Yadav, V., Ghosh, S., Rao, G. S., and Karmakar, S. (2020b). A new bivariate risk classifier for flood management considering hazard and socio-economic dimensions. *Journal of environmental management*, 255, 109733.
- Mohapatra M. (2015). Cyclone hazard proneness of districts of India. *Journal of Earth System Science*, 124(3), 515-526.
- Muralikrishnan S., Pillai, A., Narender, B., Reddy, S., Venkataraman, V. R., and Dadhwal, V. K. (2013). Validation of Indian National DEM from Cartosat-1 Data. *Journal of the Indian Society of Remote Sensing*, 41(1), 1–13.
- Paprotny D., Kreibich, H., Morales-Nápoles, O., Castellarin, A., Carisi, F., and Schröter, K. (2020). Exposure and vulnerability estimation for modelling flood losses to commercial assets in Europe. *Science of the Total Environment*, 737, 140011.
- Rentschler J., M. Salhab. 2020. People in Harm's Way: Flood Exposure and Poverty in 189 Countries. Policy Research Working Paper. No. 9447. Washington DC: The World Bank
- Sahoo B., and Bhaskaran, P. K. (2016). Assessment on historical cyclone tracks in the Bay of
- Sajjad M., Lin, N., and Chan, J. C. (2020). Spatial heterogeneities of current and future hurricane flood risk along the US Atlantic and Gulf coasts. *Science of the total environment*, 713, 136704.
- Samela C., Manfreda, S., Paola, F. De, and Giugni, M. (2016). DEM-Based Approaches for the Delineation of Flood-Prone Areas in an Ungauged Basin in Africa. *Journal of Hydrologic Engineering*, 21(2), 1–10.
- Samela C., Troy, T. J., and Manfreda, S. (2017). Geomorphic classifiers for flood-prone areas delineation for data-scarce environments. *Advances in water resources*, 102, 13-28.
- Samela C., Troy, T. J., and Manfreda, S. (2017). Geomorphic classifiers for flood-prone areas delineation for data-scarce environments. *Advances in Water Resources*, 102, 13–28.
- Teng J., Jakeman, A. J., Vaze, J., Croke, B. F., Dutta, D., and Kim, S. (2017). Flood inundation modelling: A review of methods, recent advances and uncertainty analysis. *Environmental modelling and software*, 90, 201-216.
- Thober S., Kumar, R., Wanders, N., Marx, A., Pan, M., Rakovec, O., ... and Zink, M. (2018). Multi-model ensemble projections of European river floods and high flows at 1.5, 2, and 3 degrees global warming. *Environmental Research Letters*, 13(1), 014003.
- Tiggeloven T., Moel, H. D., Winsemius, H. C., Eilander, D., Erkens, G., Gebremedhin, E., ... and Ward, P. J. (2020). Global-scale benefit–cost analysis of coastal flood adaptation to different flood risk drivers using structural measures. *Natural Hazards and Earth System Sciences*, 20(4), 1025-1044.
- Trigg M. A., Birch, C. E., Neal, J. C., Bates, P. D., Smith, A., Sampson, C. C., ... and Fewtrell, T. J. (2016). The credibility challenge for global fluvial flood risk analysis. *Environmental Research Letters*, 11(9), 094014.
- Vousdoukas M. I., Mentaschi, L., Voukouvalas, E., Verlaan, M., Jevrejeva, S., Jackson, L. P., and Feyen, L. (2018). Global probabilistic projections of extreme sea levels show intensification of coastal flood hazard. *Nature communications*, 9(1), 1-12.
- Ward P. J., Jongman, B., Aerts, J. C., Bates, P. D., Botzen, W. J., Loaiza, A. D., ... and Winsemius, H. C. (2017). A global framework for future costs and benefits of river-flood protection in urban areas. *Nature climate change*, 7(9), 642-646.
- Wing O. E., Pinter, N., Bates, P. D., and Kousky, C. (2020). New insights into US flood vulnerability revealed from flood insurance big data. *Nature communications*, 11(1), 1-10.
- Wing O. E., Sampson, C. C., Bates, P. D., Quinn, N., Smith, A. M., and Neal, J. C. (2019). A flood inundation forecast of Hurricane Harvey using a continental-scale 2D hydrodynamic model. *Journal of Hydrology X*, 4, 100039.
- Zhan P., Zhu, W., and Li, N. (2021). An automated rice mapping method based on flooding signals in synthetic aperture radar time series. *Remote Sensing of Environment*, 252, 112112.

Atmospheric Rivers and Flood Events in Ganga and Brahmaputra River Basins

Nimisha Singh*, Rohit Pradhan and R. P. Singh

Land Hydrology Division, EPSA, Space Applications Centre (ISRO), Ahmedabad, Gujarat, India

*Email: nimisha@sac.isro.gov.in

(Received: Aug 10, 2021; in final form: Oct 06, 2021)

Abstract: Atmospheric Rivers (ARs) are known to carry huge amount of moisture in a very short interval of time leading to extreme precipitation, which in turn may result in flood like events in some part of the world. They also play an important role in governing the global hydrological cycle by contributing considerable fraction of rainfall. Occurrence of ARs particularly over India and adjoining regions have been studied to some extent but particularly on hydrological extreme event basis. This paper presents novel observations of linking branching of ARs from monsoonal circulation over Indian region leading to flood events in Ganga and Brahmaputra river basins. In this study, identification of ARs was performed by computing Integrated Water Vapour Transport (IVT) from ERA5 ensemble mean dataset that uses specific humidity, zonal and meridional components of wind vectors between 1000 hPa to 300 hPa as initial parameters. The identified AR events were compared with altimeter observed water level over Ganga (25.29° N, 87.12° E; 25.59° N, 81.60° E; 25.51° N, 85.70° E) and Brahmaputra (26.21° N, 91.04° E) virtual gauging sites for the year 2008-2020 depending upon the availability of altimeter time series. Increase in water level was observed within 5-14 days of AR events in Ganga river but had minimal effect over Brahmaputra virtual gauging site. Flux computed for these ARs like phenomenon were correlated with altimeter observed water level which resulted in $r=0.47$ at Ganga near Prayagraj (25.59° N, 81.60° E). These observations indicate that the rate of recurrence and the amount of the water flux carried by the ARs leads to increased runoff that subsequently increases river flow.

Keywords: Atmospheric Rivers, Integrated Water Vapour Transport (IVT), Altimeter, Water Level, Specific Humidity, Monsoon.

1. Introduction

Atmospheric Rivers (ARs) are described as long and narrow filamentary structures that are responsible for water vapour transport across the mid-latitudes (Shields and Kiehl, 2016). They bear a resemblance with the terrestrial rivers that flow in a channel and are restricted by banks on its either side; ARs are concentrated bands of water vapour carrying huge moisture towards the poles (Mc Gregor, 2019). ARs account for over 90% of moisture transport toward the poles and take up only 10% of Earth's circumference (Zhu and Newell, 1998). At any given point in time, there are 3 to 5 ARs active around any given hemisphere (Zhu and Newell, 1998; Gimeno et al., 2014).

ARs are capable of carrying large amounts of water from one place to another through narrow corridors in the atmosphere and when they deposit their moisture in form of very heavy rainfall, it can lead to floods (Konrad and Dettinger, 2017; Lamjiri et al., 2017; Lavers et al., 2011; Lavers and Villarini, 2013; Paltan et al., 2017; Ralph et al., 2006). ARs over Pacific Ocean that carry moisture all the way from Hawaii and deposit it over California (Guan et al., 2010), commonly known as the Pineapple Express (Lackmann and Gyakum, 1999), have been studied in great detail. In India, ARs have been linked to the extremely heavy precipitation over the West Coast during monsoon (Dhana Lakshmi and Chakraborty, 2021) and the Chennai floods of December 2015 (Dhana Lakshmi and Satyanarayana, 2019).

Different researchers have used different thresholds and variables to identify land falling AR. ARs are usually longer than 2000 km and less than 1000 km wide (Ralph et al., 2004; Guan and Waliser, 2015). Two most common variables used to detect ARs are IWV (Integrated Water

Vapour) and IVT (Integrated Vapour Transport). IWV considers the column-integrated water vapour from satellite (Ralph et al., 2004) or atmospheric models (Dettinger et al., 2011) whereas IVT uses specific humidity and wind velocity components to compute vertically integrated horizontal water vapour transport between 1000-300 hPa levels from atmospheric reanalysis data (Zhu and Newell, 1998). IVT is recognized to better capture ARs in the atmosphere (Rutz et al., 2014; Lavers and Villarini, 2013; Nayak et al., 2016). It has been observed that there are more ARs in the winter half of a year due to the association of ARs with extra-tropical cyclones (Gimeno et al., 2014).

In India, some researchers have reported monsoon time AR leading to extreme rainfall in the west coast of India (Dhana Lakshmi and Satyanarayan, 2019, 2020; Dhana Lakshmi et al., 2019). Yang et al. (2018) reported the climatology of AR over Bay of Bengal and showed the linkage to northern Indian extreme rainfall. This shows that although less common, ARs during monsoon are possible and can be crucial in understanding certain extreme events and their association with floods.

Ganga and Brahmaputra river basins in India witness widespread floods during the monsoon season and the frequency of floods in Indian sub-continent have increased in the past decade under a warming climate (Ali et al., 2019). Large-scale global phenomena such as El Nino, Indian Ocean Dipole etc. have been linked to floods and droughts in India. However, effects of ARs in monsoonal extreme events have been studied on a case-to-case basis only (Dhana Lakshmi and Chakraborty, 2021). In this paper, we present new observations linking the branching of ARs from monsoonal circulation to flood events in the Indian Ganga and Brahmaputra River Basin. We show that

the frequency and amount of vapour carried by these branches have a direct impact on the river water levels and associated flood events.

2. Study area and data used

Ganga and Brahmaputra are one of the largest river basins of Asia circumscribing countries of the South Asian region including India, China, Nepal and Bangladesh. They are known to support a variety of flora and fauna, also keep up the livelihood of people by supplying fertile agricultural lands, providing drinking water and also in assisting hydropower activities (Rasul, 2015). Dhar and Nandargi, 2000 also tried to summarize the potentialities of both the rivers and concluded that Ganga is known to have greater potential in agricultural irrigation while Brahmaputra is having high hydropower potential. One major characteristic of these two basins is that they particularly lie in the monsoonal strap because of which their water level fluctuates to a large extent. Several regions of these two river basins are also susceptible to flood like conditions due to extreme rainfall taking place during the monsoon period that typically lies between June to September. Chowdhury and Ward, 2004 observed that most extreme floods in Ganga were observed during September month because increase in river water level was found to be maximal. Brahmaputra basin signalizes two spells of flood, one in July and August and other in September (Chowdhury and Sato, 1996). Present study was carried out over Ganga and Brahmaputra river basins along with Bay of Bengal.

The variables used in the study include specific humidity and zonal (U) and meridional (V) component of wind vector at different pressure level between 1000 hPa to 300 hPa for the month of July and August (2001-2020). They were obtained from ERA5 (European Centre for Medium-Range Weather Forecasts Reanalysis 5th Generation) ensemble mean dataset for 1200 UTC having $0.5^\circ \times 0.5^\circ$ spatial resolution (C3S, 2017). ERA5 is the reanalysis climate data produced by ECMWF providing hourly data from 1979 to present at 37 pressure levels. Water level of altimeter gauging sites in Ganga (25.29° N, 87.12° E; 25.59° N, 81.60° E; 25.51° N, 85.70° E) and other in Brahmaputra (26.21° N, 91.04° E) were acquired from THEIA Land Data Centre (Santos da Silva et al., 2010; Normandin et al., 2018; <http://hydroweb.theia-land.fr/>). This uses Ku-band satellite altimetry (Jason-2/3) to estimate water level. It provides water level at nearly about 250 virtual stations across the globe and has a revisit time of approximately 10 days at our gauging sites.

3. Methodology

In order to detect ARs, one of the most common parameter is to compute Integrated Water Vapour Transport (IVT, Zhu & Newell, 1998). In this study, AR identification was done by calculating IVT for the month of July and August (2001-20) from ERA5 ensemble mean data. IVT is calculated as:

$$IVT = \sqrt{\left(\frac{-1}{g} \int_{1000}^{300} qu dp\right)^2 + \left(\frac{-1}{g} \int_{1000}^{300} qv dp\right)^2} \quad (1)$$

Here, g is the acceleration of gravity ($m s^{-2}$), q is specific humidity ($kg kg^{-1}$), u and v are the zonal and meridional components of wind vector ($m s^{-1}$) and p is the air pressure (Pa).

IVT intensity threshold was chosen to be $250 kg m^{-1} s^{-1}$ (Rutz et al., 2014; 2015; Ralph et al., 2017). ARs that passed through India in the month of July and August were identified by applying the threshold criteria of $IVT > 250 kg m^{-1} s^{-1}$ and length to width ratio greater than 2:1. Frequency of ARs in July and August was also recorded for the year 2001-20. Subsequently, altimeter observed water level for Ganga (25.29° N, 87.12° E; 25.59° N, 81.60° E; 25.51° N, 85.70° E) and Brahmaputra (26.21° N, 91.04° E) was analysed within 5-14 days of AR events in Ganga and Brahmaputra river basins for the period 2008-2020 depending upon the availability of altimeter data. Flux was also computed for these AR like phenomena and was related with altimeter observed water level for the above locations. Figure 1 shows flowchart of the algorithm adopted in the study.

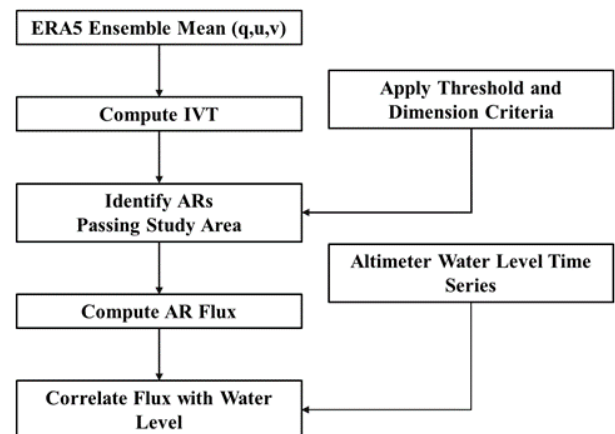


Figure 1. Flowchart of the algorithm adopted in the study.

4. Results and discussion

4.1 Identification and analysis of AR events

ARs satisfying IVT threshold and dimension criteria were identified over the Indian region and adjoining seas for the month of July and August (2001-20) by computing IVT using ERA5 ensemble mean dataset for 1200 UTC. Figure 2 shows IVT and wind vectors during two detected AR events of (a) 13 August 2011 and (c) 16 July 2018 along with zoomed in extent of IVT over India and adjoining regions (b) 13 August 2011 and (d) 16 July 2018. High moisture flux carried by these ARs, that form a part of the monsoon circulation, is clearly distinguished. We observed splitting of these ARs from the monsoonal circulation which extends from Arabian Sea to the western Pacific ocean. After splitting from the monsoonal circulation near northern Bay of Bengal, these ARs turn towards the Ganga and Brahmaputra basins and can extend up to Northwest India (Figure 2b and 2d).

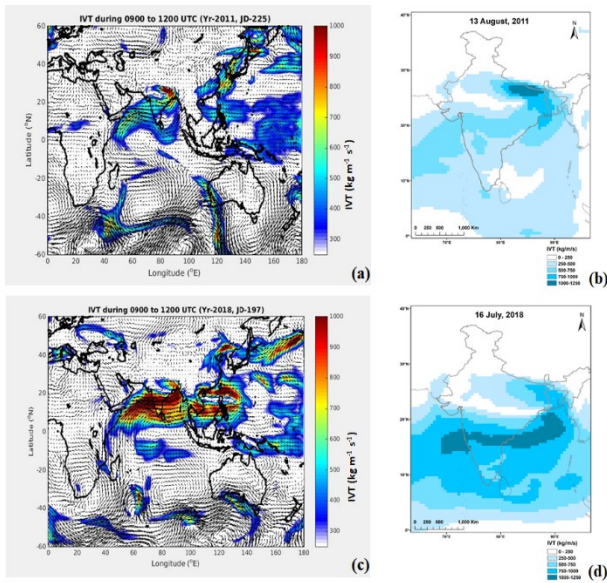


Figure 2. IVT maps with intensity (colour shading) and wind vectors on (a) 13 August 2011 (c) 16 July 2018 for 1200 UTC. Zoomed in spatial extent of IVT over India and adjoining regions on (b) 13 August 2011 (d) 16 July 2018.

AR events, similar to the ones shown in Figure 2, were observed in July and August months of every year between 2001-2020. The centreline of all these ARs, beginning from the point where they split from monsoon circulation, is presented in Figure 3 for every 5-year period (2001-05; 2006-10; 2011-15 and 2016-20). The actual length of these ARs is different, as they originate from the large-scale moisture transport during monsoon, but for the purpose of this study, the origin is taken from the point where they bend and curve towards the Indo-Gangetic plains. It can be clearly seen that the centreline of AR bends towards the Ganga catchment shifting moisture convergence away from the Brahmaputra river basin. On analysing the spatial extent of these centrelines, we observe that all of them are concentrated over the Northern belt of India with a smaller extent over Northeast India.

Figure 4 shows the frequency of ARs observed over the study region for Jul-Aug of 2001-2020, showing highest occurrence of ARs in the year 2003 with 4 events in the two months. Although the occurrence of these ARs varies between 1-4 per year during Jul-Aug, it is interesting to note their timing with respect to flood events in the Ganga and Brahmaputra basins. The influence of these ARs in causing floods can be studied by relating their spatial and temporal occurrence with the flood events in Ganga and Brahmaputra rivers. Instead of analysing the spatial extent of flood in these basins, in this study we use water level along different locations of the rivers as an indicator of flood.

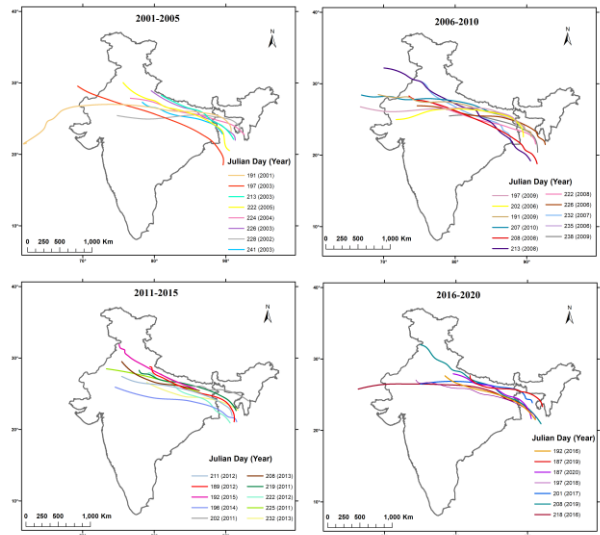


Figure 3. Identification of Atmospheric Rivers (ARs) that passed through India for every five year period (2001-20) of July & August.

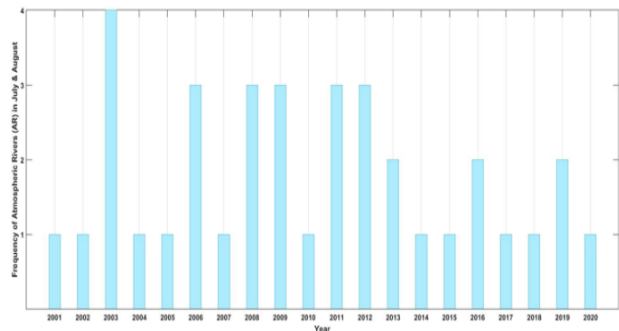


Figure 4. Frequency of ARs in July and August for the year 2001-20.

4.2 Linking AR to flood events

ARs with high IVT have the potential to cause more rainfall and this may lead to increased runoff in the subsequent days. This increased runoff increases the water level in rivers, which can be picked up by altimeters. Figure 5 shows the plot of altimeter observed water level time series for three gauging locations in Ganga (25.29° N, 87.12° E; 25.59° N, 81.60° E; 25.51° N, 85.70° E) and one in Brahmaputra (26.21° N, 91.04° E) along with the days when ARs were observed at their peak lengths. The timing of ARs matches well with high-flow conditions in these gauging locations of Ganga but has minimal effect over Brahmaputra virtual gauging site. During such AR phenomenon, it was observed that the moisture transport tends to shift away from the Brahmaputra basin towards Ganga basin. This results in more precipitation in the Ganga catchment and subsequent increase in river flow. However, the strength of an AR in terms of flux of moisture carried by them usually determines the intensity of rain and subsequent flooding.

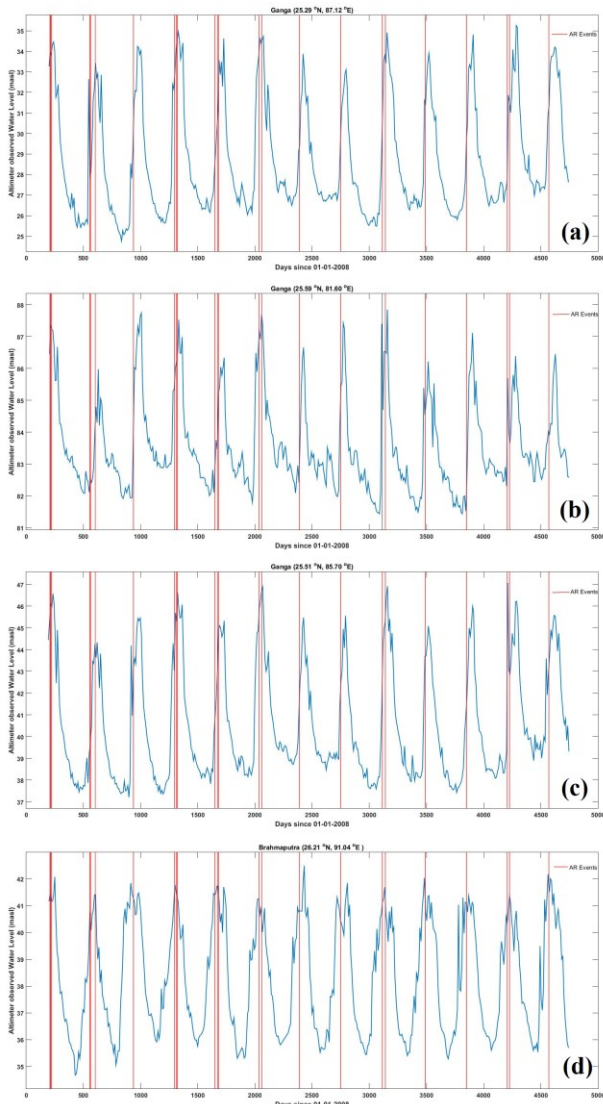


Figure 5. Plots of altimeter observed water level at four gauging locations (a) 25.29° N, 87.12° E; (b) 25.59° N, 81.60° E; (c) 25.51° N, 85.70° E and (d) 26.21° N, 91.04° E with the days of ARs events.

Flux of an AR (represented in kg s^{-1}) is similar to the discharge carried by a river. Flux was computed for each event at the cross-section where maximum IVT value is observed along the length of the AR. This flux was correlated to the river water level observed by altimeter in the subsequent 5-14 days of the event. This gap between AR flux and altimeter observation is taken to account for the lag between ARs moisture being converted to rain and subsequent runoff reaching the river. Figure 6 shows the scatter plot and correlation between AR flux and altimeter observed water level for a gauging site (25.59° N, 81.60° E) in Ganga. Although the correlation coefficient value ($r=0.47$) is low, we observe a significant direct positive correlation between the two variables. This indicates that the moisture carried by ARs detected in this study has a direct impact on the river water level and thus plays a major role in influencing flood events. This non-periodic splitting of ARs from monsoonal flow and the amount of moisture carried by them during July-August influences the timing of flood events in Ganga river basin. More study is required to quantitatively estimate the impact of these

ARs in causing heavy precipitation and flood events in Ganga basin. Identification and prediction of these branching ARs can help improve weather forecasts and flood early warning systems in the region.

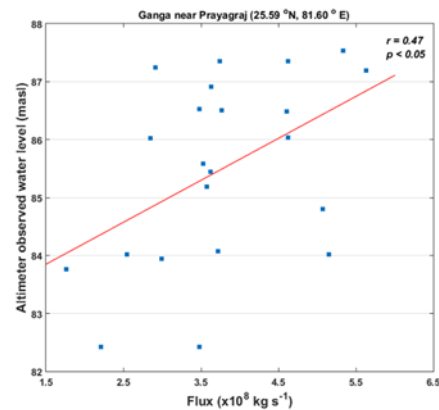


Figure 6. Scatter plot between altimeter observed water level vs Flux for the year 2008-2020.

5. Conclusions

Present study discusses about branching of ARs from the monsoonal wind over Indian Ganga and Brahmaputra river basins. AR identification was performed by computing IVT using ERA5 ensemble mean datasets of July and August for the period 2001-20. These ARs originate from the monsoon circulation near Bay of Bengal and turn towards Ganga and Brahmaputra basins, extending all the way up to Northwest India. Timing of AR events matched well with increasing water level along Ganga River, which was used as an indicator of flood, however, minimal effect was observed over the Brahmaputra river basin. Flux of ARs computed at the cross section with maximum IVT showed correlation 0.47 ($p < 0.05$) with altimeter observed water level at one of the gauging location of Ganga (25.59° N, 81.60° E). This study showed that splitting of ARs from the monsoon circulation can have impact on flood events in Ganga river basin.

Acknowledgements

This work was carried out under SARITA program of Land Hydrology Division, EPSA, SAC. The authors are thankful to Shri N M Desai, Director, SAC and Dr. I M Bahuguna, Deputy Director, EPSA. The authors thankfully acknowledge ECMWF for ERA5 Reanalysis data and THEIA Land Data Centre/ CNES for altimeter water level.

References

Ali H., P. Modi and V. Mishra (2019). Increased flood risk in Indian sub-continent under the warming climate, *Weather and Climate Extremes*, 25, 100212. <https://doi.org/10.1016/j.wace.2019.100212>.
 Chowdhury M. R. and N. Ward (2004). Hydro-Meteorological Variability In The Greater Ganges–Brahmaputra–Meghna Basins, *International Journal of Climatology*, 24, 1495-1508.

- Chowdhury M. R. and Y. Sato (1996). Flood monitoring in Bangladesh: experience from normal and catastrophic floods. *Hydrology (Journal of the Japanese Association of Hydrological Sciences)*, 26, 241–152.
- Copernicus Climate Change Service (C3S) (2017): ERA5: Fifth generation of ECMWF atmospheric reanalyses of the global climate. Copernicus Climate Change Service Climate Data Store (CDS), 22 February, 2021. <https://cds.climate.copernicus.eu/cdsapp#!home>.
- Dettinger M. D., F. M. Ralph, T Das, P. J. Neiman and D. R. Cayan (2011). Atmospheric Rivers, Floods and the Water Resources of California. *Water*, 3(2):445-478.
- Dhana Lakshmi D. and A. N. V. Satyanarayana (2019) Influence of atmospheric rivers in the occurrence of devastating flood associated with extreme precipitation events over Chennai using different reanalysis data sets. *Atmospheric Research*, 215, 12-36. <http://doi.org/10.1016/j.atmosres.2018.08.016>.
- Dhana Lakshmi D. and A. Chakraborty, (2021). Assessment of WRF-ARW model parameterization schemes for extreme heavy precipitation events associated with atmospheric rivers over West Coast of India, *Atmospheric Research*, 249, 105330. <https://doi.org/10.1016/j.atmosres.2020.105330>.
- Dhana Laskhmi D. and A. N. V. Satyanarayana (2020). Climatology of landfalling atmospheric Rivers and associated heavy precipitation over the Indian coastal regions. *International Journal of Climatology*, 1–18.
- Dhana Laskhmi D., A. N. V. Satyanarayana and A. Chakraborty (2019). Assessment of heavy precipitation events associated with floods due to strong moisture transport during summer monsoon over India. *Journal of Atmospheric and Solar-Terrestrial Physics*, 189, 123-140.
- Dhar O. and S. Nandargi (2000). A study of floods in the Brahmaputra basin in India. *International Journal of Climatology - INT J CLIMATOL*. 20. 771-781.
- Gimeno L., R. Nieto, M. Vázquez and D. A. Lavers (2014). Atmospheric rivers: A mini-review, *Frontiers in Earth Science*, 2(1), 1-6, doi:10.339/FEART.2014.00002.
- Guan B. and D. E. Waliser (2015). Detection of atmospheric rivers: Evaluation and application of an algorithm for global studies. *Journal of Geophysical Research: Atmospheres*, 120, 12, 514–12, 535. <https://doi.org/10.1002/2015JD024257>.
- Guan B., N. P. Molotch, D. E. Waliser, E. J. Fetzer and P. J. Neiman (2010), Extreme snowfall events linked to atmospheric rivers and surface air temperature via satellite measurements, *Geophysical Research Letters*, 37, L20401, doi:10.1029/2010GL044696
- Konrad C. P. and M. D. Dettinger (2017). Flood runoff in relation to water vapour transport by atmospheric rivers over the western United States, 1949–2015. *Geophysical Research Letters*, 44, 11456-11462, <https://doi.org/10.1002/2017GL075399>.
- Lackmann G. M. and J. R. Gyakum (1999). Heavy cold-season precipitation in the northwestern United States: synoptic climatology and an analysis of the flood of 17–18 January 1986. *Weather and Forecasting*, 14, 687–700.
- Lamjiri M. A., M. D. Dettinger, F. M. Ralph, and B. Guan, (2017). Hourly storm characteristics along the U.S. West Coast: Role of atmospheric rivers in extreme precipitation, *Geophysical Research Letters*, 44, 7020-7028. <https://doi.org/10.1002/2017GL074193>.
- Lavers D. A. and G. Villarini (2013). The nexus between atmospheric rivers and extreme precipitation across Europe. *Geophysical Research Letters*, 40, 3259–3264. <https://doi.org/10.1002/grl.50636>.
- Lavers D. A., R. P. Allan, E. F. Wood, G. Villarini, D. J. Brayshaw and A. J. Wade (2011). Winter floods in Britain are connected to atmospheric rivers. *Geophysical Research Letters*, 38: L23803.
- McGregor G. R. (2019). Climate and rivers. *River Research and Applications*, 35, 1119– 1140. <https://doi.org/10.1002/rra.3508>.
- Nayak M. A., G. Villarini and A. A. Bradley (2016). Atmospheric rivers and rainfall during NASA's Iowa Flood Studies (IFloodS) campaign. *Journal of Hydrometeorology*, 17(1), 257–271. <https://doi.org/10.1175/JHM-D-14-0185.1>.
- Normandin C., F. Frappart, A. T. Diepkilé, V. Marieu, E. Mougin, F. Blarel, B. Lubac, N. Braquet, A. Ba (2018). Evolution of the Performances of Radar Altimetry Missions from ERS-2 to Sentinel-3A over the Inner Niger Delta. *Remote Sensing*, 10(6), 833, doi: 10.3390/rs10060833.
- Paltan H., D. Waliser, W. H. Lim, B. Guan, D. Yamazaki, R. Pant and S. Dadson (2017). Global floods and water availability driven by atmospheric rivers. *Geophysical Research Letters*, 44, 10,387–310,395. <https://doi.org/10.1002/2017GL074882>.
- Ralph F. M., P. J. Neiman and G. A. Wick (2004). Satellite and CALJET aircraft observations of atmospheric rivers over the eastern North-Pacific Ocean during the winter of 1997/98, *Monthly Weather Review*, 132, 1721 – 1745.
- Ralph F. M., P. J. Neiman, G. Wick, S. Gutman, M. Dettinger, D. Cayan and A. B. White (2006). Flooding on California's Russian River: Role of atmospheric rivers. *Geophysical Research Letters*, 33, L13801. <https://doi.org/10.1029/2006GL026689>.
- Ralph F. M., S. F. Iacobellis, P. J. Neiman, J. M. Cordeira, J. R. Spackman, D. E. Waliser, G. A. Wick, A. B. White and C. Fairall, (2017). Drosoponde observations of total

integrated water vapor transport within North Pacific atmospheric rivers. *Journal of Hydrometeorology*, 18(9), 2577–2596. <https://doi.org/10.1175/JHM-D-17-0036.1>.

Rasul G. (2015). Water for growth and development in the Ganges, Brahmaputra, and Meghna basins: an economic perspective. *International Journal of River Basin Management*, 13(3), 387-400. <https://doi.org/10.1080/15715124.2015.1012518>.

Rutz J. J., W. J. Steenburgh and F. M. Ralph (2014). Climatological characteristics of atmospheric rivers and their inland penetration over the Western United States. *Monthly Weather Review*, 142(2), 905–921. <https://doi.org/10.1175/MWR-D-13-00168.1>.

Rutz J. J., W. J. Steenburgh and F. M. Ralph (2015). The inland penetration of atmospheric rivers over western North America: a Lagrangian analysis. *Monthly Weather Review*, 143(5), 1924–1944. <https://doi.org/10.1175/MWR-D-14-00288.1>.

Santos da Silva J., S. Calmant, O. Rotuono Filho, F. Seyler, G. Cochonneau, E. Roux and J. W. Mansour (2010). Water Levels in the Amazon basin derived from the ERS-2 and ENVISAT Radar Altimetry Missions. *Remote Sensing of the Environment*, doi:10.1016/j.rse.2010.04.020.

Shields C. A. and J. T. Kiehl (2016). Atmospheric river landfall-latitude changes in future climate simulations, *Geophysical Research Letters*, 43, 8775–8782, doi:10.1002/2016GL070470.

Yang Y., Z. Tongtiegang, N. Guangheng and S. Ting (2018). Atmospheric rivers over the Bay of Bengal lead to northern Indian extreme rainfall, *International Journal of Climatology*, 38, 1010-1021.

Zhu Y. and R. E. Newell (1998). A proposed algorithm for moisture fluxes from atmospheric rivers. *Monthly Weather Review*, 126(3), 725–735.

An Approach of Satellite and UAS based Mosaicked DEM for Hydrodynamic Modelling – A Case of Flood Assessment of Dhanera City, Gujarat, India.

Kishanlal Darji¹, Dhruvesh P. Patel^{1*}, Amit Kumar Dubey², Praveen K. Gupta² and R P Singh²

¹Department of Civil Engineering, School of Technology, PDEU, Gandhinagar, Gujarat, India

²Space Applications Centre, ISRO, Ahmedabad

*Correspondence: dhruvesh.patel@sot.pdpu.ac.in

(Received: Aug 15, 2021; in final form: Oct 06, 2021)

Abstract: Digital Elevation Models (DEMs) are an essential source of information, which describe the terrain that allows researchers to estimate various hydrological processes. Flood modelling is an important hydrological process which is applicable to estimate and assess the flood risk in susceptible area, however the accuracy of flood estimation depends on DEM resolution, therefore, the present case describes the generation of mosaicked high-resolution DEM for urban and riverine flood inundation modelling. First stage, satellite based CARTOSAT DEM of 10m x 10m of Rel river catchment is prepared for riverine flooding, whereas in second stage, UAS (Unmanned Aerial System) based 3.6 cm x 3.6 cm high resolution DEM is generated for Dhanera city using UAS (Phantom 4 Pro RTK UAV and Pix4D software). This paper focuses on merging DEM methods where generated high resolution UAS based DEM is mosaicked with CARTOSAT DEM using three methods based on software like Inverse Distance Weighted Interpolation method (IDW method) using Global Mapper software, Nearest Neighbour using ArcGIS software and Stitching method using HEC-RAS software. Out of all the methods, HEC-RAS based merging method is found to be more promising without leading a discontinuity on the edge of DEM. Present flood assessment case of Dhanera and Rel river basin shows the merged DEM can be used as cost-effective approach for accurate flood estimation of flash flooding in an urban and riverine region.

Key Words: DEM, Flood Assessment, UAV, Drone, CARTOSAT, Rel River

1. Introduction

Floods are most frequent and natural disasters worldwide which cause the major economic damage at the global level (Memon et al., 2020; Nagesh Kumar et al., 2020; Popescu et al., 2017). Floods have been recurrent phenomena in India. Almost every year floods of varying magnitude affect some part of the country or the other, which cause huge loss of lives and damage to livelihood systems, property, infrastructure and public utilities (NDMG, 2008; NDMP, 2019). Gujarat 2017, Kerala-2018, and Bihar 2019 are some of recent examples of flooding in India (Gupta, 2020). Floods are not fully preventable, but the associated hazards could be minimized if flood-prone areas are known in advance (Patel et al., 2017; Sahoo and Sreeja, 2017). Therefore, flood assessment has become an important step to reduce the loss of life and properties in floodplains area (Patel et al., 2017). Many hydrologic and hydrodynamic models are widely available for flood assessment and flood prediction; however, modelling techniques are mostly based on the Digital Elevation Model (DEM), and thus the reliability and accuracy of flood simulations results such as inundation, extent, flow velocity, flow depth, flow patterns, are highly dependent on the accuracy and resolution of the DEM data (Agnihotri et al., 2021; Jakovljevic et al., 2019; Saksena and Merwade, 2015). DEMs contain the elevation of a point on a surface above the mean sea level. DEMs are sometimes referred to as Digital Terrain Model (DTM), or Digital Surface Model (DSM) (Ajayi et al., 2017; Poon et al., 2005). Nowadays, many open source satellite based DEM i.e ASTER global, SRTM (30 m x 30 m), GMTED2010 (30 arc-second), GMTED 2010 (15 arc-seconds) GMTED 2010 (7.5 arc-seconds) and (ALOS (12.5 m x 12.5 m), are available for flood assessment studies, however low resolution DEM

(generally coarser than 30m) has many vertical inaccuracies and these DEMs are too old to break the accuracy of estimation of flood hazard in urban area (Lakshmi and Yarrakula, 2018). The restricted accessibility to get high-accuracy DEMs states that open-access global DEMs are still used widely in assessment of flood models, mostly in data scarce region (Case presented by (Glas et al., 2020; Pandya et al., 2021; Patel and Pandya, 2021). It has been discovered that high-resolution DEMs like LIDAR, INSAR, UAV based DEM, ground surveying-based DEM, etc. give better flood estimations, and thus can be considered a necessary parameter for any flood modelling (Casado et al., 2018; Pandey et al., 2014; Şerban et al., 2016; Prieto et al., 2020; Pathan et al., 2021). Number of case studies shows that current remote sensing approaches fail to provide sufficient detail to assess the effects of micro-topography and the presence of property flood resistance measures (Casado et al., 2018; Ogunbadewa, 2012; Patel and Srivastava, 2014; Vant-Hull et al., 2007). Under this circumstances, Unmanned Aerial Vehicles (UAVs) or Unmanned Aerial System (UASs) are emerging platform for remote mapping at very high spatial resolution for 3D surveying, archaeological documentation, earth observation and monitoring, 3D city modelling, precision farming, hazard monitoring, environmental monitoring and assessment. Many case presented by (Casado et al., 2018; Govedarica et al., 2018; Kim and Davidson, 2015; Schumann et al., 2019) and suggested that UAV-generated very high-resolution DEM can be used for examining the stream characteristics, stream velocity and floodplain, thereby not only looking and augmenting our scientific understanding of hydrological processes at the (very) small scale, but improve the understanding in particular of flood processes (Ahmad, 2011). Examined the proficiency of UAV in creating digital maps using a light weight fixed wing UAV

equipped with a high-resolution digital camera where the conclusion shows a sub-metre accuracy (Leitão et al., 2016 and Tokarczyk et al., 2015). Demonstrated the applicability and the advantages of using UAVs to generate very high resolution DEMs for urban overland flow and flood modelling. Emergency responders have used Unmanned Aircraft Systems (UAS) to acquire core information pre-, during- and post- flood events. High resolution DEM is cost worthy and expensive for flood assessment, especially the area consist with agriculture and forest area. Although it is the important parameter to estimate the sub metric accuracy for flood inundation in river bank inundated urban area. Only a few data can be accessed freely, for example, the DEM data with high resolution may not accessible for everyone and also the data is restricted. On the contrary, the level precise topographic data as an input data for terrain models is a key element of the accuracy of hydraulic flood modelling (Sahid et al., 2018). Consequently, many researchers have developed DEM as an alternative data to obtain reliable flood modelling (Patel et al., 2020). Mosaicking or interpolating DEM is found helpful where the UAV survey is not possible for the entire catchment or where there is scarcity of high-resolution DEM data. Several approaches to ensure smooth transition of DEMs have been proposed (Petrasova et al., 2017; Reuter et al., 2007; Robinson et al., 2014) in the context of global DEM mosaicking and DEM void filling. To ensure seamless transition between DEMs (Robinson et al., 2014), proposed blending DEMs using weighted averaging method where weight is a function of distance to transition line between two DEMs². Petrasova et al. (2017) presented the case of fusion of LiDAR and UAS based DEMs, and LiDAR and Kinect based DEMs for water flow modelling using GRASS GIS and distance based weighted average method and concluded that the demonstrated technique becomes highly relevant for researchers and practitioners working for high-resolution DEMs mosaicking.

A novel approach has been performed in this paper for Dhanera and Rel River catchment for flood assessment of 2017 to produce the cost efficient UAS based DEM for Dhanera city and obtain a better mosaicked DEM by combining CARTOSAT (10m resolution) and UAS DEM

(3.6cm resolution) which can be used for flow simulation in hydrodynamic modelling. CARTOSAT images has been utilized for satellite based DEMs for Rel river catchment, whereas UAS (Phantom 4 Pro RTK UAV and Pix4D software) based 3.6 cm x 3.6 cm high resolution DEM has been considered for Dhanera city. The seamless flow approach has been compared for different mosaicked DEM and identified the best mosaic methods which provide the fast and seamless flow for hydrodynamic modelling. It reduces the requirement of High resolution DEM of entire basin for decision making activities, and provides the cost effective accurate flood assessment approach for riverine urban flooding in developing countries. Paper reports a case study for fusion of DEM using different software techniques and reduce DEM fusion inaccuracy in flood assessment techniques.

2. Study area

The study is demonstrated on Rel river Basin, which is situated in Banaskantha district, Gujarat, India (Figure.1). The Rel-river is originated from the Southern part of the Sundhamata Mountain and meet to the Rann of Kachchh in Gujarat. It has two courses.

The first course flows from the Sundhamata Mountain to Pachala Dam, Jetpura Dam reaching to Bapla and Runi, while the other course mingles in the Kes Pond. Its catchment covers an area of 442 km², lies between 240 50'N to 240 75' N latitude and 720 00'E to 720 45' E longitude. The lowest point is near Dhanera taluka and Dhanera city and it is located near the mouth of the Rel River. The Rel-river is an ungauged river with the data-scarce region. The width of the river is about 280 m and 180 m at the location of the Road Bridge and Railway Bridge, respectively. The riverbed slope is about 1 in 500 from U/S of the railway bridge and up to D/S of cause way location. Rel river is having very steep topography in the upper catchment, resulted the flash flood in the D/S region. Catastrophic flood of the maginitue of 273 m³/s and 3355 m³/s has been observed in the recent year of 2015 and 2017.

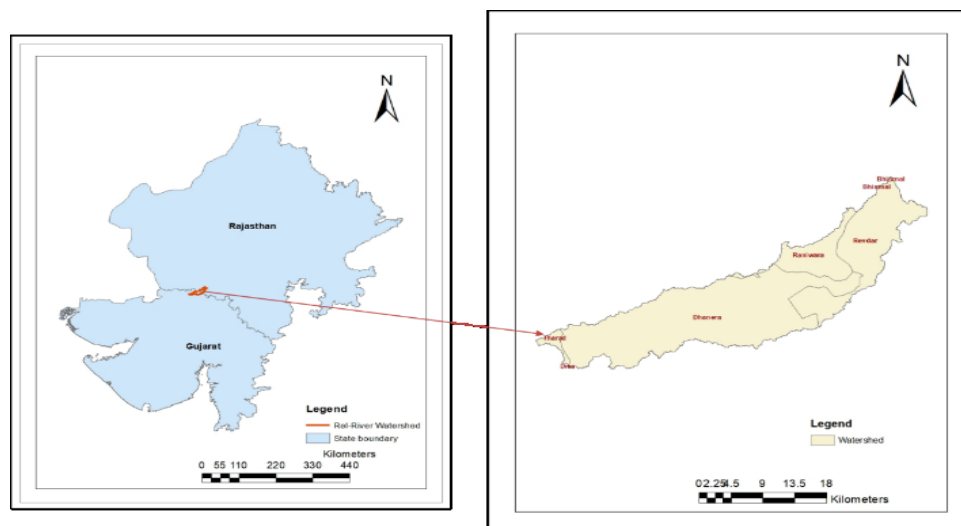


Figure 1. Study area showing Rel river catchment

3. Materials and methods

Method adopted for this research is presented in Figure 2, it has performed in basic 2 different approaches 1) DEM preparation 2) DEM mosaicking. In the first stage, two DEM were prepared. One is high resolution DEM using UAS techniques for Dhanera City, whereas second DEM is for Rel river basin, obtained from satellite based CARTOSAT DEM data. UAS techniques include collecting UAV aerial data and introducing the structure from algorithm to generate point cloud, DSMs and DEMs. Second stage deals with DEM mosaicking techniques for DEM fusion between CARTOSAT DEM and UAS based DEM. In this stage UAV based DEM for Dhanera city is merged with Rel river watershed CARTOSAT DEM using following methods. i) Inverse Distance Method (using Global Mapper) ii) Nearest Neighbour (ArcGIS software) iii) Stitching Method (HEC-RAS software). Flood modelling is performed using the merged DEM as input in HEC-RAS software and comparison is made on the basis of area and depth parameters. The output is generated in form of inundation map, depth profile and maximum depth from HEC-RAS modelling and is compared with the open Source data to check the boundary errors at merging areas. At last, errors corresponding to coarser resolution and vertical accuracy into the resampled DEMs are removed for smooth blending of DEMs.

3.1. Cartosat DEM

The CARTOSAT-1 Digital Elevation Model (CARTODEM) is a National DEM developed by the Indian Space Research Organization (ISRO). The spatial resolution is 10 m in the horizontal plane (Figure 3). Each camera has a pixel size 7 x 7 micron, swath of about 29.42 km, focal length 1945 mm (Rawat et al., 2013).

3.2 UAS DEM

Present study described the use of UAS system for post flood assessment for generating high resolution DEM for Dhanera city. DEM extraction using a UAS is performed in two stage process. Light weight UAV i.e. DJI Phantom 4 Pro RTK with automated flight operation was used for the acquisition of the image data at an altitude of 130 m above the ground level of the image area with 80% overlapping. All images obtained were from a digital, 4K resolution camera (FC300X), affixed to the lower part of the UAV system. The UAV was equipped with 12 mega pixel, focal length of 2.8 mm, and 4K resolution DJI camera. The camera has RGB band and operates in both manual and auto mode (For this study, it was operated manually). After that at second stage, image processing has been performed invoicing initial processing, point cloud & Mesh generation, DSM, orthomosaic and Index. These procedures were performed using the PiX4D mapper software.

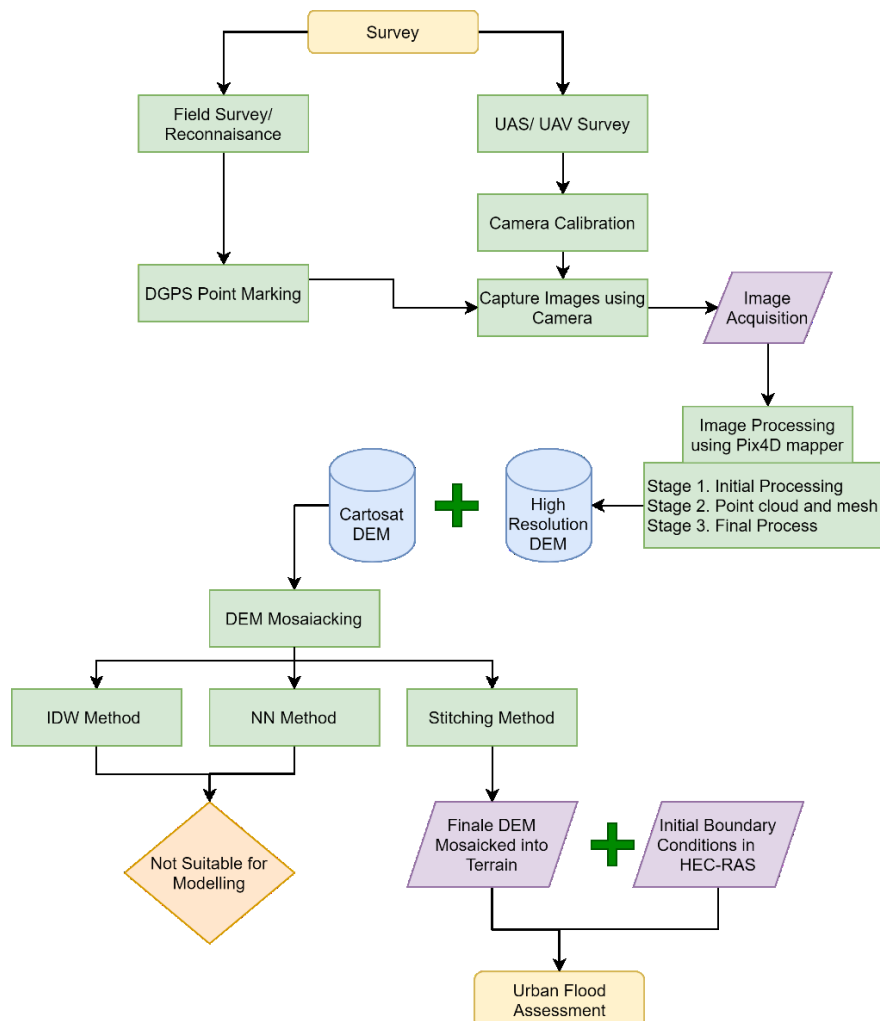


Figure 2. Methodology Chart

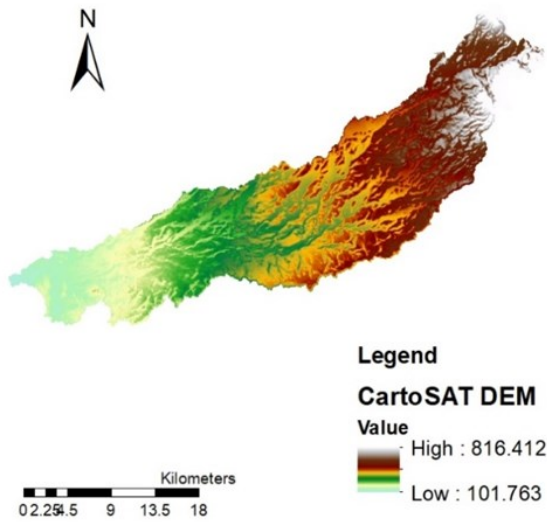


Figure 3. CARTOSAT DEM

3.2.1 Ground Control Point (GCP) Layout

Phantom 4 RTK requires minimal GCP to create accurate map. For the current study area, 7 GCP points were marked. The GCP points are marked with DGPS-RTK. GCP is obtained by continuously operating reference station method of georeferencing the data.

3.2.2 Image Acquisition

Phantom 4 Professional RTK UAV is used for capturing the images over the Dhanera city. The UAV consistent with camera version of and having the image width of 5472px, image height of 3648px, sensor width of 13.2 mm, sensor height of 8 mm, and focal length = 8.8 mm. The KML file for the region is generated (Figure 4). It is divided in to 4 zones and flight plan is decided. The 7 GCP points are marked in the study region (Figure.5). The Aerial images are taken with 80% overlap between consecutive images. The flight height is selected at 130 m so that GSD (ground sampling distance) can be 3.56 cm/px. The area covered during survey is 10 km². The RTK module can provide positioning accuracy of 1cm+1ppm (horizontal), 1.5cm+1ppm (vertical). Total 9222 images are collected for the region.

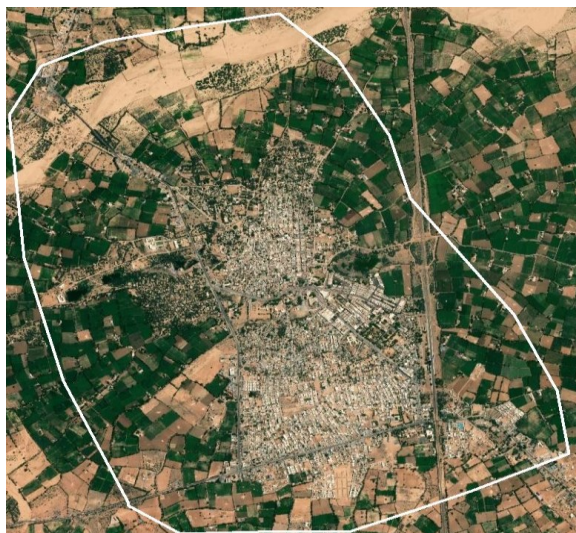


Figure 4. KML file of study area

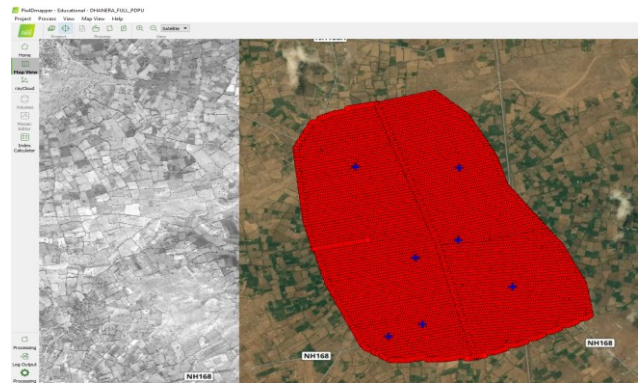


Figure 5. Images with GCP Points at Dhanera city

3.2.3 Image Processing using Pix4D

In this study, 9222 aerial images were captured using UAV for the study area. PIX4Dmapper software was used for analysis, which transforms images into digital spatial models. PIX4Dmapper graphic user performs analysis in three stages namely: Initial Processing, Point Cloud and Mesh, and Final Processing.

i) Initial Processing

In first stage there is key points extraction which identifies specific features as key points in the images. It involves fully automatic iterative proprietary algorithm for bundle block adjustment and sparse cloud point generation shown in (Figures 6-7).

ii) Point Cloud and Mesh

The second stage point cloud and mesh does the point densification where additional tie points are created based on the Automatic Tie points that results in a densified Point Cloud. (Figures 6-7). It also performs 3D textured mesh wherein a 3D textured mesh can be created based on the densified point cloud.



Figure 6. Sample analysis for Pix4D



Figure 7. Point cloud of the area

iii) DSM, Orthomosaic and Index

The third stage consists of generating Digital Surface Model (DSM) which will enable the computation of Volumes, Ortho mosaics and Reflectance Maps. This stage uses inverse distance weighting algorithm (IDW) interpolation for DSM generation. Total 9222 images of the project were divided into several portion to match the capability of computer and splitted in to 10 parts with around 1000 image in each parts with 20 % overlap. These 10 parts were merged in 3 sections in Pix4D for the final processing. (Figure 7). The MTP (Manual Tie Points) are created on the sub projects with the same location and same name in two adjacent project to merge them in a single project. A minimum three no of MTP are required for merging of the projects. After creation of MTP re-optimization is required to reassess the accuracy of the projects. The three final sections were mosaicked to a single DEM. This Mosaicking also involved Overlapping of some areas. Mosaicking was made using Global Mapper. The process takes about 18 hrs. Final DEM of resolution 3.6cm*3.6cm was obtained at the end for the given area of Dhanera city.

3.3 DEMs Mosaicking

The DEMs are the integral part of Hydrodynamic modelling, however, limited availability of high resolution DEM for entire catchment poses challenge of merging DEMs available from different sources at different scale. In this study 3 different mosaicking methods have been applied for mosaicking a CARTOSAT DEM and UAS based DEM. The best way could be the spatial interpolation technology which calculates the DEM grid cell like 1-D hydraulic modelling. There are three methods namely inverse distance weighed interpolation method, nearest neighbour method and terrain stitching method using HEC-RAS as described below.

3.3.1 Inverse Distance Weighted Interpolation method (IDW method) using Global Mapper

This method is adopted using Global Mapper software. This is a comparatively simple way to get merged the different resolution DEM in single one. The mathematical formula of the fusion is based on the weighted average given as below:

$$H_3 = \frac{w_1H_1 + w_2H_2}{w_1 + w_2} \quad (1)$$

Where, H_1 and H_2 are the height values in first DEM and w_1 and w_2 are the weights of second DEM. The entire process is simulated automatic in computer system.

3.3.2 Nearest Neighbour interpolation using ArcGIS software

This method is adopted using ArcGIS software. Like IDW, this interpolation method is a weighted-average interpolation method. The value of an unknown cell is estimated by inserting and determining the point within a polygon. For each neighbour, the area of the portion of its original polygon that becomes incorporated in the tile of the new point is calculated. This method is most appropriate where sample data points are distributed with uneven density.

3.3.3 Terrain Stitching Method using HEC-RAS

The last method for mosaicking is Terrain Stitching method in HEC-RAS. HEC-RAS is an open and freely available software (URL: <https://www.hec.usace.army.mil/software/hec-ras/download.aspx>) When multiple terrain data layers with different resolutions are used to make a terrain data set, HEC-RAS uses "Stitching" to merge the edges of the terrain data layers. HEC-RAS can input more than one GeoTIFF files and merges them into a terrain. RAS mapper converts the grids into the GeoTIFF file format. This GeoTIFF format supports pyramided and tiled data. Tiled data uses less area of the terrain by removing the 'No Data Values' and the pyramided data can store multiple terrain layers in varying resolution. Thus it is possible to merge two DEM of different resolutions. Apart from this, HEC-RAS also allows gives output file format which has smaller storage space, faster computational speed and dynamic mapping of results. Once the GeoTIFF files are created RAS Mapper also creates a *.hdf a and a *.vrt file. The *.hdf (Hierarchical Data Format) file contains information on how the multiple GeoTIFF files are stitched together. The *.vrt (Virtual Raster Translator) is an XML file that contains information about all the raster files. The user can drag and drop the *.vrt file on the ArcGIS project and can get information about all the raster files that make up the terrain layer.

3.4 Flood Modeling in HEC-RAS

The HEC-RAS 5.0.1 is utilized the 2D Saint Venant equation (GW Brunner, 2014; HEC-RAS, 2016; Quiroga et al., 2016):

$$\frac{\partial \xi}{\partial t} + \frac{\partial p}{\partial x} + \frac{\partial q}{\partial x} = 0 \quad (2)$$

$$\frac{\partial p}{\partial t} + \frac{\partial}{\partial x} \left(\frac{p^2}{h} \right) + \frac{\partial}{\partial y} \left(\frac{pq}{h} \right) = - \frac{n^2 pg \sqrt{p^2 + q^2}}{h^2} - gh \frac{\partial \xi}{\partial x} + pf + \frac{\partial}{\rho \partial x} (h\tau_{xx}) + \frac{\partial}{\rho \partial y} (h\tau_{xy}) \quad (3)$$

$$\frac{\partial q}{\partial t} + \frac{\partial}{\partial y} \left(\frac{q^2}{h} \right) + \frac{\partial}{\partial x} \left(\frac{pq}{h} \right) = - \frac{n^2 qg \sqrt{p^2 + q^2}}{h^2} - gh \frac{\partial \xi}{\partial y} + qf + \frac{\partial}{\rho \partial y} (h\tau_{yy}) + \frac{\partial}{\rho \partial x} (h\tau_{xy}) \quad (4)$$

where h is the water depth (m), p and q are the specific flow in the x and y direction ($m^2 s^{-1}$), ξ is the surface elevation (m), g is the acceleration due to gravity (ms^{-2}), n is the Manning resistance, ρ is the water density ($kg m^{-3}$), τ_{xx} , τ_{yy} and τ_{xy} are the components of the effective shear stress and f is the Coriolis (s^{-1}). (Patel et al., 2017; Quiroga et al., 2016) has presented the case of flood assessment of Bolivian Amazonia and Surat city using HEC-RAS based 2D and 1D/2D coupled hydrodynamic modelling. DEM is a sensitive parameter for 2D modelling in this study. 2D modelling is performed for 4 DEM using HEC-RAS: i) Mosaicked DEM based on IDW method ii) Mosaicked DEM based on NN method iii) Mosaicked DEM based on HEC-RAS iv) CARTOSAT DEM. The results for inundation area and depth are extracted in ARCGIS and maps are produced.

4. Observations and Results

4.1 Point cloud evaluation and high-resolution DEM extraction using UAS

A SfM algorithm is used for restoring camera exposure position and for generation of sparse point cloud and MVS algorithm is used for generation of dense point cloud as per

DSM generation method. For this project it took about 384 hours to process DSM, DTM and orthomosaic from the 9222 UAV images at 80 % overlap. As it was not possible to merge all the UAV images in one go, it was divided in 4 parts to perform the processing. Each parts were then mosaicked in global mapper as a single DEM. Accuracy of final DEM obtained was 3.6 cm as shown in Figures 8-9.

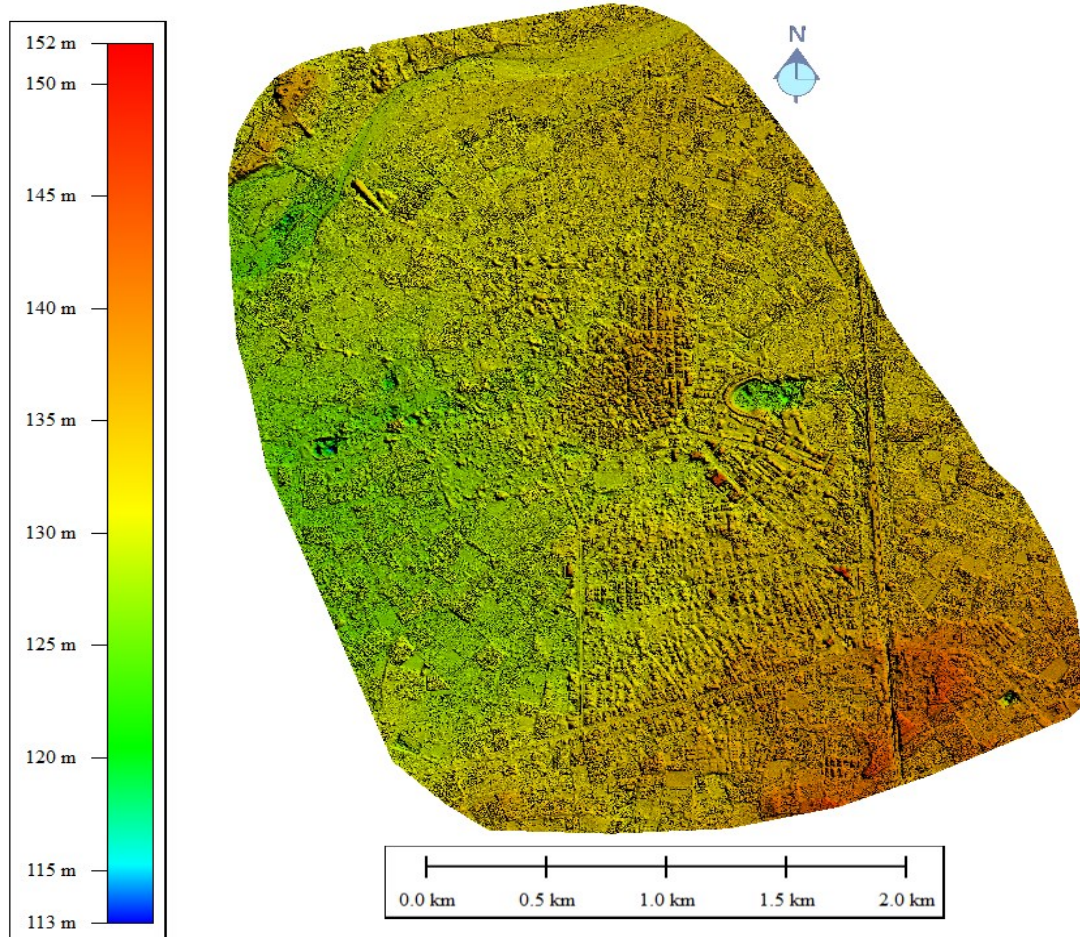


Figure 8. UAS generated DEM

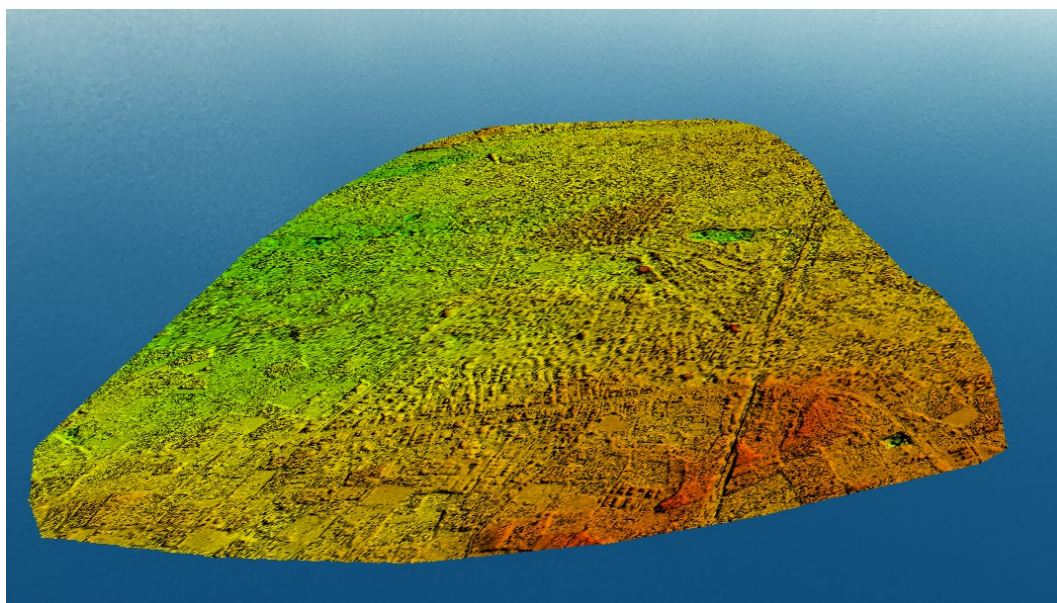


Figure 9. 3D view of high resolution DEM

4.1 DEM mosaicking

4.1.1 IDW method using Global Mapper

The final output obtained by merging the UAV based DEM for Dhanera city and CARTOSAT DEM for entire rel river watershed using IDW method. The basic limitation of this merging method is that the file size of merged DEM is too high (approx. 1TB) and it was unfit to be used as input DEM for flood modelling.

4.1.2 NN method using ArcGIS

The final output of NN merging method for Dhanera city containing UAV DEM and Rel River with CARTODEM. The merging contains less error compared to IDW method but is still unfit for flood modelling due to high file size (approx. 150GB). Thus, flood modelling is done only for a small section to compare the results.

4.1.3 Stitching method using HEC-RAS

The final output obtained can be seen in Figure 10 for merging UAV and CARTOSAT based DEMs in HEC-RAS by stitching method. This method is most suitable as it gives the better modelling results. The section as considered earlier is clipped for this DEM also and 2D unsteady flood modelling is performed (Figure 11).

4.1.4 Cartosat DEM

A section was clipped from all the merged DEM and 2D flood modelling was performed and the depth profile was generated. (Figure 12). The results of all the merged DEM are compared with actual CARTOSAT data DEM. It is

observed that the depth -time Series plot of CARTOSAT DEM (Figure 12) validates accurately to the DEM merged by Stitching method.

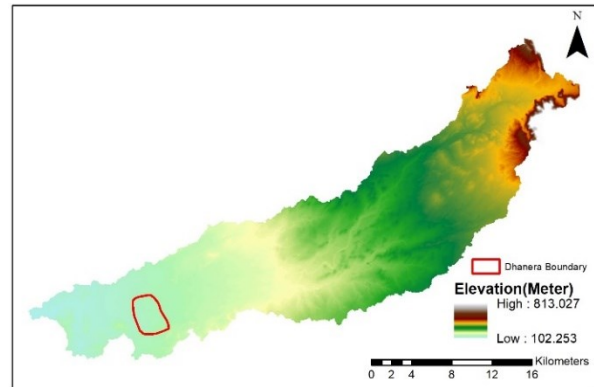


Figure 10. Terrain Stitching Method in HEC-RAS

4.2 Error analysis

R^2 values are obtained based on depth and inundation area values. R^2 is considered as a parameter to check whether which of the merged DEM matches closely with the observed river gauge data. Depth and inundation areas are calculated for all the merged type DEM and CARTOSAT DEM as shown in Table. 1 and Figure 13. It is observed that the area and depth values of stitching method matches closely with the observed, which shows the reliability of merging method.

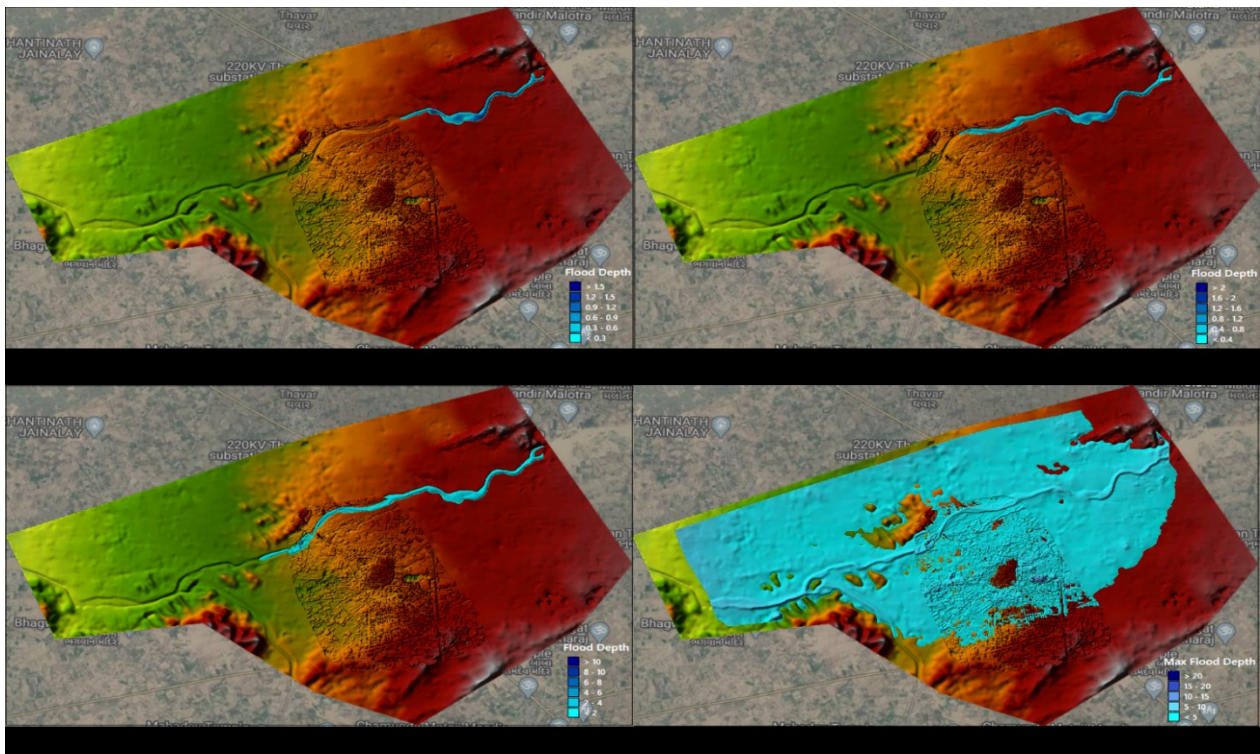


Figure 11. Depth Profile tiles of a) b) c) and d) of the Mosaic DEM (UAV and CARTOSAT)

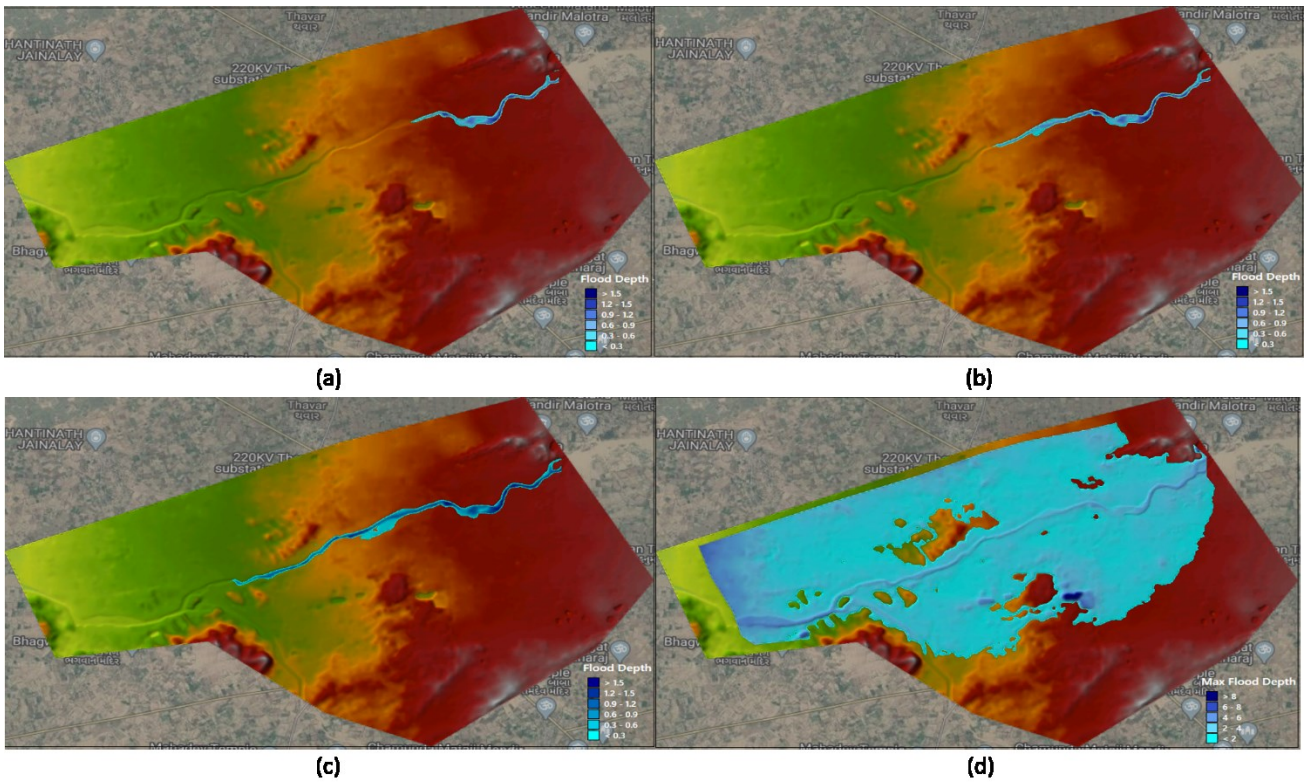
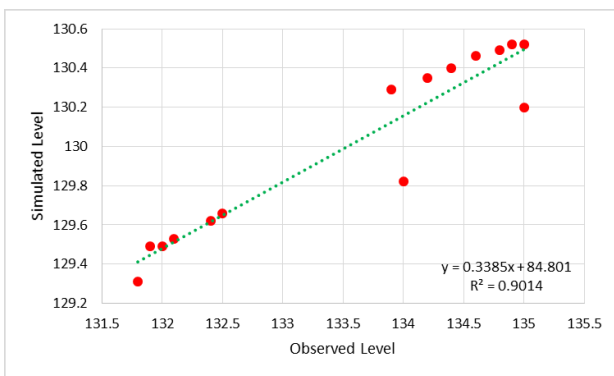


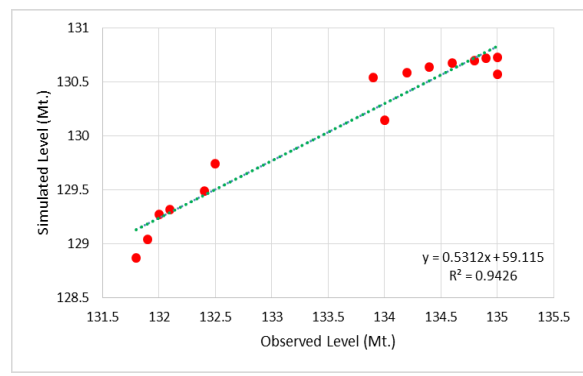
Figure 12. Depth Profile tiles of a) b) c) and d) of CARTOSAT DEM

Table 1. Comparison of Results

Sr.No	List of Parameters	CARTOSAT DEM	Stitching method in HEC-RAS
1	Inundation Area (km ²)	26.03	25.75
2	R ² Value	0.9014	0.9426



a)



b)

Figure 13. Correction of Observed Gauge level and Simulated Levels a) CARTOSAT DEM b) Mosaic DEM

5. Discussion

1. IDW (Inverse Distance Weighing) method in Global mapper software and Nearest Neighbor method using ArcGIS was used to mosaic both the DEM. The output file size is too high which is not suitable for modelling.
2. Terrain stitching method provides reliable output for flood estimation, hence applicable for cost-effective approach for accurate flood estimation of flash flooding in an urban and riverine region. The file size is 342MB and the processing time is 45 minutes.

3. Value of RMSE for stitching method is lowest out of all as shown in Table 1. Hence Stitching method is considered better out of all the methods.
4. The future stage involves flow simulation using hydrodynamic modelling. Prepared high resolution mosaicked DEM can be used for Flash Flood Hydrodynamic modelling. UAS based DEM can be merged with other open source DEMs like SRTM, ALOS, etc. and also the results can be compared further. Other parameters like arrival time and extreme flooding can be taken into consideration for flood

modelling. Merging methods using GRASS GIS software can also be considered for comparison.

6. Conclusions

Flood are the most vulnerable hazards for developing countries, cause a damage of properties and productivity in large extent, although the appropriate assessment techniques in urban and riverine area would decrease the flood catastrophe and reduce the human risk. Flood inundation and risk maps prepared from hydrodynamic modelling are purely depends on the accuracy of high resolution DEM. Preparation of high resolution DEM for entire catchments are cost associated and not an economic option for flood assessment in developing countries, therefore this study covers the development of high resolution DEM using UAS techniques and mosaics it with satellite based DEM. Merging through stitching method is more accurate from all other methods but also it gives a convenience to researcher to deal with big data in a short time. The terrain generation helps us to deal with DEM of different resolution at a same time which is beneficial in terms of hydrodynamic modelling. The study demonstrated the generation of DEM by UAV system and photogrammetry for Dhanera city which can be used a better data source for urban flood modelling. A very high resolution of DEM of accuracy 3.6cm is generated as an output which can be then merged with open source DEM or other satellite based DEM. Various methods for DEM fusion have been analysed by comparative statements which lastly conclude terrain stitching method provides the reliable output for flood mapping, hence applicable as cost-effective approach for accurate flood mapping in an urban and riverine region. Furthermore when the results of all mosaicked DEM were compared, terrain stitching merged DEM gave the best matched results with CARTOSAT DEM based on parameters like depth and inundation area. Thus a fusion of UAV based DEM and other DEM can be used a good input data source in flood mapping. This study would help to frame the guideline for use of Unmanned Aerial Systems (UAS) in post flood response activity in India.

Acknowledgements

Corresponding author would like to thanks SAC-ISRO for providing the financial support [Grant No: SAC/EPESA/GHCAG/LHD/SARITA/01/19] to execute the work. Also thanks to Mr. Raviraj and Ms. Heena, PDEU for providing initial support to carry out the research work.

References

Agnihotri P. G., S. Eslamian, D. Patel, and A. I. Pathan. (2021). Comparative analysis of 1D hydrodynamic flood model using globally available DEMs a case of the coastal region. *International Journal of Hydrology Science and Technology*, 1(1), 1. <https://doi.org/10.1504/IJHST.2021.10034760>

Ahmad A. (2011). Digital mapping using low altitude UAV. *Pertanika Journal of Science and Technology*, 19(SPEC. ISSUE), 51–58.

Ajayi O. G., A. A. Salubi, A. F. Angbas, and M. G. Odigure. (2017). Generation of accurate digital elevation models from UAV acquired low percentage overlapping images. *International Journal of Remote Sensing*, 38(8–10), 3113–3134. <https://doi.org/10.1080/01431161.2017.1285085>

Casado M. R., T. Irvine, S. Johnson, M. Palma, and P. Leinster. (2018). The use of unmanned aerial vehicles to estimate direct tangible losses to residential properties from flood events: A case study of Cockermouth Following the Desmond Storm. *Remote Sensing*, 10(10), 1–21. <https://doi.org/10.3390/rs10101548>

Glas H., P. De Maeyer, S. Merisier, and G. Deruyter. (2020). Development of a low-cost methodology for data acquisition and flood risk assessment in the floodplain of the river Moustiques in Haiti. *Journal of Flood Risk Management*, 13(2), 1–17. <https://doi.org/10.1111/jfr3.12608>

Govedarica M., G. Jakovljević, and F. Álvarez-Taboada. (2018). Flood risk assessment based on LiDAR and UAV points clouds and DEM. *Remote Sensing for Agriculture, Ecosystems, and Hydrology XX*, 10783, 66–76. <https://doi.org/10.1117/12.2513278>

Gupta K. (2020). Challenges in developing urban flood resilience in India. *Philosophical Transactions of the Royal Society A: Mathematical, Physical and Engineering Sciences*, 378(2168). <https://doi.org/10.1098/rsta.2019.0211>

GW Brunner. (2014). Combined 1D and 2D Modeling with HEC-RAS. US Army Corps of Engineers.

HEC-RAS. (2016). HEC-RAS user's Manual.

Jakovljevic G., M. Govedarica, F. Alvarez-Taboada, and V. Pajic. (2019). Accuracy assessment of deep learning based classification of LiDAR and UAV points clouds for DTM creation and flood risk mapping. *Geosciences (Switzerland)*, 9(7). <https://doi.org/10.3390/geosciences9070323>

Kim K. and J. Davidson. (2015). Unmanned aircraft systems used for disaster management. *Transportation Research Record*, 2532, 83–90. <https://doi.org/10.3141/2532-10>

Lakshmi S. E. and K. Yarrakula. (2018). Review and critical analysis on digital elevation models. *Geofizika*, 35(2), 129–157. <https://doi.org/10.15233/gfz.2018.35.7>

Leitão J. P., M. Moy De Vitry, A. Scheidegger, and J. Rieckermann. (2016). Assessing the quality of digital elevation models obtained from mini unmanned aerial vehicles for overland flow modelling in urban areas. *Hydrology and Earth System Sciences*, 20(4), 1637–1653. <https://doi.org/10.5194/hess-20-1637-2016>

Memon N., D. P. Patel, N. Bhatt, and S. B. Patel. (2020). Integrated framework for flood relief package (FRP) allocation in semiarid region: a case of Rel River flood, Gujarat, India. In *Natural Hazards (Vol. 100, Issue 1)*. Springer Netherlands. <https://doi.org/10.1007/s11069->

019-03812-z

Nagesh Kumar D., A. R. Shastry, and K. Srinivasa Raju. (2020). Delineation of flood-prone areas using modified topographic index for a river basin. *H2Open Journal*, 3(1), 58–68. <https://doi.org/10.2166/h2oj.2020.021>

NDMG. (2008). National Disaster Management Guideline.

NDMP. (2019). National Disaster Management Plan.

Ogunbadewa E. Y. (2012). Investigating availability of cloud free images with cloud masks in relation to satellite revisit frequency in the Northwest of England. *Contributions to Geophysics and Geodesy*, 42(1), 63–100.

Pandey R. K., J. F. Crétaux, M. Bergé-Nguyen, V. M. Tiwari, V. Drolon, F. Papa, and S. Calmant. (2014). Water level estimation by remote sensing for the 2008 flooding of the Kosi River. *International Journal of Remote Sensing*, 35(2), 424–440. <https://doi.org/10.1080/01431161.2013.870678>

Pandya U., D. P. Patel, and S. K. Singh. (2021). A flood assessment of data scarce region using an open-source 2D hydrodynamic modeling and Google Earth Image: a case of Sabarmati flood, India. *Arabian Journal of Geosciences*, 14(21), 2200. <https://doi.org/10.1007/s12517-021-08504-2>

Patel D. P. and U. D. Pandya. (2021). Flood stages assessment using open source 1D hydrodynamic modelling in data scarce region. *International Journal of Hydrology Science and Technology*, 1(1), 1. <https://doi.org/10.1504/IJHST.2021.10039735>

Patel D. P., J. A. Ramirez, P. K. Srivastava, M. Bray, and D. Han. (2017). Assessment of flood inundation mapping of Surat city by coupled 1D/2D hydrodynamic modeling: a case application of the new HEC-RAS 5. *Natural Hazards*, 89(1), 93–130. <https://doi.org/10.1007/s11069-017-2956-6>

Patel D. P. and P. K. Srivastava. (2014). Application of Geo-Spatial Technique for Flood Inundation Mapping of Low Lying Areas. *Remote Sensing Applications in Environmental Research*. Society of Earth Scientists Series. Springer, Cham, 113–130. https://doi.org/10.1007/978-3-319-05906-8_7

Patel D. P., P. K. Srivastava, S. K. Singh, C. Prieto, and D. Han. (2020). One-Dimensional Hydrodynamic Modeling of the River Tapi. *Techniques for Disaster Risk Management and Mitigation*, 209–235. <https://doi.org/10.1002/9781119359203.ch16>

Pathan A. I., P. G. Agnihotri, D. Patel, and C. Prieto. (2021). Identifying the efficacy of tidal waves on flood assessment study — a case of coastal urban flooding. *Arabian Journal of Geosciences*, 14(20), 2132. <https://doi.org/10.1007/s12517-021-08538-6>

Petrasova A., H. Mitasova, V. Petras, and J. Jeziorska. (2017). Fusion of high-resolution DEMs for water flow modeling. *Open Geospatial Data, Software and Using UAV SfM Supports Classical Theory*. *Remote*

Standards, 2(1), 0–7. <https://doi.org/10.1186/s40965-017-0019-2>

Poon J., C. S. Fraser, Z. Chunsun, L. I. Zhang, and A. Gruen. (2005). Quality assessment of digital surface models generated from ikonos imagery. *Photogrammetric Record*, 20(110), 162–171. <https://doi.org/10.1111/j.1477-9730.2005.00312.x>

Popescu D., L. Ichim, and F. Stoican. (2017). Unmanned aerial vehicle systems for remote estimation of flooded areas based on complex image processing. *Sensors (Switzerland)*, 17(3). <https://doi.org/10.3390/s17030446>

Prieto C., D. Patel, and D. Han. (2020). Preface: Advances in flood risk assessment and management. *Natural Hazards and Earth System Sciences*, 20(4), 1045–1048. <https://doi.org/10.5194/nhess-20-1045-2020>

Quiroga V. M., S. Kurea, K. Udoa, and A. Manoa. (2016). Application of 2D numerical simulation for the analysis of the February 2014 Bolivian Amazonia flood: Application of the new HEC-RAS version 5. *Ribagua*, 3(1), 25–33. <https://doi.org/10.1016/j.riba.2015.12.001>

Rawat J. S., V. Biswas, and M. Kumar. (2013). Changes in land use/cover using geospatial techniques: A case study of Ramnagar town area, district Nainital, Uttarakhand, India. *Egyptian Journal of Remote Sensing and Space Science*, 16(1), 111–117. <https://doi.org/10.1016/j.ejrs.2013.04.002>

Reuter H. I., A. Nelson, and A. Jarvis. (2007). An evaluation of void-filling interpolation methods for SRTM data. *International Journal of Geographical Information Science*, 21(9), 983–1008. <https://doi.org/10.1080/13658810601169899>

Robinson N., J. Regetz, and R. P. Guralnick. (2014). EarthEnv-DEM90: A nearly-global, void-free, multi-scale smoothed, 90m digital elevation model from fused ASTER and SRTM data. *ISPRS Journal of Photogrammetry and Remote Sensing*, 87, 57–67. <https://doi.org/10.1016/j.isprsjprs.2013.11.002>

Sahid A. W. Nurrohman, and M. P. Hadi. (2018). An investigation of Digital Elevation Model (DEM) structure influence on flood modelling. *IOP Conference Series: Earth and Environmental Science*, 148(1). <https://doi.org/10.1088/1755-1315/148/1/012001>

Sahoo S. N. and P. Sreeja. (2017). Development of Flood Inundation Maps and Quantification of Flood Risk in an Urban Catchment of Brahmaputra River. *ASCE-ASME Journal of Risk and Uncertainty in Engineering Systems, Part A: Civil Engineering*, 3(1), 1–11. <https://doi.org/10.1061/ajrua6.0000822>

Saksena S. and V. Merwade. (2015). Incorporating the effect of DEM resolution and accuracy for improved flood inundation mapping. *Journal of Hydrology*, 530, 180–194. <https://doi.org/10.1016/j.jhydrol.2015.09.069>

Schumann Muhlhausen, and Andreadis. (2019). Rapid Mapping of Small-Scale River-Floodplain Environments. *Sensing*, 11(8), 982. <https://doi.org/10.3390/rs11080982>

Șerban G., I. Rus, D. Vele, P. Brețcan, M. Alexe, and D. Petrea. (2016). Flood-prone area delimitation using UAV technology, in the areas hard-to-reach for classic aircrafts: case study in the north-east of Apuseni Mountains, Transylvania. *Natural Hazards*, 82(3), 1817–1832. <https://doi.org/10.1007/s11069-016-2266-4>

Tokarczyk P., J. P. Leitao, J. Rieckermann, K. Schindler, and F. Blumensaat. (2015). High-quality observation of surface imperviousness for urban runoff modelling using

UAV imagery. *Hydrology and Earth System Sciences*, 19(10), 4215–4228. <https://doi.org/10.5194/hess-19-4215-2015>

Vant-Hull B., A. Marshak, L. A. Remer, and Z. Li. (2007). The effects of scattering angle and cumulus cloud geometry on satellite retrievals of cloud droplet effective radius. *IEEE Transactions on Geoscience and Remote Sensing*, 45(4), 1039–1044. <https://doi.org/10.1109/TGRS.2006.890416>

Assessment of surface flooding over India from passive microwave radiometer

Rohit Pradhan*, Nimisha Singh and R P Singh
Land Hydrology Division, EPSA, Space Applications Centre (ISRO), Ahmedabad, India
*Email: rohithp@sac.isro.gov.in

(Received: Aug 19, 2021; in final form: Oct 6, 2021)

Abstract: Orbital measurements of surface flooding have routinely been carried out using Synthetic Aperture Radars and Altimeters. The ability of SAR and Altimeter to provide all-weather, high-resolution and accurate data is diminished by their poor revisit times. In the event of flood, rapid availability of near real-time data for damage assessment and relief applications is of utmost priority. Passive Microwave Radiometers like Advanced Microwave Scanning Radiometer – 2 (AMSR2) provide high repetivity of 1-2 days with coarser resolution, but retain their all-weather capability. In this paper, we present a method for detection and assessment of regional-scale surface flooding using Brightness Temperature at 36.5 GHz from AMSR2. Microwave Polarization Difference Index (MPDI) was used to identify flooded pixels at national scale and the severity of flood was characterised using a normalised flood index. Spatial variability and temporal frequency of surface flooding over India was studied for the period 2013-2020. Near real-time Flood Index product, using this algorithm is available on VEDAS web portal (vedas.sac.gov.in).

Keywords: Flood, inundation, passive radiometer, microwave, AMSR2.

1. Introduction

Flood is one of the most frequent natural disasters affecting millions of people worldwide. Mapping and forecasting these flood events is essential for any flood mitigation plan that can save thousands of lives. Surface hydrological variables like river water level, surface water extent, soil moisture etc. are routinely observed from satellites (Sheffield et al., 2018). Altimeters and Synthetic Aperture Radars (SAR) provide high precision and high-resolution all-weather data, which is key to retrieving these hydrological parameters. However, they suffer from poor revisit time which hampers their use during floods. Altimeters with typical revisit times of 10-35 days may not be able to capture peak water level and flood signal. Similarly, SAR data with 10-day revisit period and limited swath may not always be sufficient to delineate catchment-level flood extent and perform damage assessment.

Microwave radiometers (e.g. AMSRE, AMSR2) record emission from Earth's surface and atmosphere to estimate Brightness Temperature at multiple frequencies and retrieve a variety of geophysical parameters with a revisit time of 1-2 days (Cho et al., 2017). Soil moisture, water vapor, snow cover, sea ice etc. have been retrieved operationally from passive microwave radiometers (Njoku et al., 2003; Kazumori et al., 2012; Dai et al., 2012; Spreen et al., 2008). Emission and reflectivity in microwave region is affected by soil properties such as dielectric constant, soil roughness etc (Ulaby et al., 1981, 1986). Over land surfaces, brightness temperature is related with emissivity and temperature (Fung et al., 1994). When soil surface is completely inundated by water, the emissivity decreases causing reduction in Brightness Temperature (BT) measured in microwave frequencies. The reduction of BT in horizontal polarization is greater compared to that in vertical polarization (Ulaby et al., 1978).

Microwave indices obtained from multi-frequency radiometry have been used for detecting characteristics of land and water surfaces (Paloscia et al., 2018). Brightness Temperature Polarization Ratio (PR), also known as

Microwave Polarisation Difference Index (MPDI), at a particular frequency is one such index that is used to study soil moisture, surface inundation and vegetation characteristics (Gupta et al., 2019; Njoku et al., 2003; Zheng et al., 2016) and is given as:

$$MPDI = \frac{T_{bV} - T_{bH}}{T_{bV} + T_{bH}} = \frac{\epsilon_v - \epsilon_h}{\epsilon_v + \epsilon_h} \quad (1)$$

Where T_{bH} and T_{bV} are Brightness Temperatures and ϵ_H and ϵ_V are emissivity in H and V polarisations, respectively. This index removes the effect of fluctuations in physical temperature of target and considers only the difference in emissivity in the two polarisations. MPDI is governed by the surface water extent and is highest for water-covered regions amongst all the LULC types studied by Li et al. (2013).

Advanced Microwave Scanning Radiometer (AMSR2) is a passive microwave radiometer developed by Japanese Aerospace eXploration Agency (JAXA) that can record BT at seven frequencies in both horizontal (H) and vertical (V) polarisations. Lower frequencies recorded by passive microwave radiometers are less affected by atmosphere but provide poor spatial resolution. On the other hand, clouds and atmospheric water vapor influence higher frequencies (Shi et al., 2015). Passive radiometer data at 36 GHz has been used to retrieve river discharge and delineate flood extent, as it is mainly sensitive to fluctuations in water surface extent (Brakenridge et al., 2007, 2012). This frequency provides an optimum spatial resolution, is less influenced by atmosphere and is sensitive to fluctuations in surface water, making it best suited for detection and monitoring of floods. This paper highlights the utility of passive microwave radiometer to map surface flooding over India. In this paper, we present a novel technique for estimation of surface flooding using AMSR2 derived MPDI at 36.5 GHz over India. MPDI based flood index maps are generated which express the intensity of flooding in a given pixel and long-term analysis of flooding over India is analyzed using this method. Impact of specific extreme events like cyclones

are studied in terms of surface flooding caused by the event.

2. Study area and data used

This study was carried out over India and surrounding regions that see high prevalence of flood events. Study area lies between 5° - 40° N and 65° – 100° E excluding the seas and high altitude regions. This region experiences maximum flooding during the monsoon months of June to September with different catchments experiencing peak flooding at different times. Excess precipitation, overflowing rivers and release from man-made structures can contribute to floods in the region. These events can last anywhere from a few days to weeks depending on intensity of flood and its driving factors.

AMSR2 is a passive microwave radiometer that provides BT data in seven frequencies with varying spatial resolutions (Table 1). This data is re-gridded onto global grids at 0.1° and 0.25° resolutions and provided as standard Level 3 products. In this study, we use Level 3 Brightness Temperature (BT) data from AMSR2 at 36.5 GHz in both H and V polarisations for the period 2013-2020 (data available from ftp.gportal.jaxa.jp). At 36.5GHz, the IFOV of AMSR2 is approximately 7x12 km. After re-gridding, this data is available at 0.1°x0.1° spatial resolution over entire globe with 2-day repeat coverage within the study region. As a result, the product is generated as composite of two days. Moderate resolution Imaging Sensor (MODIS) based Land Use Land Cover (LULC) data at 5km grid is used to filter out desert regions and analyse land cover based MPDI.

Table 1. Description of AMSR2 frequencies

SNo.	Central Frequency (GHz)	Polarization	IFOV (km)
1	6.925	H, V	35 × 62
2	7.3	H, V	35 × 62
3	10.65	H, V	24 × 42
4	18.7	H, V	14 × 22
5	23.8	H, V	11 × 19
6	36.5	H, V	7 × 12
7	89.0	H, V	3 × 5

3. Methodology

MPDI (using Equation 1) for study region is computed using 0.1° x0.1° daily gridded AMSR2 BT at 36.5GHz in H and V polarisations. Sea regions are masked out and only land areas are selected for further processing. MPDI computed for the period 2013-2020 is used to generate long-term mean and standard deviation for each grid pixel. These long-term statistics serve as a diagnostic tool for assessing if the MPDI of a particular pixel is anomalously high, which might indicate inundation. These statistics are used to compute the MPDI range for partially to completely inundated pixels, which serves as threshold for identifying flooded pixels and computing a normalised flood index.

For estimating flood extent from daily AMSR2 data, MPDI image is computed from BT in H and V polarisations. Pixels with MPDI>0.1 are marked as completely inundated, whereas, pixels with MPDI between 0.01 and 0.1 are marked as partially inundated. MODIS LULC mask is applied to mask out desert regions as they too have high MPDI values due to large differences in emissivity in H and V polarisation. Pixels with MPDI between 0.01 and 0.1 are further verified to see if their polarisation ratio value exceeds 1.5 times the standard deviation from long-term mean. If these criteria are met, the pixel is confirmed as inundated and further process of converting MPDI to normalised flood index is carried in the next step. Pixels with MPDI<0.01 are marked as non-inundated and not considered for further analysis.

Once flooded pixels are identified based on MPDI, its polarisation ratio is converted to a normalised flood index value ranging from 0 to 1. This flood index is a linear scaling of MPDI values between 0.01 to 0.1 for the identified flooded pixels. For values of MPDI>0.1, flood index is set as 1. Equation 2 describes the linear conversion of MPDI to flood index values used as an indicator of flooding intensity.

$$\text{Flood Index} = \begin{cases} 1 & ; \text{MPDI} > 0.1 \\ \frac{\text{MPDI} - 0.01}{0.1 - 0.01} & ; 0.01 \leq \text{MPDI} \leq 0.1 \\ 0 & ; \text{MPDI} < 0.01 \end{cases} \quad (2)$$

Flood index map of each day is composited with the next day to obtain 2-day flood composites. Mean value is taken for pixels where data is available for both dates. Similarly, mean flood index maps for monsoon season and entire year are also generated for analysing extent, intensity and duration of floods throughout the study area. Flood index maps for specific events, like cyclone Tauktae and Yaas during 2021, were generated for understanding the performance of flood detection algorithm during extreme events. Flowchart of methodology used in this study is shown in Figure 1.

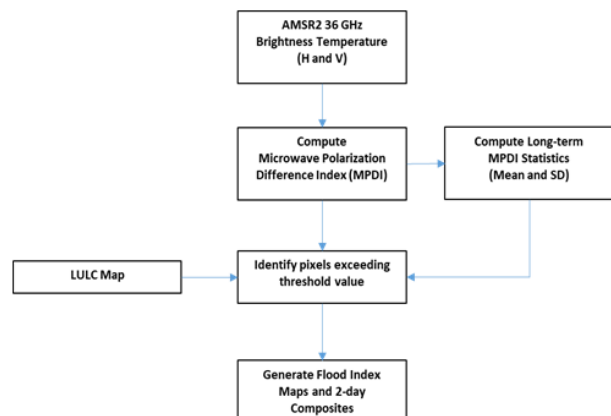


Figure 1. Flowchart of methodology implemented in this study

4. Results and discussion

4.1 MPDI and its statistics

Figure 2 shows the mean and standard deviation of computed MPDI between 2013-2020 for the study region. We can clearly see that MPDI is greater than 0.1 for seas, water bodies and lakes. MPDI for land areas is typically lower than 0.01 represented here in dark blue. Deserts and high altitude regions show high MPDI due to differences in emissivity in H and V polarisations. To overcome this, MODIS LULC was used to mask out the desert regions and barren land areas from the output flood index maps. This does not have any impact on the flood maps for major part of the Indian landmass. Surface vegetation influences MPDI and makes it difficult to detect flood in heavily vegetated areas, which is a major limitation of this work.

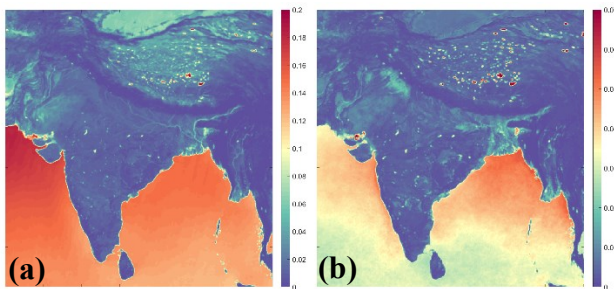


Figure 2. (a) Mean and (b) standard deviation of MPDI for the study region during 2013-2020.

4.2 Flood Index

Daily flood index maps were generated for the study period and averaged to get the mean flood index map. For dissemination purpose, 2-day composite flood index maps were generated to cover the gaps in daily BT gridded data. Figure 3 shows the mean flood index averaged over the study period for all pixels within the study region. It is clear that flood index picks up water bodies like rivers, lakes, reservoirs with good accuracy. Tributaries of rivers and frequently flooded regions are also picked up by the flood index.

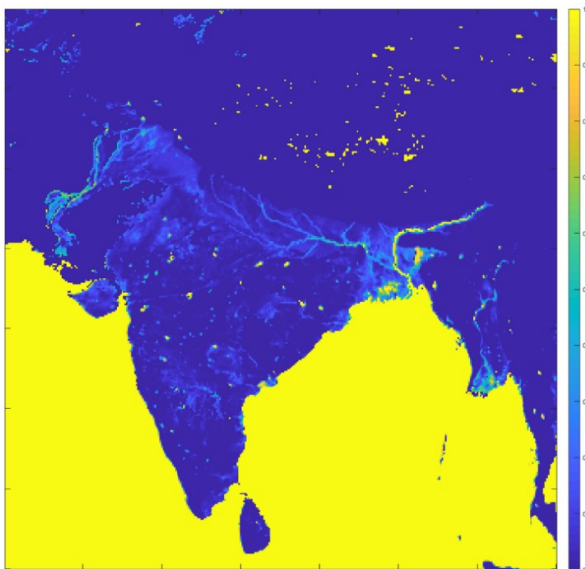


Figure 3. Mean flood index map for the study period 2013-2020

However, regions under dense vegetation cover, like forests of Northeast India and Western Ghats, hardly show any inundated areas due to influence of vegetation on MPDI values. Due to coarse resolution of AMSR2 data, coastal regions show up as partially flooded as both sea water and coastal land is present within the same pixel. One feature of this flood index product is that it can also pick up inundated agricultural fields, which are typically associated with rice cultivation. This is prominent in Punjab and Haryana regions during May-June (Singh et al., 2017) and appear as inundated pixels in flood maps.

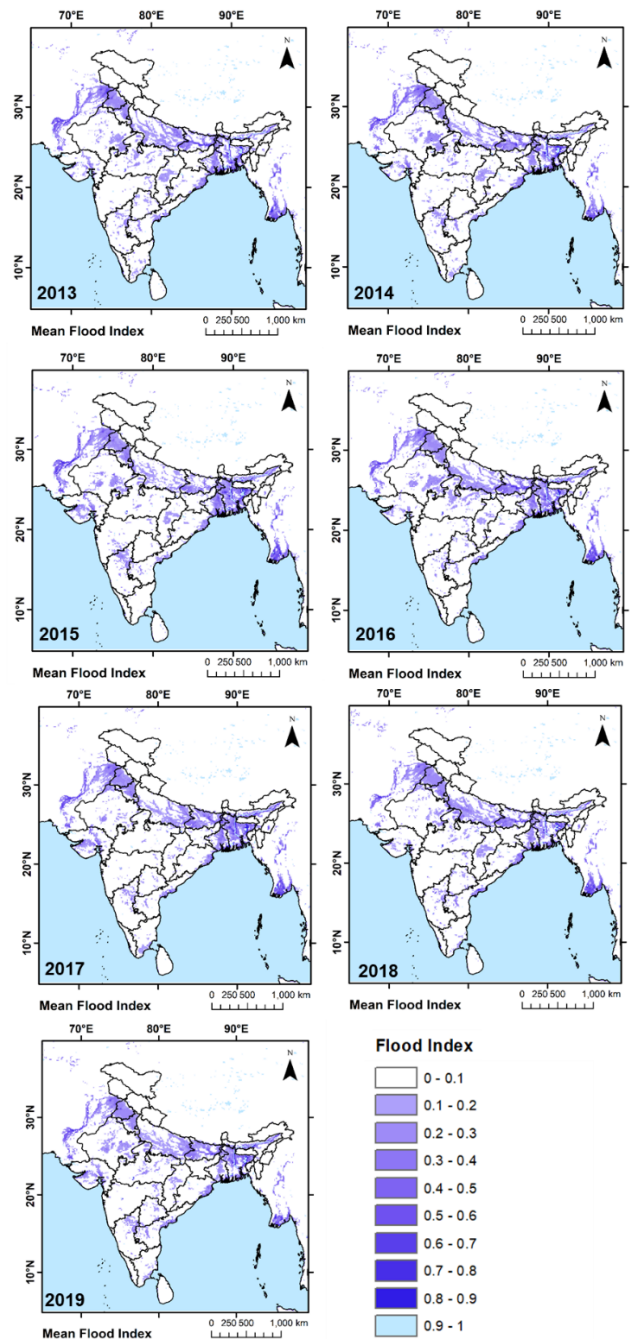


Figure 4. Mean flood index maps for monsoon (JJAS) season during 2013-2019.

Figure 4 shows the mean monsoonal flood index for each season between 2013-2019. Frequently inundated regions of Ganga and Brahmaputra basins are clearly seen along with the agricultural inundation for rice cultivation in

Punjab, Haryana, West Bengal and Chhattisgarh. Regions of Myanmar and Bangladesh that show frequent flooding, including river delta, are represented as flooded in these maps. From Figures 3 and 4 mean flood index maps, it is clear that the flood index described in this study represents frequently flooded regions during monsoon periods. To understand the performance of this technique during localised flood events, we look at the 2-day composite flood index maps for certain extreme events like cyclones. Figure 5 shows the prevalence of flood across the study area for the year 2020. Pixels where flood index is greater than 0.5 are only considered and the total number of days for which index was above this value is shown as prevalence map. This map clearly shows the frequently flooded regions of India and the persistence of flood in that region.

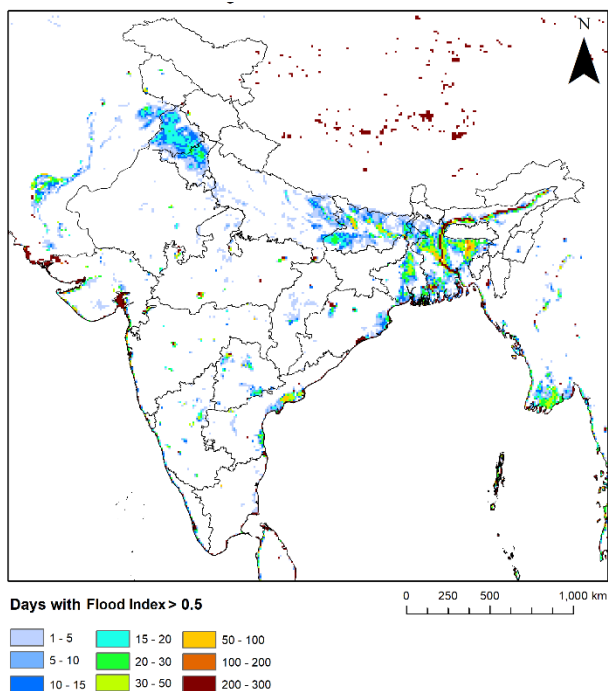


Figure 5. Number of flooding days during 2020 where pixels with flood index greater than 0.5 are considered as flooded.

4.3 Performance of Flood Index during extreme events

Tauktae, an extremely severe cyclonic storm, developed over Arabian Sea and made landfall over Gujarat near Diu on May 17, 2021. Figure 6 shows the 2-day composite flood index map for 18-19 May 2021 which clearly picks up the inundated areas. Heavy rain due to Cyclone Tauktae created flood like situation in many parts of Gujarat including the coastal districts of Amreli and Bhavnagar along with Rajkot, Botad, Ahmedabad and Surat. Effects of Cyclone Tauktae were felt inland, including Northern regions of Madhya Pradesh and parts of Uttar Pradesh as well.

Within a few days after Cyclone Tauktae, a very severe cyclonic storm named Yaas developed over Bay of Bengal and hit the Odisha coast on May 26, 2021. Figure 7 shows the 2-day composite flood index map for 27-28 May 2021 which clearly picks up the inundated areas.

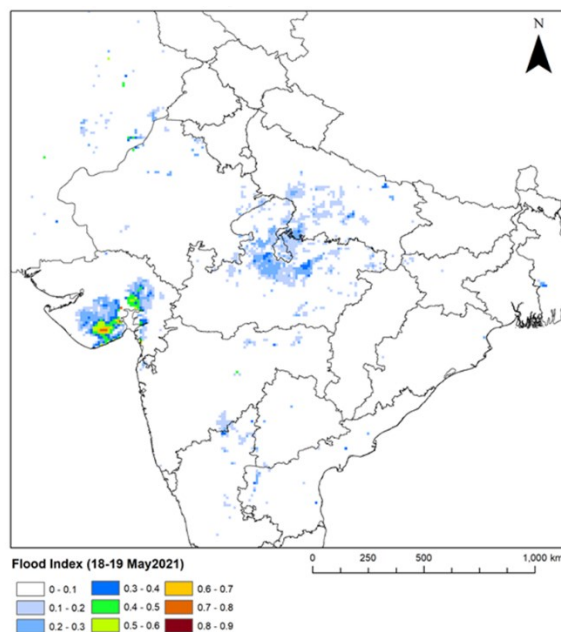


Figure 6. Flood index map for 18-19 May 2021 showing flooded regions due to impact of Cyclone Tauktae over Gujarat and central India.

Heavy rain from Cyclone Yaas created flood like situation in the coastal districts of Orissa and West Bengal. Effect of Cyclone Yaas was observed all the way upto Jharkhand, Bihar and Eastern parts of Uttar Pradesh. Coastal districts of Orissa including Bhadrak, Kendrapara and Balasore saw heavy flooding due to Cyclone Yaas. Patna and its adjoining districts in Bihar also saw flooding due to heavy rains from Cyclone Yaas which continued to batter the region on 26-27 May 2021. Surface flooding map using AMSR2 36 GHz MPDI clearly shows the affected regions of Orissa, Bihar, Jharkhand and West Bengal.

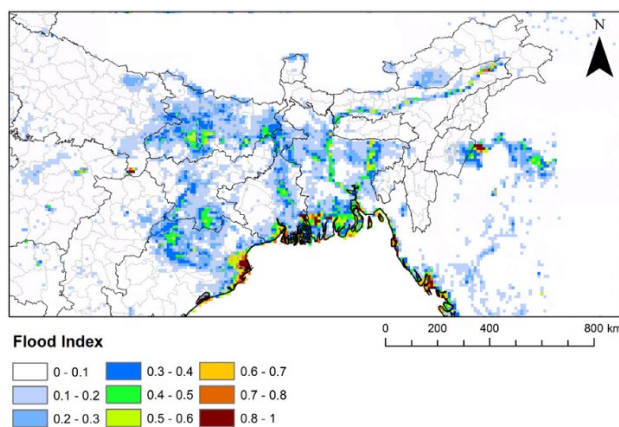


Figure 7. Flood index map for 27-28 May 2021 showing flooded regions due to impact of Cyclone Yaas over Odisha and Eastern India.

Figures 5 and 6 clearly show the capability of 36.5 GHz BT data in capturing signal of surface flooding and the corresponding flood index product in representing the severity of flooding at a regional scale. Multiple observations with 2-day repetivity can help us better understand the progression of flood wave across any catchment and help in preparedness and mitigation efforts during severe flood events.

5. Conclusions

In this paper, we present a novel technique for detecting surface flooding using AMSR2 Brightness Temperature at 36.5GHz. MPDI based flood index described in this study was able to detect inundated areas across India with two-day repetivity. Desert and barren land regions were masked out due to their high polarisation ratios. Agricultural fields of Punjab and Haryana that are inundated for rice cultivation were also picked up by this method. Performance of flood index was evaluated during flood events caused by Cyclone Tauktae and Yaas and showed good match with SAR based flood maps, although at a coarser resolution. Higher spatial coverage and two-day repetivity are two major strengths of this method for flood detection over conventional techniques.

Acknowledgements

This work was carried out under SARITA program of Land Hydrology Division, EPSA, SAC. The authors wish to thank Shri N M Desai, Director, SAC and Dr I M Bahuguna, Deputy Director, EPSA for their guidance and support. AMSR2 Brightness Temperature data from JAXA and MODIS LULC data from NASA are thankfully acknowledged.

References

- Brakenridge G.R., S. Cohen, A. J. Kettner, T. de Groeve, S. V. Nghiem, J. P. M. Syvitski and B. M. Fekete (2012). Calibration of Satellite Measurements of River Discharge Using a Global Hydrology Model, 475, 123-136.
- Brakenridge G.R., S. V. Nghiem, E. Anderson and R. Mic (2007). Orbital microwave measurement of river discharge and ice status. *Water Resources Research*, 43, W04405, doi:10.1029/2006WR005238.
- Cho E., C. H. Su, D. Ryu, H. Kim and M. Choi (2017). Does AMSR2 produce better soil moisture retrievals than AMSR-E over Australia? *Remote Sensing of Environment*, 188, 95-105.
- Dai L., T. Che, J. Wang and P. Zhang (2012). Snow depth and snow water equivalent estimation from AMSR-E data based on a priori snow characteristics in Xinjiang, China. *Remote Sensing of Environment*, 127, 14-29.
- Fung A. K. (1994). *Microwave scattering and emission models and their applications*. Norward M. A: Artech House.
- Gupta P.K., R. Pradhan, R. P. Singh and A. Misra (2019). Scatterometry for land hydrology science and its applications. *Current Science*, 117(6), 1014-1021.
- Kazumori M., T. Egawa and K. Yoshimoto (2012). A retrieval algorithm of atmospheric water vapor and cloud liquid water for AMSR-E, *European Journal of Remote Sensing*, 45(1), 63-74.
- Li Y., K. Zhao, X. Zheng and J. Ren (2013). Analysis of microwave polarization difference index characteristics about different vegetation types in northeast of China. *International Conference on Remote Sensing, Environment and Transportation Engineering, RSETE 2013*. 10.2991/rsete.2013.9.
- Njoku E. G., T. J. Jackson, V. Lakshmi, T. K. Chan and S. V. Nghiem (2003). Soil moisture retrieval from AMSR-E, *IEEE transactions on Geoscience and remote sensing*, 41(2), 215-229.
- Paloscia S., P. Pampaloni and E. Santi (2018). Radiometric microwave indices for remote sensing of land surfaces. *Remote Sensing*, 10(12), 1859.
- Shi L., Y. Qiu, J. Shi and S. Zhao (2015). Atmospheric influences analysis in passive microwave remote sensing. *2015 IEEE International Geoscience and Remote Sensing Symposium (IGARSS)*, 2334-2337, IEEE.
- Sheffield J., E. F. Wood, M. Pan, H. Beck, G. Coccia, A. Serrat- Capdevila and K. Verbist (2018). Satellite remote sensing for water resources management: Potential for supporting sustainable development in data- poor regions, *Water Resources Research*, 54(12), 9724-9758.
- Singh D., P. K. Gupta, R. Pradhan, R., A. K. Dubey and R. P. Singh (2017). Discerning shifting irrigation practices from passive microwave radiometry over Punjab and Haryana, *Journal of Water and Climate Change*, 8(2), 303-319.
- Spren G., L. Kaleschke and G. Heygster (2008). Sea ice remote sensing using AMSR- E 89- GHz channels, *Journal of Geophysical Research: Oceans*, 113(C2).
- Ulaby F.T., P. P. Batlivala and M. C. Dobson (1978). Microwave backscatter dependence on surface roughness, soil moisture and soil texture, Part-I: Bare soil, *IEEE Transactions on. Geoscience Electronics*, GE-16, 286-295.
- Ulaby F. T., R. K. Moore and A. K. Fung (1986). *Microwave Remote Sensing, from Theory to Applications*. Vol. 3, Deedham M. A.: Artech House.
- Ulaby F. T., R. K. Moore, R. K. and A. K. Fung (1981). *Microwave Remote Sensing, Fundamanetals and Radiometry*. Vol. 1, Deedham M. A.: Artech House.
- Zheng W., D. Sun and S. Li (2016). Coastal flood monitoring based on AMSR-E data. *2016 IEEE International Geoscience and Remote Sensing Symposium (IGARSS)*, 4399-4401, IEEE.

Flood assessment in the Brahmaputra River using microwave remote sensing and hydrological modelling

Amit Kumar Dubey* and R. P. Singh
Space Applications Centre, Ahmedabad, India
*Email: a_dubey@sac.isro.gov.in

(Received: Aug 28, 2021; in final form: Oct 06, 2021)

Abstract: Floods in the Brahmaputra River are very frequent and inundate large area of flood-plains. To assess the real time flood inundation, Synthetic Aperture Radar (SAR) observations are very crucial during the monsoon season. To understand and assess the flood conditions in the Brahmaputra River, a flood event in the year 2020 is selected for this study. To estimate the flood discharge hydrograph, WRF-Hydro model simulation is used. In this study, in synchronous Sentinel-1 SAR images are used to extract the flood inundation at middle reach of the Brahmaputra River. Flood inundation due to high flood discharge was delineated using logarithm of cross polarization (VH) ratio. The flood discharge during the flood event with high discharge ($\sim 50,000 \text{ m}^3/\text{sec}$) simulated through WRF-Hydro model and in-synchronous SAR images are found to be an effective combination for real-time flood assessment and modelling.

Keywords: Flood assessment, Hydrological modelling, WRF-Hydro

1. Introduction

Floods are widely occurring natural disaster worldwide, which affect the all aspects of human life (Subyani et al. (2017) and Serinaldi et al. (2018)). Rapidly warming climate and urbanization are one of the major factors behind large scale floods. (Apurv et al. (2015), Su et al. (2016), and Miller and Hutchins (2017)). Understanding of flood characteristics is import to mitigate the flood disaster effects in the flood-plain regions. Annual flooding in the Brahmaputra River is major concern for Assam, India and Bangladesh. Each year North eastern region receives very high intensity of rainfall starting with pre-monsoon rain spells. Different tributaries of the Brahmaputra also carry large amount of river discharge, therefore congestion of flow between rivers also inundate large region during high flow conditions. The Brahmaputra River originates from Tibet and flows through India and Bangladesh. It finally drains in to Bay of Bengal. Floods in the Brahmaputra not only affect large population it also submerges huge area of agriculture land and seriously affect the livelihood of millions of people. More intense rain and frequent flood events are predicted in the Brahmaputra River using climate change projections (Apurv et al. 2015 and Ghosh and Dutta 2012). The future projections

The Brahmaputra is large transboundary river with dynamic complex morphology. Each year it reshapes the river patterns due to high influx of sediment from upstream catchment (Karmaker et al. (2017) and Chembolu and Dutta (2018)). During the monsoon season the basin remains covered from clouds, therefore there is limitation in use of optical remote sensing. However, microwave SAR images provide better alternative for flood inundation mapping during monsoon season, due to its capability to see through clouds. Sentinel-1 satellite generate multi-temporal images for a region with 12-day repeat cycle with 1 satellite and 6-day repeat cycle with 2 satellites. It provides continuous coverage during the monsoon season, which makes it suitable candidate to monitor long duration floods in the Brahmaputra River.

Kaziranga National Park is one of the highest flood prone zone in the Brahmaputra river valley. It inundates each year as flood waves pass through the river. The floods in the year 2020 also inundates large region of Kaziranga National Park, which is diverse ecosystem and vulnerable to each year floods.

2. Study Area and Data

The Brahmaputra River originates from Tibet and travel through India and Bangladesh drains into the Bay of Bengal. It is one the major river system in the world. Its total length is 2900 km in which 918 km is in the India and 337 km in the Bangladesh. The rainfall pattern in the North Eastern part of India is very dynamic with average annual rainfall of 2300 mm over Assam (Singh et al. (2004)). The Brahmaputra is one of the highest flowing river of India with multiple flood waves within the monsoon season. The hydrograph varies from average lean flow of $4420 \text{ m}^3\text{s}^{-1}$ and average flood flow of $51156 \text{ m}^3\text{s}^{-1}$ with an average of 6 flood waves passing annually (Singh et al., 2004; Karmaker and Dutta (2010)). The Brahmaputra River basin is very large (Figure 1) and has varying river bed slope and river flow width from upstream to downstream of the river. The average bed slope is found in the range of 10^{-4} with braided belt width ranging between 2 km to 18 km (Goswami (1985)). The river has very fine bed material with highly morphologically dynamic features such as active bank erosion, river bed migration and sand bar deposition/erosion (Khan and Islam (2003), Sarma (2005), Sarker et al. (2014), and Chembolu and Dutta (2018)).

In this study, we have used Global Satellite Mapping of Precipitation (GSMaP) precipitation data for WRF-Hydro model simulations. GSMaP-gauge product version-7 which is calibrated with in-situ data is used for flood discharge simulations. Meteorological forcing for the WRF-Hydro was taken from 24 hr operational WRF forecast provided by Meteorological & Oceanographic Satellite Data Archival Centre (MOSDAC) at Space Applications Centre, Ahmedabad. Meteorological forcing consists air temperature (T2D), near-surface wind speed component u (U2D) and v (V2D), specific humidity (Q2D)

and shortwave radiation (SWDOWN), longwave radiation (LDOWN). Microwave images was used from Sentinel-1 satellite, which provide dual-polarization data primarily in VV and VH mode.

3. Methodology

In this study, we have used SAR images from Sentinel-1 satellite and an uncoupled WRF-Hydro model to study a flood event in the Brahmaputra River. The model is equipped with different terrestrial physics options such as overland flow, subsurface, and channel flow for discharge estimation. To generate daily discharge hydrograph WRF daily weather forecast was used as a WRF-Hydro model forcing. The model was simulated for the period of year 2013-2020 with calibration and validation on year 2018 and 2019, respectively. The details of model set-up, calibration and validation is documented in Dubey et al., 2021. The model performance was statistically satisfactory. Sentinel-1 satellite microwave images were used to extract flood inundation region for the region near

Kaziranga National Park. Microwave satellite images of cross-polarization were used in identification of flood inundation after the flood event (Figure 2). In this study we have used VH polarization instead of VV polarization for flood extraction. VV polarization is very sensitive to surface roughness characteristics, Hence, we have used amplitude ratio of VH polarization and its logarithm to identify the region of changes. The ratio of cross polarization (VH) for post and pre flood event highlighted the changes due to flood event.

4. Results and Discussion

The extreme flood event (Figure 4 to Figure 7) occurred in the month of July 2020 was simulated using WRF-Hydro model and it was found that it inundated large flood-plains. The simulated discharge revealed that the peak discharge was about 50,000 m³/sec at Guwahati for the Brahmaputra River. In synchronous satellite images of Sentinel-1 satellite were also analysed for the same period.

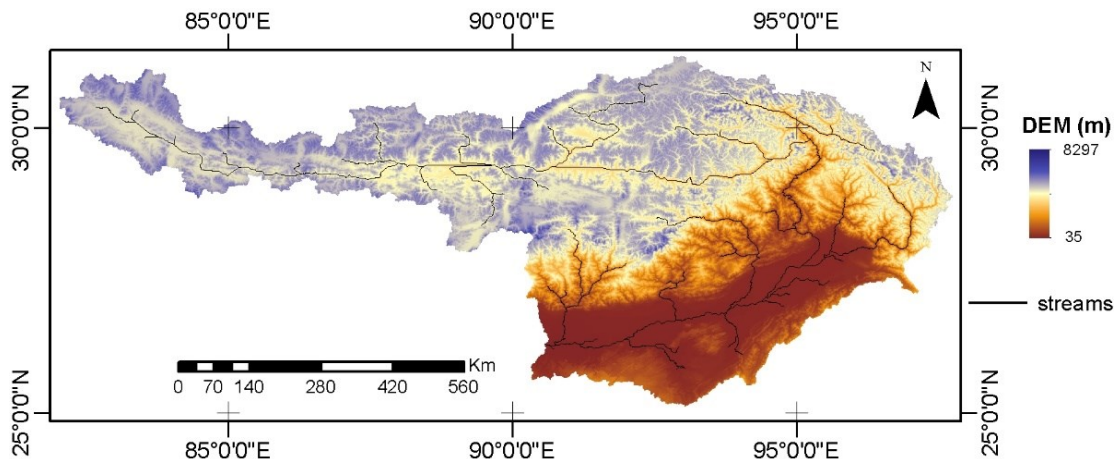


Figure 1. Study area showing drainage network, topography of the Brahmaputra River.

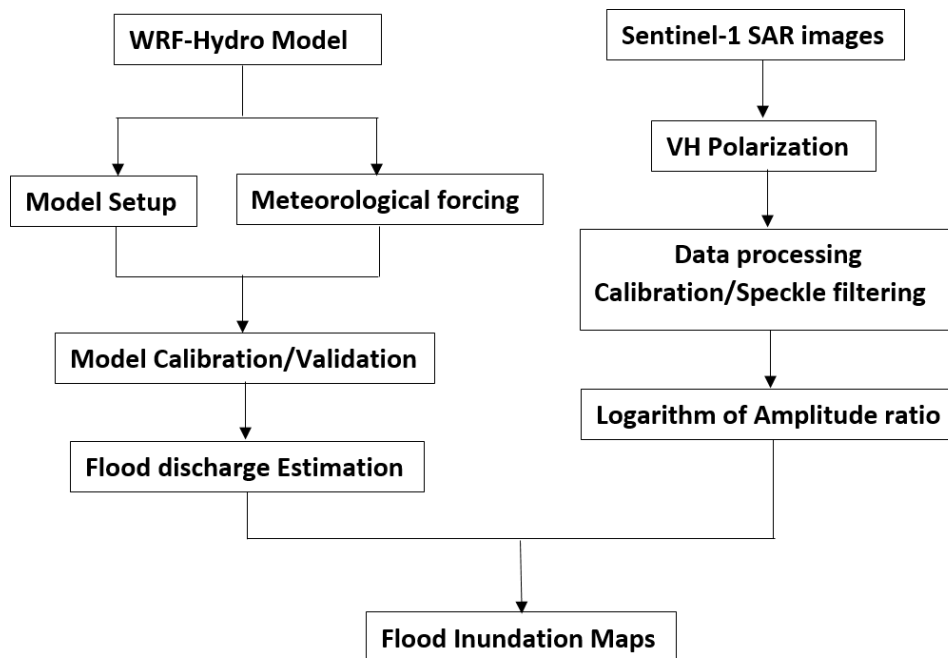


Figure 2. Flow chart showing the methodology adopted in this study.

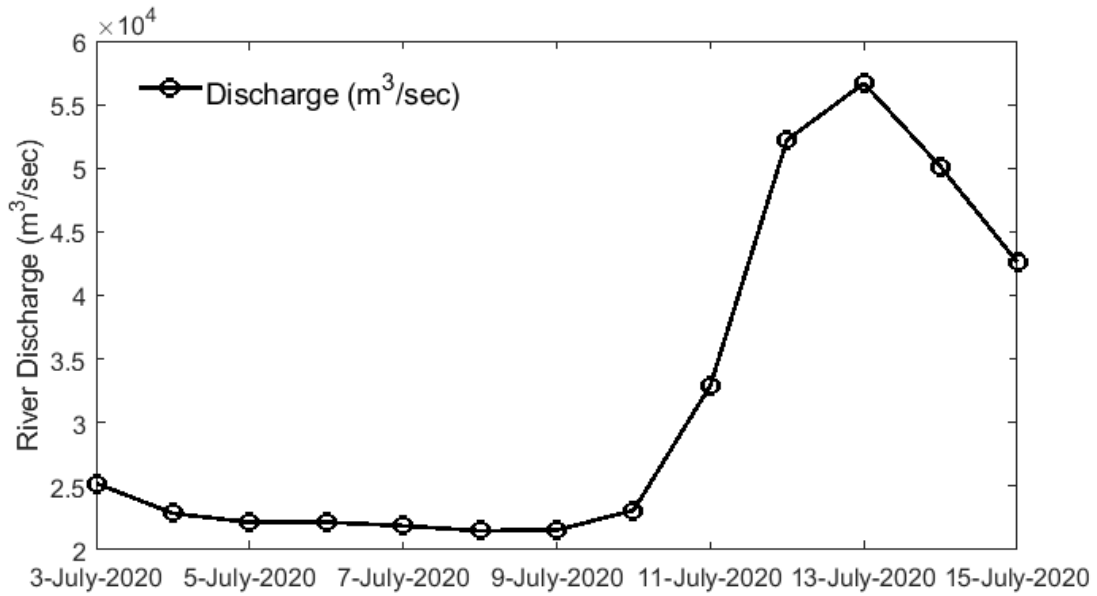


Figure 3. WRF-Hydro simulated discharge hydrograph for the flood event from 03-15 July 2020 in the Brahmaputra River.

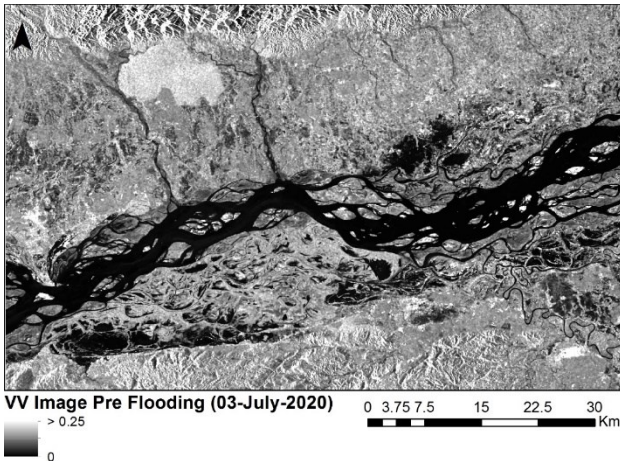


Figure 4. Sentinel-1 microwave satellite image of VV polarization prior to flood event (03-July-2020).

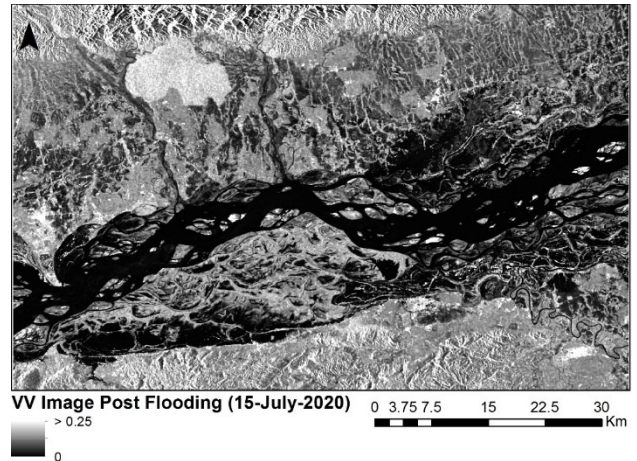


Figure 5. Sentinel-1 microwave satellite image of VV polarization after the flood event (15-July-2020).

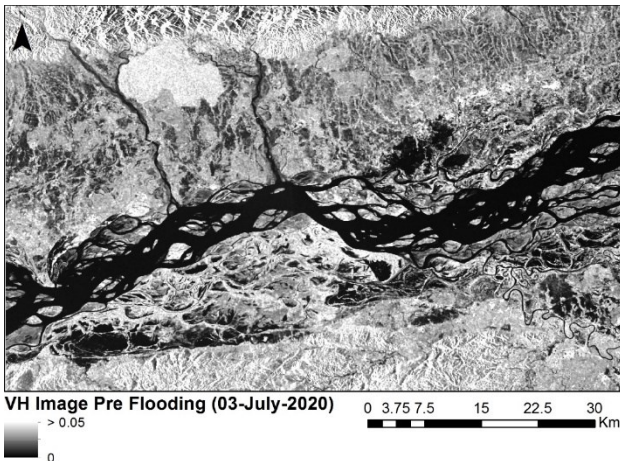


Figure 6. Sentinel-1 microwave satellite image of VH polarization prior to flood event (03-July-2020).

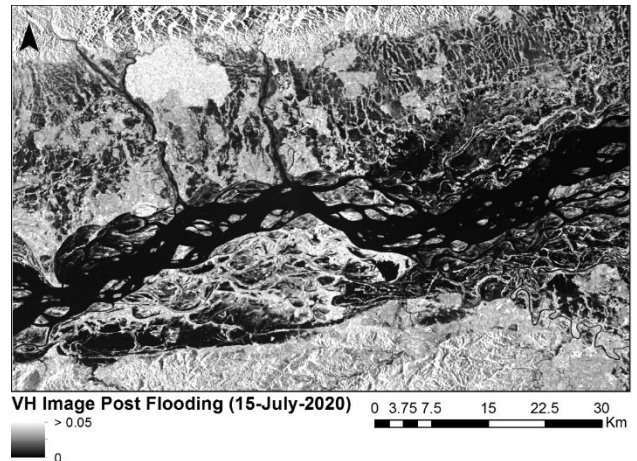


Figure 7. Sentinel-1 microwave satellite image of VH polarization after the flood event (15-July-2020).

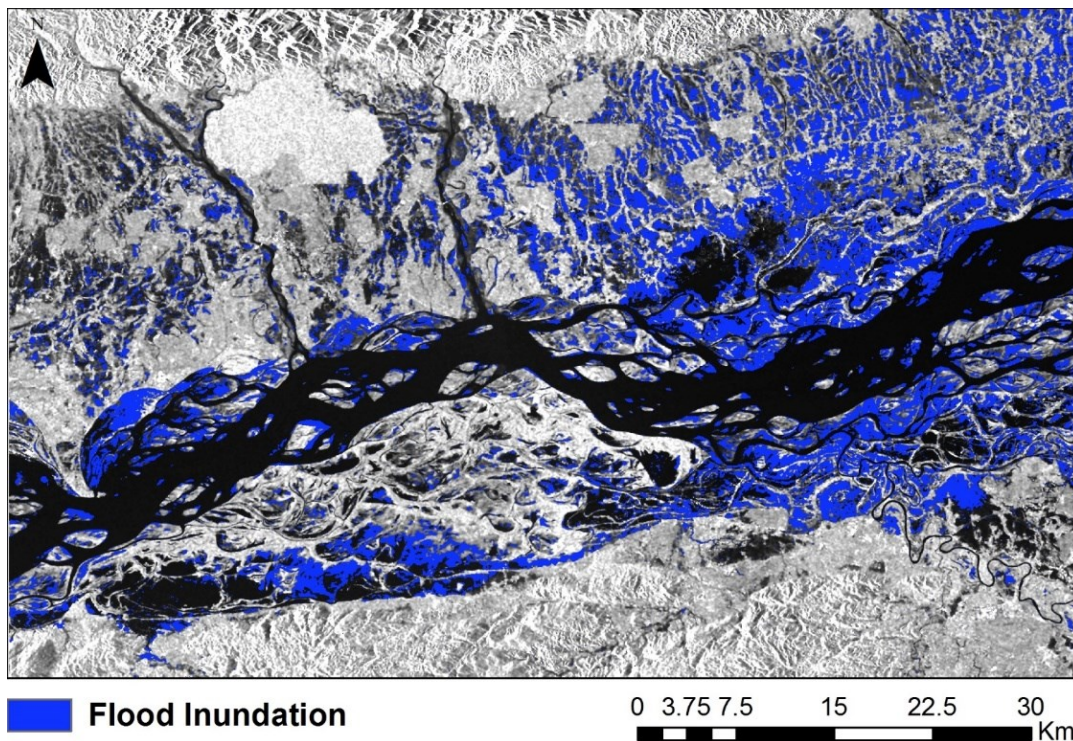


Figure 8. Flood inundation extraction on 15-July-2020 after the flood event in the Brahmaputra River

The cross polarisation (VH) image was found useful in identifying the flood prone region near Kaziranga National Park, Assam, India. The amplitude image of VV polarization was more sensitive towards the surface roughness results in higher return signal. Whereas the VH polarization was found to be better in identifying the water pixels due to lesser return signal from water body. The polarization ratio of VH for pre and post flood event was found to be very effective for identifying the flood inundation due to high flood discharge (Figure 8).

5. Conclusions

Flood discharge estimation using WRF-Hydro model was found to capture the extreme flood event occurred in the month of July 2020. The peak flood discharge during this event was about 50,000 m³/sec and risen rapidly within the span of few days. The rapid rise in flood discharge created widespread floods in the Brahmaputra River and inundated large region of Kaziranga National Park, Assam. Cross polarization microwave SAR images of Sentinel-1 satellite were used in flood inundation mapping. The logarithm of cross polarization amplitude ratio of VH found to be effective technique in extraction of flood inundation region. The flood discharge during the flood event with high discharge (~50,000 m³/sec) simulated through WRF-Hydro model and in-synchronous SAR images were found to be an effective combination for real-time flood assessment and modelling.

Acknowledgements

Authors express their gratitude towards Director Space Applications Centre (ISRO), Ahmedabad. We also extend our thanks to the Deputy Director (EPSA) for encouragement and motivation for this study.

References

- Apurv T., R. Mehrotra, A. Sharma, M. K. Goyal, and S. Dutta (2015). Impact of climate change on floods in the Brahmaputra basin using CMIP5 decadal predictions. *Journal of Hydrology*, 527, 281–291.
- Chembolu V., and S. Dutta (2018). An entropy based morphological variability assessment of a large braided river. *Earth Surface Processes and Landforms*, 43, 2889–2896.
- Dubey A. K., P. Kumar, V. Chembolu, S. Dutta, R. P. Singh, and A. S. Rajawat, (2021). Flood modelling of a large transboundary river using WRF-Hydro and microwave remote sensing. *Journal of Hydrology*, 598, 126391.
- Ghosh S., and S. Dutta (2012). Impact of climate change on flood characteristics in Brahmaputra basin using a macro-scale distributed hydrological model. *Journal of Earth System Science*, 121, 637–657.
- Goswami D.C. (1985). Brahmaputra River, Assam, India: Physiography, basin denudation, and channel aggradation. *Water Resources Research*, 21, 959–978.
- Karmaker T., and S. Dutta (2010). Generation of synthetic seasonal hydrographs for a large river basin. *Journal of Hydrology*, 381, 287–296.
- Karmaker T. and S. Dutta (2011). Erodibility of fine soil from the composite river bank of Brahmaputra in India. *Hydrological Processes*, 25, 104–111.
- Karmaker T., H. Medhi, and S. Dutta (2017). Study of channel instability in the braided Brahmaputra River using satellite imagery. *Current Science* (00113891) 112.
- Khan N.I. and A. Islam (2003). Quantification of erosion patterns in the Brahmaputra–Jamuna River using

- geographical information system and remote sensing techniques. *Hydrological Processes*, 17, 959–966.
- Miller J.D. and M. Hutchins (2017). The impacts of urbanization and climate change on urban flooding and urban water quality: A review of the evidence concerning the United Kingdom. *Journal of Hydrology: Regional Studies*, 12, 345–362.
- Singh V., N. Sharma and C.S.P. Ojha (2004). The Brahmaputra basin water resources. 47. Springer Science & Business Media.
- Sarker M.H., C.R. Thorne, M.N. Aktar, M.R. Ferdous (2014). Morphodynamics of the Brahmaputra–Jamuna River, Bangladesh, *Geomorphology*, 215, 45–59.
- Sarma J. (2005). Fluvial process and morphology of the Brahmaputra River in Assam, India. *Geomorphology*, 70, 226–256.
- Serinaldi F., F. Loecker, C.G. Kilsby and H. Bast (2018). Flood propagation and duration in large river basins: a data-driven analysis for reinsurance purposes. *Natural Hazards*, 94, 71–92.
- Subyani D., A. Daniels, S. Murray, T. Kirsch (2017). The human impact of floods: a historical review of events 1980–2009 and systematic literature review. *PLoS Curr* 5, 1–19.
- Su F., L. Zhang, T. Ou, D. Chen, T. Yao, K. Tong and Y. Qi (2016). Hydrological response to future climate changes for the major upstream river basins in the Tibetan plateau. *Global and Planetary Change*, 136, 82–95.

Rainfall-Runoff relationship for the Lower Tapi Basin

Aditi Rathod^{1*}, Amit Kumar Dubey², Sanskriti Mujumdar¹ and Nirav Agrawal¹

¹ Faculty of Technology and Engineering, The Maharaja Sayajirao University of Baroda, Baroda, India

² Land Hydrology Division (GHCAG/EPISA), Space Applications Centre, (ISRO) Ahmedabad, India

*Email: aditirathod.a@gmail.com

(Received: Sept 14, 2021; in final form: Oct 06, 2021)

Abstract: Floods are key contributors to the massive loss of lives, property, infrastructure, and public services. Due to climate change and accompanying variability, floods have occurred in places that were previously variability, floods have occurred in places that were previously not considered flood-prone. The purpose of the study is to use SWAT to model rainfall-runoff in the lower Tapi basin from Ukai Dam to Surat City. Surat is the city one of most populated which is located at the mouth of the Tapi River. In the years 1998 and 2006, one of the worst floods occurred. The Rainfall-Runoff relationship for the Lower Tapi Basin was established using the Soil and Water Assessment Tool (SWAT). SWAT a physically based distributed parameter can be used to predict runoff, soil effect, and the impact of land management methods on water. The SWAT model was created for the 1998-2017 baseline scenarios. The SWAT model is calibrated and validated using the SWAT-cup. On a daily time scale, the model was calibrated at the Mandvi gauging site. For auto-calibration and validation, the SWAT-CUP SUFI-2 software was employed. The major objective function was the coefficient of determination (R^2), during Calibration and Validation. Model performance was good in daily calibration and validation, with R^2 values of 0.87 and 0.83 respectively. SWAT model was shown to be capable of replicating hydrologic components in the Lower Tapi basin in this study.

Keywords: SWAT Model, SWAT-CUP SUFI-2, Calibration and Validation,

1. Introduction

Floods are by far the most common natural calamity. Flooding is an overflowing of water onto land that is normally dry. Floods affect more than a third of the world's area, affecting around 82 percent of the world's inhabitants (Maxx Dilley et al., 2005). The study region is in the Tapi lower basin, which is downstream of the Ukai dam and leads to Surat city, Surat, where flooding is a natural threat. Surat city had experienced flood in 1998 and 2006. The main reason of flood was a heavy discharge from Ukai dam.

The most important hydrological variable used in water resource studies is runoff. In river basin where there is no gauged station, direct runoff is complicated and tedious. Traditional runoff prediction models necessitate a large amount of meteorological and hydrological data. Many watersheds hydrology models have been developed, but the paucity of spatial data and temporal has hampered their deployment, mostly in poor nations. For estimating high discharge, direct runoff and hydrographs in combination with proper rainfall runoff model Geographical information system (GIS) and remote sensing is an ideal tool. The widespread use of these models has been affected and enhanced by the development of remote sensing techniques and Geographic Information System capabilities.

India is the most diverse country in the world. From culture and tradition, to topography and climate, environment and geography, all has different varieties. Rainfall in different parts of the world varies greatly in strength and distribution. The area's Rainfall-Runoff behavior must be investigated immediately in order to better understand the hydrological phenomena as they change over time and how to affect those changes. Catchment modelling is also essential for estimating various hydrological variables in order to develop effective and safe water structures. For Research hydrologist and Practicing engineers involved in

the development and implementation of integrated water resource system Hydrological modelling is an essential and successful mechanism (Schultz, G.A., 2001).

1.1. SWAT model

a) Introduction to SWAT

The USDA Agricultural Research Service (USDA-ARS) and Texas a&MAgriLite Research collaborated to create SWAT a public domain model. The model allows the user to study long term consequences and is physically based with easy computational efficiency and employs easily available inputs. This model has been developed in early 1990. SWAT model is continuous in its development process with the passage of time to address the various emerging issues in hydrological modelling. During the course of the development of the model, various tools such as, multiple hydrological response units, auto irrigation and fertilization options, nutrition cycling routine, Bacteria transport routine etc. have been added to the model. With the use of this model, water as well as sediment circulation and can be tested and forecasted. Runoff in urban catchments can be estimated using this model. The entire catchment region has been separated into sub-catchments in order to use the model in a real-world setting. Based on the land use, land cover similarities and soil management techniques the sub catchments are separated into minor Hydrological Response Units (HRU). SWAT's hydrologic component is based on land use, land cover and soil management techniques. The following water balance equation is used to calculate the hydrologic component of SWAT:

$$SW_t = SW_o + \sum_{i=1}^n (R_{day} - Q_{surf} - E_a - W_{seep} - Q_{gw}) \quad (1)$$

Where SW_t is the final soil water content (mmH₂O), SW_o is the initial soil water content (mm H₂O), t is time in days,

R_{day} is amount of precipitation on day i (mm H₂O), Q_{surf} is the amount of surface runoff on day i (mm H₂O), E_a is the amount of evapotranspiration on day i (mm H₂O), W_{seep} is the amount of percolation and by pass exiting the soil profile bottom on day i (mm H₂O), Q_{gw} the amount of return flow on day i (mmH₂O) (Jain et al., 2017)

There are two phases to the hydrology of the basin: land phase and routing phase. The land phase describes the entry of water, sediment, pesticides, and other materials into the channel, whereas the routing phase describes the transport of water, sediments, and other materials from the basin through the drainage network of the basin. Daily humidity, solar radiation, temperature, rainfall, wind speed, and other variables are inputs to the SWAT model. To estimate evapotranspiration, various methods such as Priestly-Taylor, Penman Monteith and Hargreaves are used in the models. For obtaining the better estimation and forecasting of water, sediment circulation etc. from the basin, simulation of hydrological cycle integrating overall water circulation the basin is essential.

b) Evaluation of SWAT Model

Model performance evaluation can be done to fulfil the following objectives. i) Quantitative aspect, determining the model ability in representing the historical as well future watershed behaviour ii) To suggest the improvement in modelling approach with the consideration of various factors such as adjustment of model parameters, use of additional information, model structure modification, consideration of important spatial and temporal characteristics of watershed etc.iii) Comparison with the past modelling practices/approaches with the current approach(Jaehak Jeong, 2010).The performance of the model has been assessed using a variety of methods.The model parameters are improved after a simulation run of the SWAT model to match the observed and simulated hydrographs at the outlet(Subhadip Kangsabanik et al., 2017).Optimization is done to minimize a scalar quantity known as objective function. The objective function can be defined by the different methods. Most two approach of performance evaluation used are as

(1) Nash-Sutcliffe efficiency (NSE):

To estimate the efficiency of evaluating the performances of hydrological models, Nash and Sutcliffe developed the following equation:

$$NSE = 1.0 - \frac{\sum_{i=1}^n (o_i^{obs} - p_i^{sim})^2}{\sum_{i=1}^n (O_i^{obs} - O_{i^{mean}})^2} \quad (2)$$

The efficiency NSE proposed by the above equation varies from 1 to $-\infty$. The observed time series data mean value would be a better predictor than the model if the efficiency rating was negative. The above method has a key problem in that it calculates discrepancies between observed and anticipated values on a square basis, which causes larger

values to be inflated and smaller values to be ignored. As a result of this impact, model performance is overestimated during peak flow and underestimated during lean flow. This model efficiency is not more sensitive for systematic model over or under predictions during lean periods.

(2) Coefficient of Determination(R²):

R² is a coefficient that runs from 0 to 1, and it explains the observed dispersion from the values that were simulated. There is no correlation if the value is 0, whereas a value of 1 denotes that the observed and expected values are perfectly correlated (Nina Omani et al., 2007).Major drawback of this method for defining model efficiency is that it only quantifies the dispersion. A model with that systematically over or under predicts all the time may have good correlation even the predictions are wrong.

1.2. Objectives

The study's major goal is to use the Soil and Water Assessment Tool model to investigate the Rainfall-Runoff behaviour of the Lower Tapi basin. To model the discharge using SWAT-CUPs (SWAT-Calibration uncertainty programmes), which employ the sequential uncertainty fitting (SUFI-2) algorithm.

2. Study Area

The Tapi River is the Peninsula's second-largest westward-flowing interstate waterway. It starts in the Multai forest reserve in Madhya Pradesh's Betul district, at an elevation of 752 meters. The river's overall length from source to outfall into the Arabian Sea stretches over 724 kilometers, with the first 282 kilometers flowing through Madhya Pradesh and 54 km forming the state's common border with Maharashtra. It flows across Maharashtra for 228 kilometers before entering Gujarat. The Tapi River flows across Gujarat for 214 kilometers before joining the Arabian Sea at the Gulf of Cambay after passing through Surat.

The Tapi basin is divided into three sub-basins: the Upper Basin (29,430 sq. km) up to the Hatnur confluence of the Purna with the main Tapi, the Middle Tapi Basin (25,320 sq. km) from Hatnur to the Gidhade gauging site, and the Lower Tapi Basin (25,320 sq. km) from the Gidhade gauging site up to the sea (10,395 sq. km). The Lower Tapi basin had maximum rainfall is 1427.45mm while minimum annual rainfall is recorded in year of 1991 is 578.94mm (CWC, March, 2014). The Lower Tapi Basin spans a large region of 4108.90 Sq. km (CWC, March, 2014).

Surat is located in the Lower Tapi Basin, (Figure 1) which runs between the Ukai Dam and the Arabian Sea. One of the worst floods in Surat's history occurred in the years 1998 and 2006. The flood of 2006 is remembered as a huge occurrence that caused a calamity, resulting in the mass demolition of properties worth INR 20 billion.

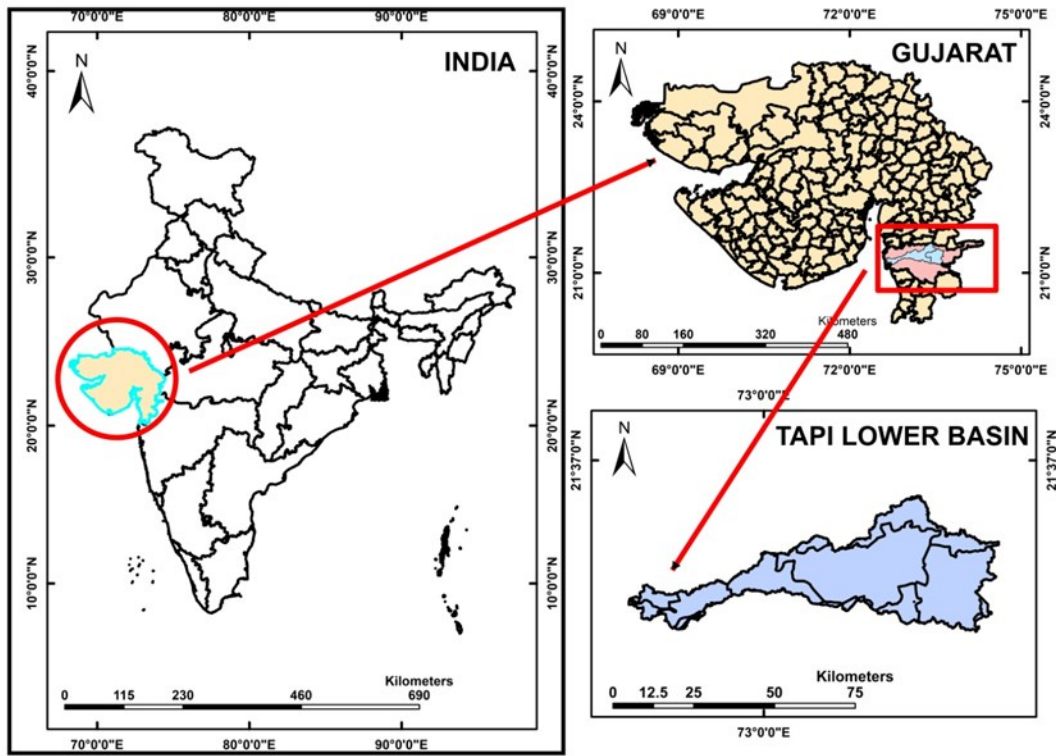


Figure 1. Location Map of Lower Tapi basin

3. Methodology

A high number of geographical and temporal inputs are required by the SWAT. SWAT, as a model that is spread in a semi-distributed manner, must use GIS technologies to process, aggregate, and evaluate this data spatially. As a result, the model was integrated with ArcSWAT for ArcGIS is a free supplement plugin that makes ArcGIS easier to use. The flow chart Figure 2 depicts the SWAT at the basin’s outlet; a methodology for runoff modelling has been developed.

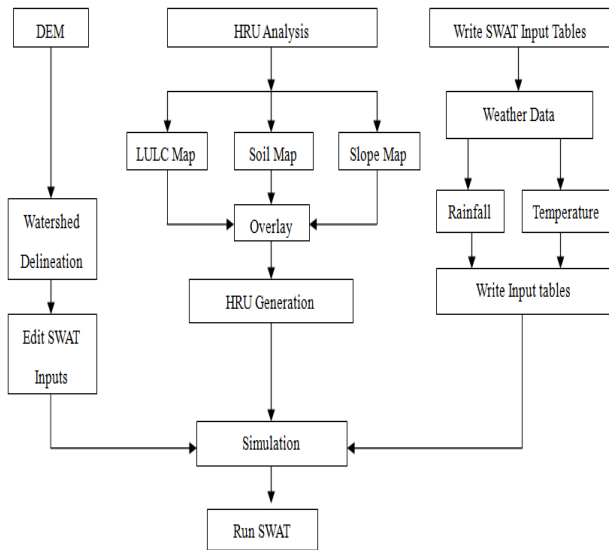


Figure 2. Rainfall-Runoff Modelling Methodology

3.1. Digital Elevation Model (DEM)

A digital elevation model (DEM) is a three-dimensional depiction surface of a terrain derived from elevation data. A digital elevation model (DEM) is a digital depiction of the elevation of the land surface in relation to any reference datum. DEM was taken from the Bhuvan ISRO website. The DEM image has a resolution of 30x30 metres. The DEM is used to define the stream network, longest reaches, and drainage surfaces of the watershed and sub-basins. The DEM was also used to derive channel slope, terrain slope, and reach length are all topographic factors. Figure 3 shows the Digital Elevation Model for Lower Tapi basin.

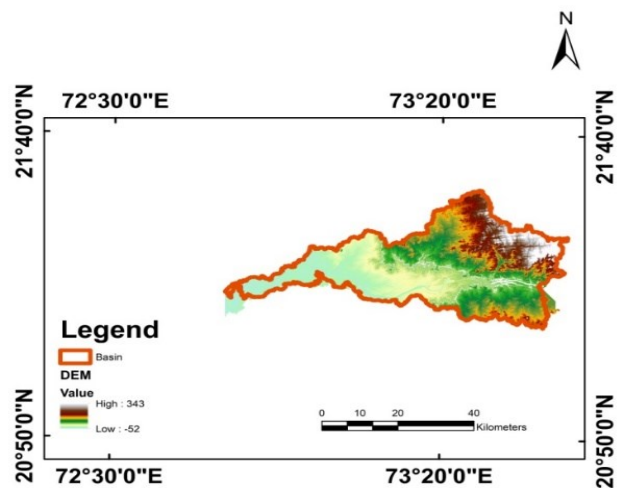


Figure 3. Digital Elevation Model

3.2. Landuse/Landcover classification

The LANDSAT 8 Image was used to create the Landuse data (acquired on December 2020). The data was obtained from the USGS Archive. There are seven bands in the

downloaded file. Then, this picture is projected into correct projection using ArcGIS, same as the DEM with the same datum. For image classification the supervised classification technique is use by recognising distinct signatures found in the Tapi lower basin and then to make it compatible with ArcSWAT the image was converted to grid format in ArcGIS. Water, pasture, Agricultural Land- Generic, Mixed Forest, and Residential are among the major classifications. Figure 4 depicts the land use map of the Tapi lower basin, while Table 1 shows the area covered by various land use types.

Table 1. LULC classes in Tapi Basin

SWAT Code	Land use description	Area (ha)	Watershed Area (%)
WATR	Water	3747.4348	2.31
PAST	Pasture	52743.0246	32.52
AGRL	Agricultural Land- Generic	64231.9705	39.60
FRST	Mixed Forest	38126.2247	23.50
URBN	Residential	3347.6122	2.06
	Total	162196.2668	100

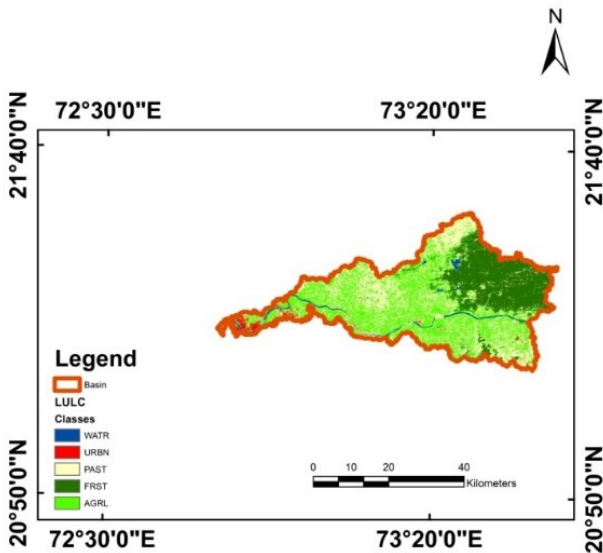


Figure 4. Land Use Map

3.3. Map of the soil

The Food and Agriculture Organization of the United Nations (FAO/UNESCO) provided a soil map with a geographical resolution of 1:50,000, 000.00. The soil data from the Tapi Lower Basin has been separated into three groups. Clay loam, loam, and clay are the textures of the soils. Figure 5 depicts a soil map of the Tapi lower basin.

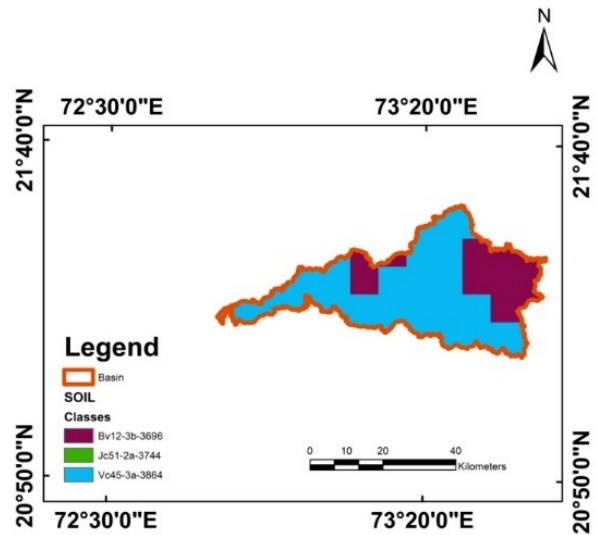


Figure 5. Soil Map

3.4 Hydro meteorological data

For the modelling of numerous physical processes, SWAT requires daily values for solar radiation, relative humidity, precipitation, wind speed, and maximum and minimum temperature. The daily Maximum Temperature, Minimum Temperature and Rainfall data for Lower Tapi basin were provided by State Water Data Centre (SWDC). From 1998 to 2017, 20 years of daily rainfall data and 20 years of daily maximum and minimum temperature data were used in this study area. Figure 6 shows the delineation of sub-basin of Lower Tapi basin.

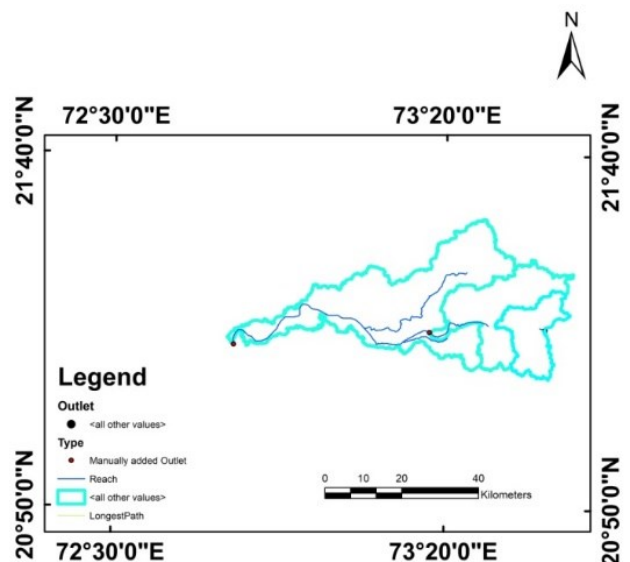


Figure 6. Delineation of sub-basin of Lower Tapi basin

4. Model setup

The SWAT model's whole database has been produced, and the model has been set up for the research area. Using a DEM-based automatic technique, ArcSWAT2012 enables us to define sub-watersheds. The model includes a DEM file. The catchment area's outlet was identified, for the purposes of this investigation, the watershed was

defined (Figure 5), and all of the parameters for each subbasin, and calculations were made. The catchment's total size is estimated to be 1621.9627 km². The research area's minimum and greatest elevations are -50 and 342 metres, respectively. There are three sub-basins in the watershed.

We may import a land use and soil map, assess slope characteristics, and calculate land HRUs for each sub-watershed using SWAT. The land use category identifies the land use layer for each category, and the soil look up table specifies the type of soil to be represented.

The database was classed into three hydrological soil groups (HSGs): Clay Loam, Clay and Loam, and Clay and Loam. The LULC map has been reorganised into five categories. The slope map has been categorised into three categories: 0 – 10%, 10% – 20%, and 20% – 99%. The land use, soil, and slope data layers were then superimposed. Hydrologic response units (HRUs) have been distributed throughout the basin. A total of 29 HRUs were developed in the Lower Tapi basin. To exclude minor land use, soil, and slope, a 10% threshold has been developed for all land use, soil, and slope classes.

Daily precipitation and temperature data are required by the model. Weather station locations can be loaded into the current project and weather data can be assigned to sub-watersheds using SWAT. Daily precipitation data as well as daily maximum and minimum temperature data from 8 rain gauge sites was used from the same years.

The ArcSWAT toolbar's 'Write Input Tables' menu is used to load weather data. This tool enables the users to add weather station sites to their current project and allocate weather data to sub-watersheds. For every kind of meteorological data loaded, one gauge is linked by each sub-watershed. The initial watershed input parameters must be defined before SWAT can be executed. These numbers are derived from defaults or automatically determined depending on the watershed demarcation and land use/soil/slope characteristics. The model was then used to simulate surface runoff.

To achieve the study's goal, the SWAT2012/Arc 2012.10.24 interface was used. SWAT-CUP is a free computer application that can be used for sensitivity analysis, calibration, and validation.

An interface's primary purpose is to connect the input or output of a calibration software and model. Using trial-and-error method Auto calibration and validation were carried out, which required fewer model runs to get the best possible simulation that was closer to the actual values (Davy Sao et al., 2020).

5. Analysis and discussion of results

For the calibration, validation and estimation of the uncertainty of the SWAT model, SWAT-CUP a free software tool is used. The software prefers MCMC SUFI2, GLUE, ParaSol, and PSO procedures. The data was loaded from a SWAT Model text input file, and the SWAT CUP software's SUFI2 algorithm was used to do auto calibration

and validation. SWAT-CUP SUFI2 is a calibration and validation software used in hydrological studies and investigation, (Kh. Gorgij, A. Dehvari and M. R. Dahmardeh, 2020). For multi-site and multivariable analysis SUFI2 can be used. The present study and analysis have been done on daily time steps.

The first three years of observed data (1998-2000) were used to warm up the model, and then data from 2001 to 2010 were used to calibrate the model's parameters, with the performance of the calibrated model being evaluated using data from 2011 to 2017. The SUFI-2 iterative procedure will narrow the parameters value after each iteration phase. The simulation in the iteration process was set to 500. The number of iterations can be determined once the statistical coefficient is calculated; the best simulation with the best statistical coefficient result can be displayed. Uncertainties in factors such as the driving variable, the conceptual model, the parameters, and the observed data (Abbaspour et al., 2007). In addition to the Coefficient of correlation (R²), Nash-Sutcliffe Efficiency (NSE), and RMSE standard deviation ratio, the P-factor and r-factor are employed to know the strength of calibration and uncertainty measurements (RSR) (Abbaspour et al., 2007). The p-factor must be close to 1 and the r-factor should be close to 0 in ideal conditions. When the values of p-factor and r-factor approach acceptable levels, the parameter uncertainties are within the required parameter ranges. The most common error index metric is the root mean square error (RMSE). Equation (3) can be used to determine RSR.

$$RSR = \frac{\sqrt{\sum_{i=1}^n (O_i^{obs} - P_i^{sim})^2}}{\sqrt{\sum_{i=1}^n (O_i^{obs} - P_i^{mean})^2}} \quad (3)$$

The coefficient of determination was used as the second assessment criterion (R²). The main objective function was R². The equation number (4) is used to calculate R².

$$R^2 = \frac{|\sum_{i=1}^n (Q_i^{sim} - \bar{Q}_i^{sim})(Q_i^{obs} - \bar{Q}_i^{obs})|^2}{\sum_{i=1}^n (Q_i^{sim} - \bar{Q}_i^{sim})^2 \sum_{i=1}^n (Q_i^{obs} - \bar{Q}_i^{obs})^2} \quad (4)$$

Where Q_i^{sim} and Q_i^{obs} represent simulated and observed values and \bar{Q}_i^{sim} and \bar{Q}_i^{obs} show mean simulated and mean observed values.

The Nash-Sutcliffe efficiency criterion was used as the third evaluation criterion (NSE). NSE could be computed using the equation (5)

$$NSE = 1.0 - \frac{\sum_{i=1}^n (O_i^{obs} - P_i^{sim})^2}{\sum_{i=1}^n (O_i^{obs} - O_i^{mean})^2} \quad (5)$$

Table 2. Performance Ratings for Statistical Parameters

Indices	R ²	NSE	RSR
Range	0 to 1	-∞ to 1	0 to ∞
Optimal Value	1	1	0
Satisfactory Value	>0.5	>0.5	≤0.7

SWAT model calibration and validation

In SWAT model, to reduce the discrepancy between the observed and simulated daily, monthly and yearly stream flow, as well as to correspond anticipated values with an acceptable degree of fit, model calibration was performed (A. van Griensven et al., 2005).

The model's parameters were calibrated using observed data from 2001 to 2010, with the most sensitive parameters, such as the SCS runoff curve number (CN2.mgt), base flow alpha factor (ALPHA BF), groundwater delay factor (GW DELAY.gw), and threshold water depth in shallow aquifer required for return to occur, being adjusted (GWQMN.gw).

The ability of a model to mimic hydrological activity in the study area is determined by comparing model simulated values to observed values (Haan et al., 1982). To simulate daily flow data, the SUFI-2 algorithm's SWAT-CUP software was utilized for auto calibration and validation. The SWAT CUP software's SUFI2 algorithm produces visual comparisons as well as statistical criteria such as coefficient of determination (R²), Nash-Sutcliffe Efficiency (NSE) and RMSE- observations standard deviation ratio (RSR).

The overall qualitative visual match, like peak matching, overall agreement in hydrograph characteristics and recession tendencies are shown by Visual comparison.

Figures 7 and 8 exhibit graphs of observed and model computed runoff for the daily calibration and validation periods, respectively. Few high peaks are underestimated, as seen in the images, and in many cases, there is a distinct difference between observed and simulated flow. The model anticipates high runoff, which is progressively retreating when there is persistent heavy rainfall, indicated by brown circle in Figure 8. This indicates that basin characteristics such as slope play an important role in achieving a hydrological response (82.15 percent area coverage for slopes ranging from 0 to 10%). The red circle indicated the computation of high runoff with high rainfall.

Figure 9 and 10 exhibits correlation graphs between observed and simulated data. For the calibration and validation periods, the R² values were 0.87 and 0.83, respectively, revealing a very excellent correlation between observed and simulated streamflow data.

Table 3 shows the results of statistical evaluation criteria used to check model performance for daily periods. Based on the performance ratings listed in Table 2, the model's performance can be rated as very good, as shown in these tables.

Table 3. Daily calibration and validation statistical model results

Statistical Parameter	R ²	NSE	RSR
Calibration (year 2001-2010)	0.87	0.86	0.37
Validation (year 2011-2017)	0.83	0.82	0.43

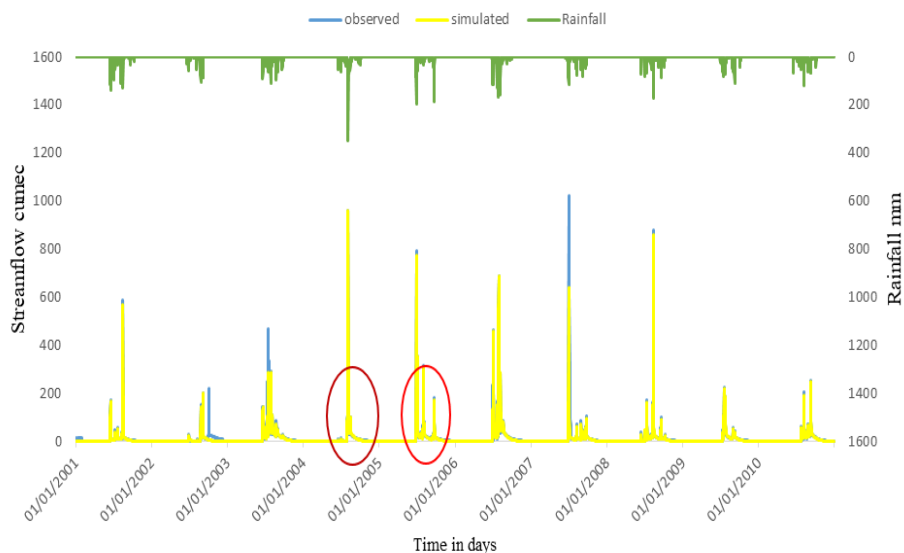


Figure 7. Daily Calibration from 2001 to 2010

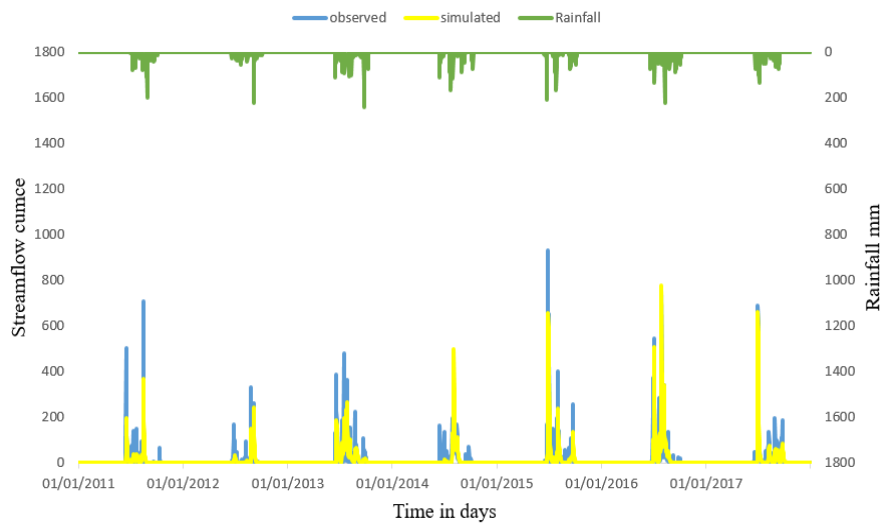


Figure 8. Daily Validation from 2011 to 2017

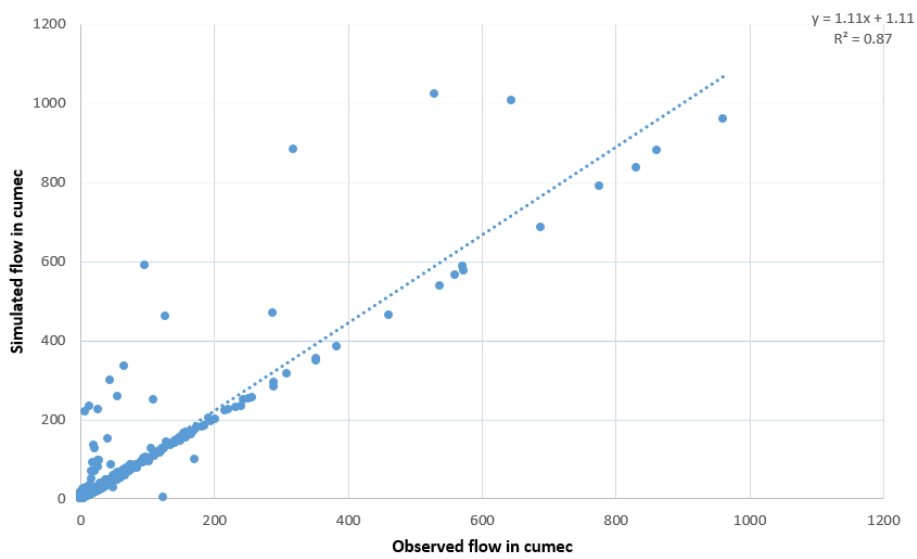


Figure 9. Correlation performance of calibration

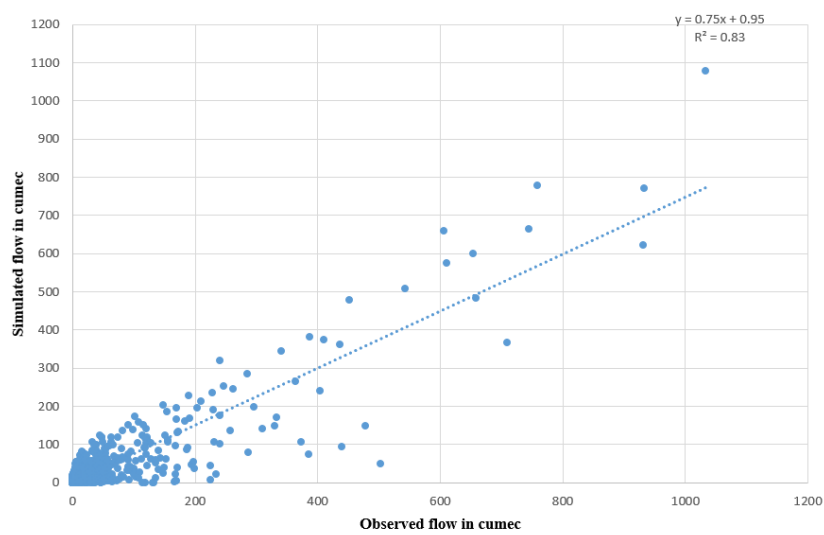


Figure 10. Correlation performance of validation

6. Conclusions

Observed stream flow data were used to calibrate and validate the SWAT model. During the Lower Tapi basin's calibration and validation periods, the SWAT model worked admirably. For calibration and validation, twenty-year discharge data is separated into two equal halves. From 1998 to 2010, the flow was auto-calibrated using daily observed and simulated flows. Validation of flows from 2011 to 2017 is carried out. The calibration result revealed that the calibrated and observed daily flows are in good agreement ($R^2=0.87$, $NSE=0.86$, $RSR=0.37$). For validation, the R^2 is 0.83, the NSE is 0.82, and the RSR is 0.43.

References

- Harka A. E., N. T. Roba and A. K. Kassa (2020). Modelling rainfall runoff for identification of suitable water harvesting sites in Dawe River watershed, Wabe Shebelle River basin Ethiopia, *Journal of Water and Land Development*, 187-195.
- Griensven A. V., T. Mexiner, S.Grunwald, T.Bishop, M.Diluzio and R.Srinivasan (2005). A global sensitivity analysis tool for the parameters of multi-variable catchment models, *Journal of Hydrology*, 10-23.
- Yaduvanshi A., R. K. Sharma, S. C. Kar and A. K. Sinha (2017). Rainfall–runoff simulations of extreme monsoon rainfall events in a tropical river basin of India, *Nat Hazards*, 90, 844-861.
- CWC (2014). Annual report of central water commission.
- Kuhn C. (2014). Modeling rainfall-runoff using SWAT in a small urban wetland, *FES 724 Watershed Cycles and Processes | spring 2014*, 1-19.
- Schultz G. A. (2001). Integrated Hydrologic Modeling and GIS in Water Resources Management, *Journal of Computing in Civil Engineering*, 217-223.
- Jeong J., N. Kannan, J. Arnold, R. Glick, L. Gosselink and R. Srinivasan (2010). Development and Integration of Sub-hourly Rainfall–Runoff Modeling Capability within a Watershed Model, *Water Resource Manage* 24, 4506-4527.
- Abbaspour K. C., J. Yang, I. Maximov, R. Siber, K. Bogner, J. Mieleitner, J. Zobrist, R. Srinivasan (2007). Modelling hydrology and water quality in the pre-alpine/alpine Thur watershed using SWAT, *Journal of Hydrology*, 333, 413–430.
- Gorgij K., A. Dehvari and M. R. Dahmardeh (2020). Uncertainty Analysis of Hydrological Parameters in the Sarbaz Watershed Using the SWAT Model and the SUFI-2 Algorithm, *Journal of Hydrosociences and Environment*, ISSN: 2345-5608, 43-56.
- Sao D., Tasuku K., L. H. Tu, P. Thouk, A. Fitriyah and C. Oeurng (2020). Evaluation of Different Objective Functions Used in the SUFI-2 Calibration Process of SWAT-CUP on Water Balance Analysis: A Case Study of the Pursat River Basin, Cambodia, *Water*, 1-22.
- Dilley M. (2005). Natural Disaster Hotspots a Global Risk Analysis, The World Bank Hazard Management Unit, 1-132.
- Omani N., M. Tajrishy and A. Abrishamchi (2007). Modeling of a River Basin Using SWAT Model and GIS, *Riverside Kuching, Sarawak, Malaysia*, 510-517.
- Shanbor K. and M. Jain, (2017). Rainfall-Runoff Modeling of a River Basin using SWAT Model, *International Journal of Engineering Research & Technology (IJERT)*, ISSN: 2278-0181, 6(12), 293-302.
- Kangsabanik S. and S. Murmu (2017). Rainfall-runoff modelling of Ajay River catchment using SWAT model, *IOP Conference Series: Earth and Environmental Science*, 67, 7th International Conference on Environment and Industrial Innovation, Malaysia, 24-26 April 2017.
- Shivhare V., M. K. Goel and C. K. Singh (2014). Simulation of Surface Runoff for Upper Tapi Sub catchment area (burhanpur watershed) using SWATS, *The International Archives of the Photogrammetry, Remote Sensing and Spatial Information Sciences*, Volume XL-8, 391-397.
- Tejaswini V. and K.K. Sathian (2017). Calibration and Validation of Swat Model for Kunthipuzha Basin Using SUFI-2 Algorithm, *International Journal of Current Microbiology and Applied Sciences* ISSN: 2319-7706 7, 2162-2172.

Coupled Model for Flood Prone Lower Tapi River Basin Integrating Satellite Inputs

Swati S. Patel^{1*} and Praveen.K. Gupta²

¹Kalol Institute of Technology and Research Centre, Kalol, 382721, India

²Space Applications Centre (ISRO), Ahmedabad, 380015, India

*Email: swatipatel191993@yahoo.com

(Received: Sept 16, 2021; in final form: Oct 6, 2021)

Abstract: Coupled hydrological-hydraulic model is very important and needs to be considered for water resources planning and management. Most of the work has been done on either hydrological aspect or hydraulic behaviour separately using mathematical models. This research work aims to develop and test an integrated modelling system coupling hydrological and hydraulic processes in the lower Tapi basin that incorporates mainstream from Ukai reservoir to the Gulf of Cambay while the length of the Lower Tapi River Basin in Tapi River is estimated as 127 km. The MIKE SHE model is a deterministic fully distributed and physically based hydrological modelling tool has been integrated with MIKE 11, which is a 1D river simulation model. The model also uses a network of regular grids to discretize the horizontal plane of a watershed, and represent the spatial variability of the hydrological process. Coupled MIKE SHE and MIKE 11 model has been parameterized integrating the remote sensing derived hydro-meteorological and biophysical variables to simulate the hydrological water balance and river flows. Model has been calibrated using the satellite altimeter derived and simulated river water levels. Model calibration was satisfactory with coefficient of determination (R^2) 0.97. Tested integrated model simulations were carried out to simulate the evapotranspiration, surface runoff, soil moisture, and stream flows. Major water balance components such as actual evapotranspiration and Surface Runoff were obtained 50.2% and 39.7%, respectively. Further, ET was partitioned into evaporation and transpiration, which were of 37.2% and 62.8%, respectively. Calibrated integrated model would be useful for long-term hydrological simulations for planning and management of water resources in the region.

Keywords: coupled model, MIKESHE, MIKE11, hydrological water balance, river flow simulation

1. Introduction

In order to utilize available water resources efficiently, we need to develop strategies that are based on the thorough study of hydrological balance and its complex nature along with river flows. Therefore, an integrated model needs to be developed to study the 2-D overland flow in the basin as well as river flow simulations. Certain constraints in this model must be accentuated, as well as simulated results should be validated for the given period in terms of observed hydrological parameters. This calibration will allow us to understand the hydrological-hydraulic interactions more efficiently and thoroughly (Zhiqiang et al. 2008). Coupling of hydrological and hydraulic processes enable the simulation of river flow along with hydrological water balance (Clilverd et al., 2016).

Most of the research work carried out independently either on hydrological aspect or hydraulic behaviour using mathematical models. The present research work aims to develop and test an integrated modelling system (coupling hydrological and hydraulic processes) in the lower Tapi basin with satellite data integration. Coupling of both MIKE SHE and MIKE 11 have been used to simulate the hydrological water balance and river flows (Mirela-Alina and Ana, 2015; Clilverd et al., 2016). Integrated model simulations were carried out to quantify water fluxes such as AET, overland flow, soil moisture, stream flows etc. in the Lower Tapi river Basin chosen as study area (Saidislomkhon et al. 2016).

2. Study area and data

Study area for the purpose of this research work is the lower Tapi river basin that incorporates mainstream from Ukai Reservoir to the Gulf of Cambay (Figure 1). The length of the Lower Tapi River is calculated as 127km. Ghala gauging site is considered taking into account availability of satellite altimeter data. Climatic aspects of Ghala are considered to represent the entire lower Tapi Zone. There exists a forest area of 2428 square km in the basin. The coastal plains in Gujarat are composed of alluvial soil with a layer of black soil on the surface. There are few satellite altimeter (SARAL-Altika) tracks for water level estimations and shown in Figure 2.

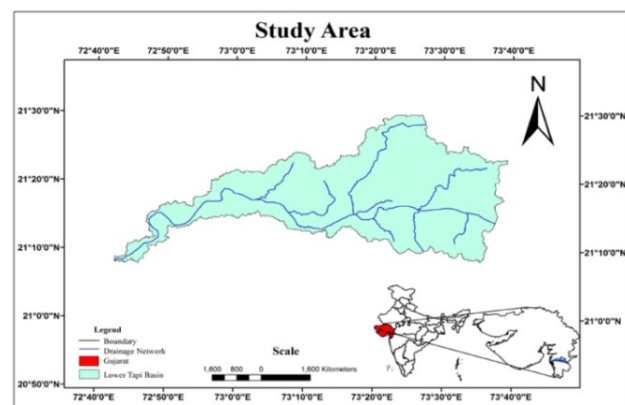


Figure 1. Location of lower Tapi river basin

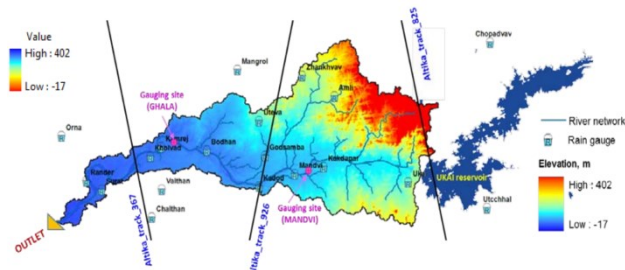


Figure 2. Lower Tapi basin along with altimeter passes and drainage network

List of datasets used for the parametrization of coupled hydrological-hydraulic model, hereafter “coupled model” is presented in Table 1 along with their sources.

Table 1. List of datasets used in the study

Sr. No.	Data	Source
1	DEM	Satellite: SRTM (30 m)
2	LULC	Satellite: AWiFS (Resouresat-2)
3	Soil	NSBSS_LUP
4	Rainfall	NOAA CPC
5	PET (Potential Evapotranspiration)	MODIS PET
6	LAI (Leaf Area Index)	MODIS 4-day composite
7	River cross sections	CWC Tapi division Surat
8	Strickler’s roughness (M)	From literature and using LULC (Subramanya,
9	Study area boundary	Delineated using DEM
10	Drainage network	Delineated using DEM
11	Ukai releases	Ukai Division No.1, Ukai
12	Water level for nearby Ghala	SARAL-ALTIKA

3. Methodology

Present study aims for the simulation of water balance and river flows using coupled model in integrated fashion using remote sensing derived hydrological and bio-physical parameters. Coupled model with MIKESHE (DHI, 2007a and 2007b) and MIKE 11 (DHI, 2007) for water balance and river flow simulations has been used. Approach used in this study is presented in Figure 3. All the hydrological inputs (remote sensing, in situ, ancillary data) have been prepared in the GIS environment and transformed into the model pre-defined formats using the GIS-model interfaces. These model inputs have been used for the parameterization of integrated model. Model calibration and validation (DHI, 2007c) have been carried out by comparing the observed/measured water levels with the simulated results through the adjustment of model control parameters such as Strickler’s roughness and soil hydraulic conductivities. Simulated results have been analysed to estimate the various water balance components in the lower Tapi basin.

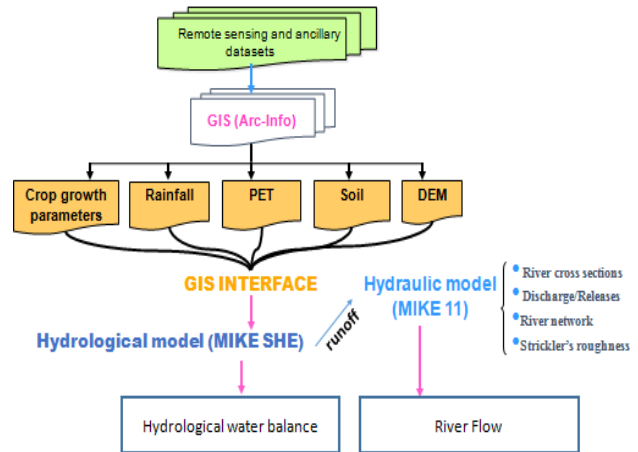


Figure 3. Schematic outline of the coupled model

3.1. MIKE SHE/ MIKE 11 Parameterization

Remote sensing based hydro-meteorological parameters and other ancillary data used in the coupled modelling are presented in the subsequent section.

a) Digital Elevation Model (DEM) (Topography)

Topography is defined by a DEM that describes the elevation of any point in a given area at a specific spatial resolution. In this study, 30m resolution SRTM (Shuttle Radar Topography Mission) DEM of 30m resolution is considered. Maximum elevation in the basin goes upto 386 m whereas minimum value observed to -20 m. Average topography in the basin is 78.1 m with standard deviation of 69.2 m. Figure 4 presents topographical variations in the study area.

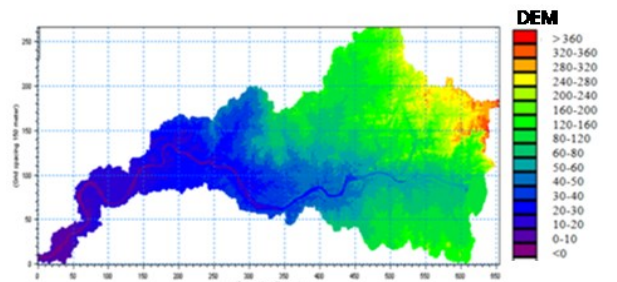


Figure 4. DEM of the study srea

b) Potential Evapotranspiration (PET)

Global potential evapotranspiration product (MOD16) from MODIS is downloaded from Goddard Spcae Flight Centre of NASA. PET is available with 8 day composite and spatial resolution of 1 km. Potential evapotranspiration for a particular day is shown in Figure 5.

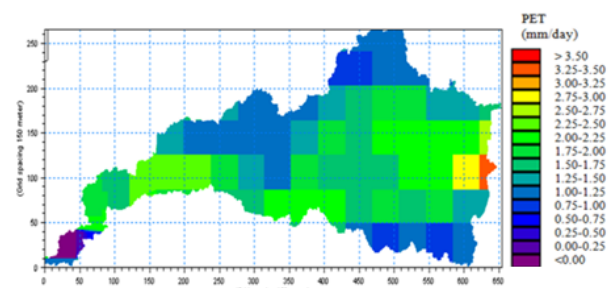


Figure 5. PET for a particular day

c) Precipitation (Rain)

Multi-sensors along with model based rainfall product of climate prediction centre of NOAA is used in the present study. Data is available with daily temporal and 10 km spatial resolutions. Rainfall variations for a particular day is presented in Figure 6.

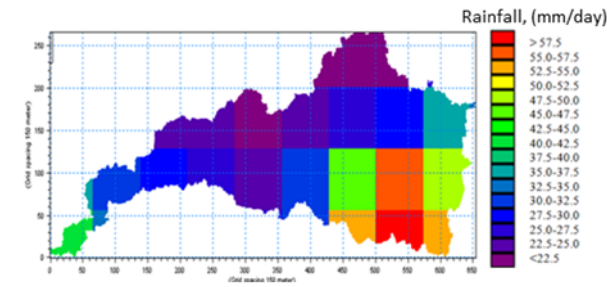


Figure 6. Precipitation for a particular day

3.1.2 Other data used in the study are as follows:

a) Soil

Soil data from National Bureau of Soil Survey and Land Use Planning (NBSS&LUP) is used in the study. There four major soil types in the study area which includes sandy loam (23.7%), loam (16.4%), silty (34.3%) and clayey soils (25.6%). Spatial variability of soil types is present in Figure 7.

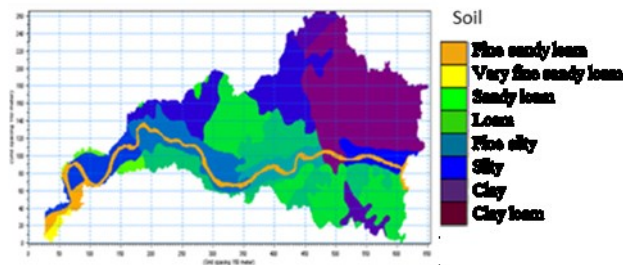


Figure 7. Soil type Map in the study area

b) Land Use Land Cover (LULC)

Advanced Wide Field Sensor (AWiFS) data of Resourcesat-2 is used to classify land cover classes in the study basin. unsupervised classifier ISO data is used for the land cover classifications. Total 6 major land cover classes obtained in the basin and these are water bodies (17.7%), forest (14.8%), agriculture (43.7%), built-up (2.5%) and scrub lands (21.3%). These land cover classes have been used to estimate Strickler’s coefficient, which is reciprocal of Mannings, roughness coefficients.

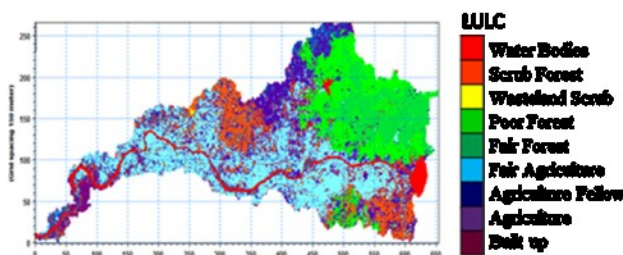


Figure 8. LULC class map in the study area

c) Strickler’s coefficient (M)

Initial values of the Strickler’s coefficient (M) are assigned based on the land cover classes which are estimated using remote sensing data. Value of M varies from 18-45 in the basin. Mean value of the M in the study area is 30.1 with standard deviation of 7.5. Strickler’s coefficient is a model control parameter for the model calibration. Strickler’s coefficient variation in the study area is presented in Figure 9.

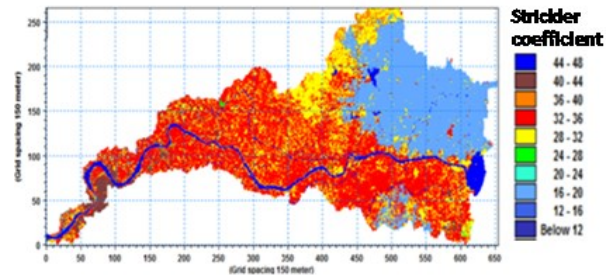


Figure 9. Strickler’s coefficient variation in the study area

3.2. River data

3.2.1. River Network

Pre-processing of the DEM is one of the important steps needed to be carried out as a first step in automatic extraction of drainage networks and delineation of basin. Therefore, a hydrologically corrected DEM was prepared and after that based on flow direction matrix and flow accumulations an ordered drainage network was delineated. Subsequently, drainage network was imported to the MIKE-11 model environment. Driange network used in the MIKE-11 model is presented in Figure 10. Red dots are representing locations where cross sections have been defined in the model along the river.

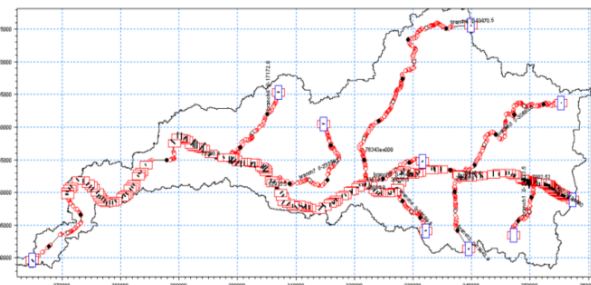


Figure 10. Longitudinal profile of river network as input of MIKE11

3.2.2. Cross Sections

Cross sections data of lower Tapi river basin are collected from the Central Water Commission (CWC) office, Tapi division Surat. A total of 250 plus cross sections data covering major variations along the entire river are collected. Figure 11 illustrate the cross sectional variation of the river from upstream to downstream locations. Depth of river bed varies approximately from 4 m to 30 m along the river from upstream to downstream.

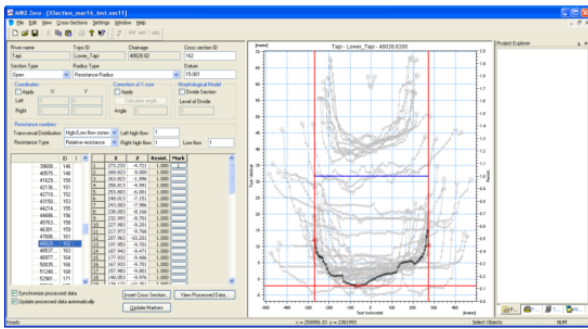


Figure 11. Major cross sections from Upstream to Downstream of the Lower Tapi River Section.

4. Results and discussion

Coupled model, integrated with remote sensing derived hydro-meteorological products, simulations have been carried out for the monsoon season of the year 2013. model simulated results during the study period have been analysed in the spatial and time domain. Analysis of results is presented in the following section.

MIKE SHE Simulated Results

Major water balance components such as Actual Evapotranspiration (AET) and surface runoff are found to be 50.2% and 39.7% of total rainfall, respectively. Fraction of evaporation and transpiration obtained are 37.2% and 62.8% respectively of total evapotranspiration. The following overall water balance estimates are obtained for lower Tapi river basin and shown in Table 2.

Table 2. Total water Balance of lower Tapi basin

Parameters	Values(mm)
Precipitation	1905.0
Evapotranspiration	957.0
-Evaporation	356.0
-Transpiration	601.0
Soil moisture change	185.0
Runoff	756.0

Spatial Domain Results: Different components of the water balance are extracted from MIKE SHE in spatial domain and presented in Figures 12-18.

1. Average water content (monsoon season average) in the root zone (soil Moisture)

An average soil moisture map of the basin was prepared by aggregating the daily maps during the monsoon season of 2013. It may be observed that along the river network and in the downstream regions soil moisture is high as compared to regions or flood plains which are away from the river/stream sections. This is because of accumulation of surface runoff in the streams and subsequently in the main river system. In the upstream area especially in the southern region, average soil moisture found to be slightly low. Result of average water content in the root zone is presented in Figure 12.

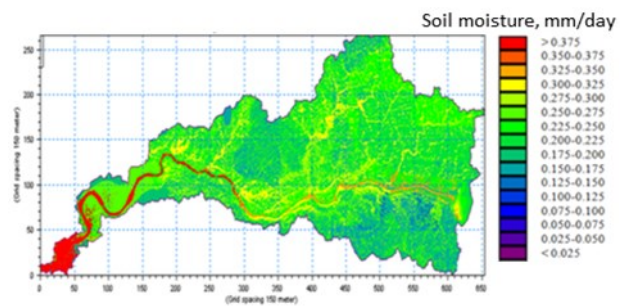


Figure 12. Result of average water content in the root zone

2. Actual Evapotranspiration (AET)

Actual evapotranspiration (AET) is summation of evaporation and transpiration losses in a particular location. Mean AET in the basin is 4.1 mm with standard deviation of 0.73 mm. Results of AET is presented in Figure 13.

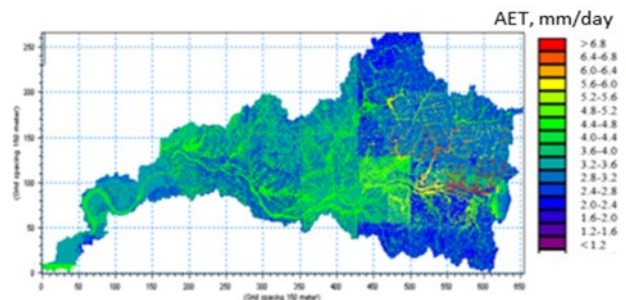


Figure 13. Result of actual evapotranspiration

3. Actual Transpiration

Actual transpiration is mainly contributed by the vegetation and similar trend is observed in the basin. Agriculture and forest regions are showing high transpiration losses and it is very low in the river/streams and other water bodies. Small amount of transpiration from water bodies is due to presence of aquatic vegetation. Mean value of transpiration is 2.1 mm with standard deviation (SD) of 1.2 mm in the basin. Results of actual transpiration is presented in Figure 14.

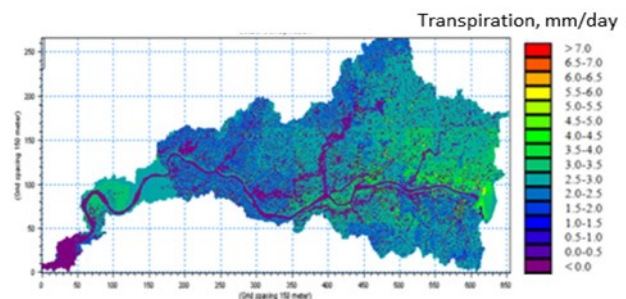


Figure 14. Result of actual transpiration

4. Actual Evaporation from Pondered Water

Evaporation is mainly occurring in open water bodies and from the fields which are having soil moisture but very less vegetation. It can be remarked that all the river/stream network along with other water bodies are showing high evaporation whereas it is quite low in other land cover

classes. Result of actual evaporation from ponded water and other land cover classes is presented in Figure 15. Mean of evaporation is 1 mm with SD of 1.7 mm in the basin, although maximum value goes up to 7 mm per day.

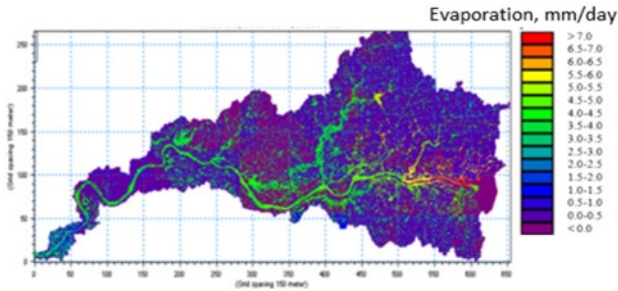


Figure 15. Result of actual evaporation in the basin

5. Canopy Interception Storage

Interception losses from canopy of the vegetation is presented in Figure 16. Mainly forested regions which are in the upstream of the lower Tapi basin show high interception losses. Mean interception loss is 0.11 mm with SD of 0.16 mm.

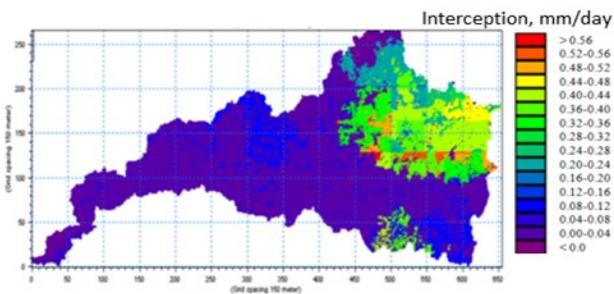


Figure 16. Result of canopy interception storage

6. Depth of Overland Water

Water depth over the ground surface is estimated and aggregated for the season to show accumulated water depth in the basin (Figure 17). Main river and its tributaries streams show high water depth. it may be observed that in the flood plain depressions also water depth is high. Mean accumulated water depth, representing the monsoon season, in the basin found to be 0.064 m with SD of 0.39 m.

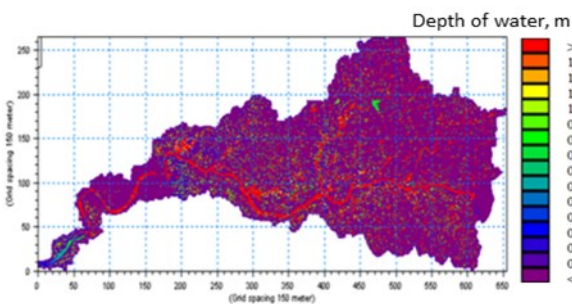


Figure 17. Result of depth of accumulated overland water during the season

7. Infiltration to UZ (negative)

Infiltration to the ground surface is estimated and presented in Figure 18. Mean infiltration is 1.1 mm with standard deviation of 0.45 mm per day.

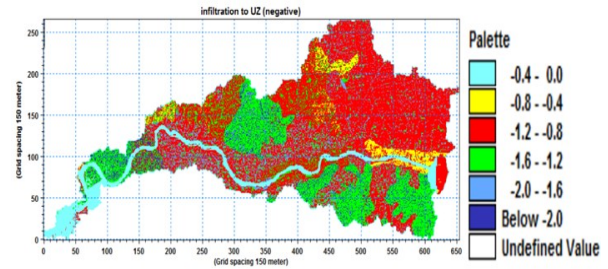


Figure 18. Result of infiltration to unsaturated zone (negative)

Time series plots:

Time series plot for different water balance components such as AET, overland water (runoff), soil moisture etc. for a particular cell for the monsoon season has been extracted and sample results have been shown in the section below., in all-time series plots.

1. Average water content in the root zone

Variation of average water content in a particular cell in time domain is shown in Figure 19. By observing the time series plot, it is found that obtained results for soil moisture gradually increase as the monsoon starts then remains more or less stable during monsoon period and decreases as the monsoon terminates.



Figure 19. Time series of average water content in the root zone

2. Actual Evapotranspiration

AET profile in a particular cell in time domain is shown in Figure 20. Variation of AET is depend on the transpiration losses as well as evaporation from water bodies and these two are govern by variability of rainfall as well as land cover types.

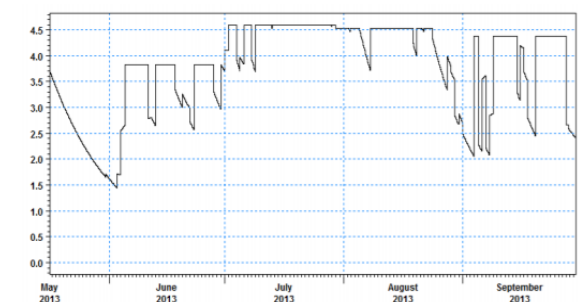


Figure 20. Time series of Actual Evapotranspiration

3. Depth of Overland Water

Water depth on the ground surface fluctuates throughout the monsoon period and mainly govern by the rainfall pattern. Time series of depth of overland water depth in a particular cell is presented in Figure 21.

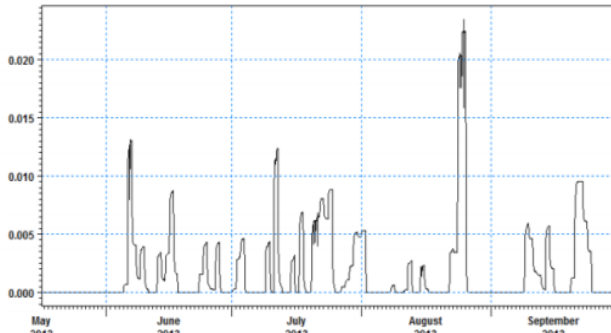


Figure 21. Time series of depth of overland water

MIKE 11 Simulated Results

Hydro-dynamic model MIKE-11 was coupled dynamically with the hydrological model MIKE SHE. Runoff from hydrological model is integrated with the hydro-dynamic model on daily time steps. Therefore, river flow simulations have been performed and water surface elevation along with discharge are estimated. Water Surface Elevation at different cross sections of Lower Tapi river along the longitudinal profile of the river is shown in Figure 22. The spikes in the profiles are indicative of the tributaries junctions.

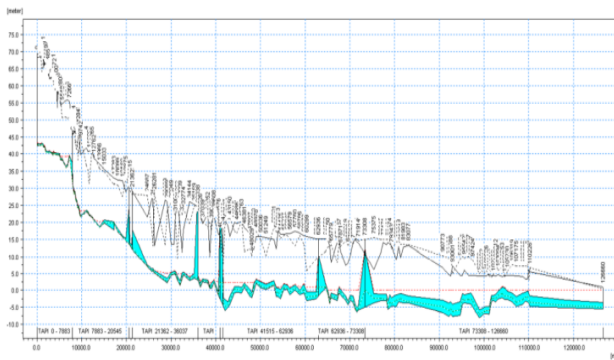


Figure 22. Water surface elevation along the longitudinal profile of the river

Model Calibration

The coupled model was tested using the satellite altimeter (SARAL-Altika) retrieved water levels in absence of in situ measurements with simulated river water levels. Approach for the retrieval of river water level from altimeter is adopted from Gupta et al., 2015. Model calibration was done at Ghala river gauging site (Figure 2). A very good match between the model simulated and altimeter retrieved water levels is obtained. The accuracy in terms of coefficient of determination was obtained with a value of 0.97. Coupled model calibration results is presented in Figure 23.

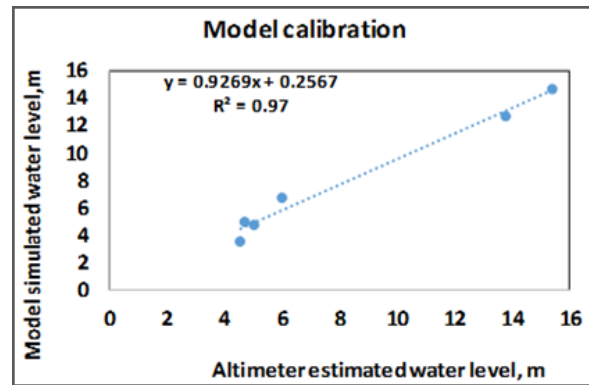


Figure 23. Model calibration results

5. Conclusions

Coupled MIKE SHE and MIKE 11 model has been parameterized integrating the remote sensing derived hydro-meteorological and biophysical variables to simulate the hydrological water balance and river flow over the Lower Tapi river basin. Model was calibrated using the satellite altimeter derived and simulated river water levels. Tested integrated model simulations were carried out to simulate the evapotranspiration, surface runoff, soil moisture, and stream flows. The following conclusions are derived from the present study:

- An integrated modelling system is developed and tested for Lower Tapi basin. The modelling of hydrological water balance is done using MIKESHE and simulation of river flow is done using MIKE11.
- Remote Sensing Provides hydro-meteorological and biophysical variables and plays vital role for the parameterization of data intensive physically base models.
- Major water balance components such as Actual Evapotranspiration and Surface Runoff were obtained 50.2% and 39.7%, respectively for the monsoon season of 2013.
- ET was further partitioned into evaporation and Transpiration and were of 37.2% and 62.8%, respectively.
- Model calibration using altimeter based river water levels was satisfactory with coefficient of determination (R^2)0.97.
- Calibrated integrated model would be useful for long-term hydrological simulations for planning and management of water resources in the region.

Acknowledgements

We thank Human Resource Department, Space Applications Centre (SAC), ISRO Ahmedabad to provide an opportunity for conducting research work at SAC. Thanks to Dr. R.P. Singh, Head of Land Hydrology Division, for his guidance and support.

References

DHI, MIKE SHE User Manual, Volume 1 (2007a) Reference Guide. Danish Hydraulic Institute – Water and Environment: Hørsholm, Denmark.

DHI, MIKE SHE User Manual. Volume 2 (2007b) Reference Guide. Danish Hydraulic Institute – Water and Environment: Hørsholm, Denmark.

DHI, MIKE ZERO Auto Calibration and Parameter Optimisation Tool (2007c) User Guide Danish Hydraulic Institute–Water and Environment: Hørsholm, Denmark.

Clilverd H. M., J. R. Thompson, C. M. Heppell, C. D. Sayer and J. C. Axmacher (2016). Coupled Hydrological/Hydraulic Modelling of River Restoration Impacts and Flood plain Hydrodynamics. *River Research and Applications*. <https://doi.org/10.1002/rra.3036>

Gupta P. K., A. K. Dubey, N. Goswami, R. P. Singh and P. Chauhan (2015). Use of SARAL-Altika Observations for Modeling River Flow. *Marine Geodesy*, 48, 614-625.

Mirela-Alina S. and V. Ana (2015). Applicability of MIKE SHE to Simulate Hydrology in Argesel River

Catchment. *Agriculture and Agricultural Science Procedia* 6, 517-524.

Saidislomkhon U., Y. Mitani and T. Kusuda (2016). An Integrated Hydrological Model for Water Balance Estimation in the Chirchik River Basin, Northern Uzbekistan, *Computational water, Energy, and Environmental Engineering*, 5, 87-97. <http://dx.doi.org/10.4236/cweee.2016.53009>

Zhiqiang Z., W. Shengping, G. Sun, G. M. Steven, H. Zhang, J. Li, M. Zhang, E. Klaghofer and P. Strauss (2008). Evaluation of the MIKE SHE Model for Application in the Loess Plateau, China, *Journal of American water resources association*, 44 (5), 1108-1120. Available: <https://doi.org/10.1111/j.1752-1688.2008.00244.x>.

Subramanya K. (1997). *Flow in open channel hydraulics* (Second edition), Tata McGraw-Hill Publishing, New Delhi.

Geomatics Revealed

IGiS

Integrated GIS & IP Software

VERSION 2.0



MAKE IN INDIA



National Awards on Technology
By The Former President of India,
Dr. A. P. J. Abdul Kalam



Launch of IGiS Version 2.0
By Padam Shri AS Kiran Kumar, Chairman, ISRO and
Shri Tapan Mishra, DIRECTOR, SAC, ISRO.

What's new in IGiS

IGiS Version 2.0 is full of enhancements which you'll appreciate every day. New advanced GIS/IP and SAR modules are vital now a days. New COM Based Architecture makes you even more productive. The more you do with IGiS Version 2.0, the more you'll wonder how you ever did without it.

Enhancements in IGiS Version 2.0

- Advanced GIS / Image Processing
- Microwave SAR Analysis
- Meteorological Analysis
- COM Based Scalable Architecture
- New Ribbon Bar GUI
- Python Customization
- OGC Standards



Product Development Partner



Government of India | Department of Space
Indian Space Research Organisation - (ISRO)



Scanpoint Geomatics Ltd.

www.scanpointgeomatics.com

Scanpoint Geomatics Ltd.

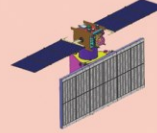
Corporate Office : 12, Abhishree Corporate Park, Iskcon - Ambli Road, Ahmedabad - 380 058. Gujrat (India)
[P] +91 2717 297096-98 [F] +91 2717 297039 [E] info@scanpointgeomatics.com [W] www.scanpointgeomatics.com

INDIAN SPACE RESEARCH ORGANISATION
GOVERNMENT OF INDIA

A Smart Destination For Geospatial Solutions

National Remote Sensing Centre
Hyderabad, India
www.nrsc.gov.in
www.bhuvan.nrsc.gov.in
data@nrsc.gov.in

nrsc



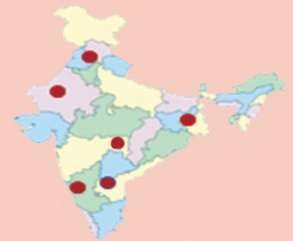
Only Organization in the Country
to Acquire & Supply
Satellite Data to Users



Aerial Acquisition for Specific
User Demands &
Disaster Management Support



Open Data & Value Added
Products Dissemination
Through Bhuvan



Region Specific Solutions



Capacity Building in
Remote Sensing Applications